ENGINEERED MICROARRAYED SURFACES FOR THE DETECTION OF

BIOMOLECULES

By

Zhou Xu

Dissertation

Submitted to the Faculty of the

Graduate School of Vanderbilt University

in partial fulfillment of the requirements

for the degree of

DOCTOR OF PHILOSOPHY

in

Chemical Engineering

May, 2011

Nashville, Tennessee

Approved:

Professor Paul E. Laibinis

Professor Kenneth A. Debelak

Professor Scott A. Guelcher

Professor G. Kane Jennings

Professor Sharon M. Weiss

To my parents

ACKNOWLEDGEMENTS

TABLE OF CONTENTS

LIST OF TABLES

LIST OF FIGURES

CHAPTER I

DNA MICROARRAYS

1.1 Introduction

DNA microarray technology has become an increasingly important tool in
genomic investigations. These systems have been used for gene expression profiling [1,2],
and for identifying single nucleotide polymorphisms [3] in a genetic sample, as well as
characterizing entire genomes. They have provided large databases of information for
the growing area of comparative genomics [4] and as a tool for pharmacogenomic studies,
where a goal is personalization of medicine whereby particular treatments are selected
based on one's genetic profile. These systems have more recently expanded in use
beyond studies in molecular biology, and are finding use in clinical diagnostics (such as
for infectious and genetic disease diagnostics, and cancer diagnostics), and in areas of
biodefense, forensics, and agriculture. Since their first description by Fodor *et al*. in a
1991 paper [5], the DNA microarray area has grown to represent a $500 million/yr
industry, showing growth of roughly 11% a year [6].

DNA microarrays (sometimes referred to as "DNA chips") have enabled
researchers to monitor genome-wide expression profiles. These devices are becoming a
powerful tool for scientists to understand biological mechanisms of complex diseases and
processes at the whole-genomic level. Using the resulting gene expression profiles,
researchers are able to identify novel biomarkers for diseases such as cancers, establish

their correlations to disease phenotypes, and thus classify diseases more accurately. Further, the results can expand clinical abilities in prognosis and diagnosis, and determine likelihoods of treatment success.

The use of microarrays in determining single nucleotide polymorphisms (SNPs) is providing an ability to conduct large-scale genetic linkage analyses that are able to map disease loci and determine the disease susceptibility of various genes. Typical assays contain up to about one million SNPs and offer genotyping abilities at a greater throughput (genome-wide). DNA microarrays make a whole-genome analysis possible for the researcher in a benchtop experiment, reducing required experimental times for such analyses from weeks or months to days.

The ability of DNA microarrays to investigate the interactions between a DNA sample of interest and thousands to hundreds of thousands of different DNA sequences or more in a single experiment has revolutionized procedures for acquiring genomic information. Continued increases in knowledge about the genetic underpinning of many biological functions will likely expand the uses of microarrays for other applications as well as increase requirements on their performance.

1.2 DNA molecules and DNA microarrays

This section is concerned with background information on DNA microarrays, including specifics about the chemical structures of DNA molecules, and the Watson-Crick Model for their hybridization.

1.2.1 DNA molecules

DNA is the acronym of deoxyribonucleic acid. Deoxyribonucleotides are composed of a nitrogenous base that is linked to a five-carbon sugar (a pentose) to which at least one phosphate group is attached [7]. The nitrogenous base molecules are planar, aromatic and heterocyclic, and most common bases fall into two categories: derivatives of purine such as Adenine (A) and Guanine (G); derivatives of pyrimidine such as Cytosine (C), and Thymine (T). The chemical structures of deoxyribonucleotide, purine and pyrimidine, and bases A, G, C, and T are shown in Figure 1.1. The atoms on the ribose are specified by primed numbers while the atoms on the bases use unprimed ones, as purine and pyrimidine. In nucleotides, the phosphate group is either at carbon 3' or carbon 5' position (Figure 1.1 is showing a 5' monophosphate attached to the pentose). Figure 1.2 shows the chemical structures of the four bases linking to the ribose group. Nucleotide units can connect with each other to form a polymeric chain, a single strand DNA, by bridging phosphates between 3' and 5' carbons.

A helical DNA duplex forms when two complementary single strands of DNA bind with each other, based on the DNA model [8] proposed by Watson and Crick in 1953, as shown in Figure 1.3(A). In their suggested model, DNA has two helical chains each coiled around the same axis, and the chains are held together by hydrogen bonding between the purine and pyrimidine bases. The planes of the bases are perpendicular to the axis, and the bases are joined together in pairs with a single base from one chain being hydrogen-bonded to a single base from the other chain. Only specific base pairs can bond with each other, i.e., adenine with thymine (A with T), and guanine with cytosine (G with C). The chemical structure of base paring between two single-stranded

3

Figure 1.1. Chemical structures of deoxyribonucleotide, purine, pyrimidine, and bases.
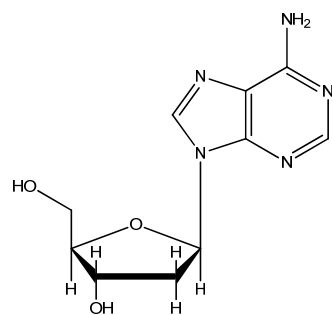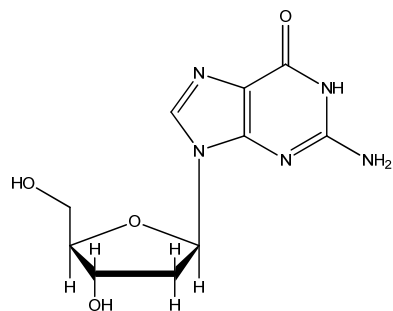
Figure 1.2. Chemical structures of deoxyadenosine, deoxyguanosine, deoxycytidine, and deoxythymidine.
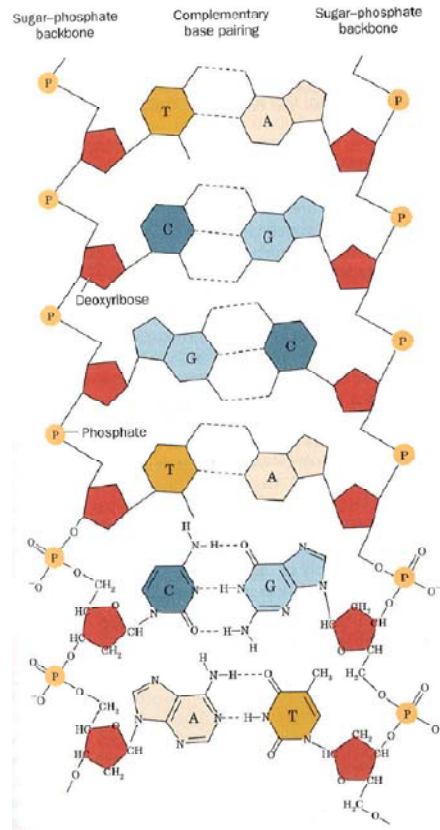
(A)   (B)

Figure 1.3. (A) Schematic illustration of a Watson-Crick DNA double helical model, taken from the original paper [8]. The two ribbons represent sugar-phosphate backbones, and the horizontal rods stand for base pairs. (B) Diagram showing chemical structure of complementary base pairing between two single stranded DNA chains, taken from a textbook[7]. The A and T base pairs have two hydrogen bonds while the G and C base pairs have three.

DNA chains is shown in Figure 1.3(B). The specificity of the base pairing rule suggests a copying mechanism for DNA molecules, and becomes the foundation of modern biological science.

1.2.2 DNA microarrays

DNA microarrays consist of a flat solid surface onto which have been immobilized as many as tens of thousands of single-stranded DNA molecules (that are referred to as "probe DNAs"), each into their own region or spot on the surface. When used for examining DNA sequences, this surface is incubated with a solution containing fluorescently labeled DNA molecules (that are referred to as "target DNAs"). DNA microarrays operate in a massively parallel format and rely on the simple rules of Watson-Crick base-pairings that adenine (A) interacts preferentially with thymine (T) and guanine (G) preferentially with cytosine (C) for their operation. These target DNAs adsorb onto the surface probe DNAs at levels depending on their abilities to hybridize to the probe DNAs. Complementarity between the sequences of the probe and target DNAs is a primary determinant in their levels of adsorption, as illustrated in Figure 1.4. After the incubation step, unbound materials are washed away from the slide, and the array is scanned to provide a fluorescence image of the surface. The intensities from each region of the surface are used to determine those probe DNAs that interacted most strongly with the target DNAs. Such microarray experiments provide details about the sequence of the
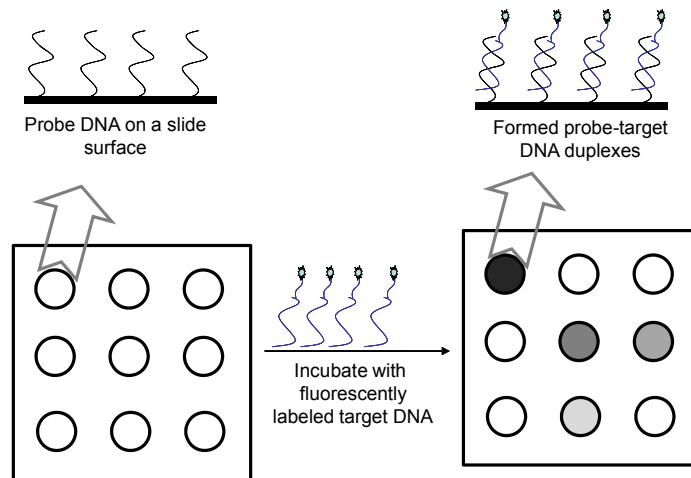
Figure 1.4. Schematic illustration of fluorescently-tagged target DNA molecules hybridizing with probe DNAs on a chip surface. Complementarity between the sequences of the probe and target DNAs is a primary determinant in their levels of adsorption, as indicated in the figure by the gray level on each spot.

target DNAs, and comparison experiments can yield information about mutation levels and whether certain genes have been up- or down-regulated in a process.

1.3 DNA microarray platforms

This section compares the two most commonly used "DNA chip" platforms in current genomic studies, cDNA and oligonucleotide microarrays, and analyzes their advantages and disadvantages.

1.3.1 cDNA microarrays

Most cDNA microarrays are prepared by sequentially spotting solutions containing PCR products or clones from a cDNA library onto poly-lysine coated slides[1,9]. The probe DNAs adsorb onto the poly-lysine surface as a result of electrostatic attractions between the negatively charged DNA chains and the positively charged surface. The sequence lengths for the DNA strands are typically hundreds of base units. Computer-controlled microspotting systems are frequently used to generate the 2-D pattern of different probe DNAs on the slide surface. Figure 1.5 shows the general layout of such microarray spotting systems [9].

cDNA microarrays can be easily customized and fabricated in-house. The spotting of user purified and pre-synthesized probes results in a high probe sequence

9

A

B
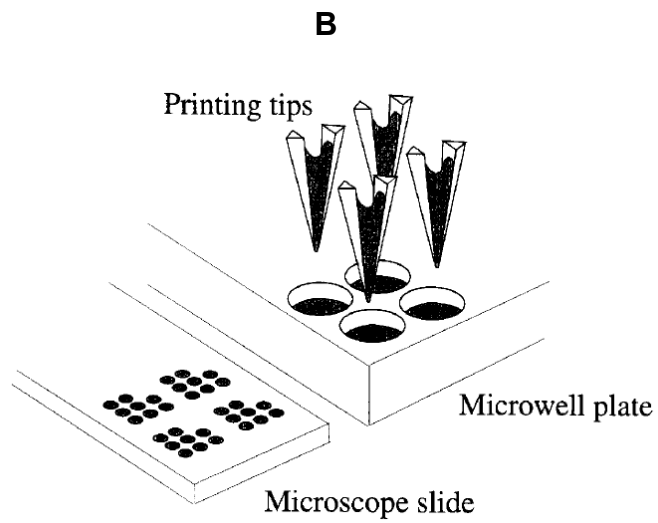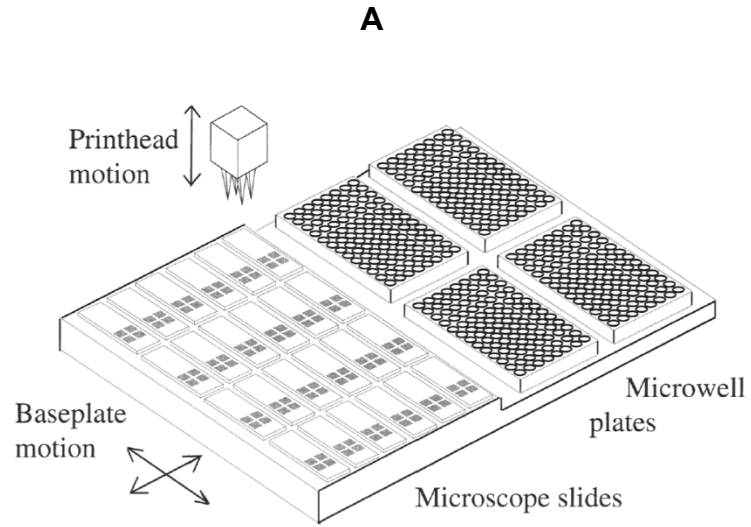
Figure 1.5. (A) The layout of a microarray spotter. (B) A magnified view of the microquill printing tips. Both pictures were taken from a reference paper [9]. The pins on the printhead transfer liquids in the wells of the microwell plates onto microscope slides.

fidelity. However, the fabrication of cDNA microarrays generates multiple-position

attachment of the DNA probes to the slide surface. The resulting structures exhibit

reduced hybridization efficiencies and higher possibilities of forming mismatches than

for the sequences in solution. Additional problems with this technique include high

background signals from sites where no DNA is spotted [10], and high signal variance

between duplicate spots on different slides as well as on the same slide [11]. The

underlying spot-to-spot and slide-to-slide variance in probe DNA surface density and its

distribution can cause inconsistent levels of target-probe hybridization and inaccurate

data [12].

1.3.2 Oligonucleotide microarrays

A competing strategy to the use of spotting pre-formed DNA strands is the

chemical synthesis of oligonucleotides onto the slide surface, where local control over the

reaction chemistry for their formation results in regions with different custom

oligonucleotide sequences. These oligonucleotide microarrays are often prepared by

combinatorial chemical synthesis using either light [13,14] or thermal inkjet printing [15] to

spatially pattern a surface. Typical probe lengths generated by these methods are 25-

mers and 60-mers, respectively. In the light-directed synthesis method, a process

analogous to photolithography is used to control the sequence composition of probe

DNAs as they are synthesized on the surface, as shown in Figure 1.6 [13]. In the inkjet
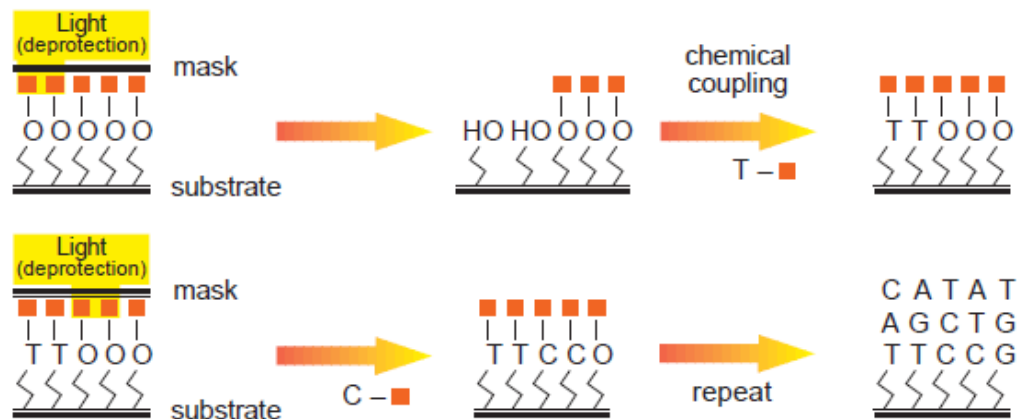
Figure 1.6. The process of the light-directed oligonucleotide synthesis. The picture was taken from a reference paper [13]. A mask is used to define the spatial pattern during the synthesis. Light deprotects and activates the selected sites and the sites are coupled with the protected DNA bases. By repeating the process, high-density oligonucleotide arrays can be fabricated with user-defined probe sequences at each probe site.

printing method, an inkjet printer head delivers the specific bases to each location on the slide in order to generate specified sequences.

These methods have the advantages over microspotting methods (as used for cDNA arrays) in generating smaller feature sizes (typically 10-100 μm) and higher density arrays and provide end-immobilization. However, they require the use of custom equipment and highly controlled environments, and the specialized nature of their preparation places limits on the abilities to customize them for a particular investigation. Furthermore, the probes fabricated by stepwise synthesis consist of full-length sequences as well as truncated sequences. For example, the yield of average stepwise oligonucleotide synthesis in the photolithographic process is in the range of 92~94% [16], therefore, the probe sequence fidelity, i.e., the percentage of the full-length sequence at a 25-mer probe surface is ~ $(0.94)^{25} = 21\%$. The nearly 79% truncated sequences complicates the binding events between probes and targets, probably due to the probe-probe interactions, steric effects and electrostatic effects, which makes the hybridization data analysis more challenging [17]. In comparison, the typical step yield in an inkjet printing method has been estimated as 99.5% [18], thus the probe sequence fidelity for a typical 60-mer surface is $(0.995)^{60} = 74\%$, and nearly 26% are truncated sequences.

1.3.3 Motivation for a DNA microarray platform

cDNA microarrays and oligonucleotide microarrays have their own strengths and limitations, as described in sections 1.3.1 and 1.3.2. My first goal of this work is to

combine the strengths from both methods and provide a DNA microarray architecture which contains end-immobilized DNA strands to the chip surface (a feature of oligonucleotide arrays) and has high fidelity of probe sequences on the chip surface (a feature of cDNA arrays).

My microarray preparation combines the approaches of solid-phase oligonucleotide synthesis and conventional microarray spotting, as a general way to prepare end-immobilized oligonucleotide structures at surfaces. Solid-phase oligonucleotide synthesis chemistry can be used to generate covalently attached DNA strands at a surface by an automated process involving single base additions. The resulting single-stranded DNA surface is used for immobilizing secondary DNA strands that can be selected to be gene specific. An available microspotting system provides an ability to locate probe DNA solutions onto the surface of the substrate efficiently and precisely for the generation of microarrays. An overview of this process is shown in Figure 1.7. This method provides selectability over the spots comprising the microarray and their locations.

1.4 *In situ* DNA hybridization and dehybridization

Despite the increasing use of microarrays for genomic investigations, there have been few studies that have examined the processes of DNA hybridization and dehybridization *in situ* on such surfaces. Presently, *in situ* investigations have largely been limited to experiments conducted on single spots and employed techniques such as
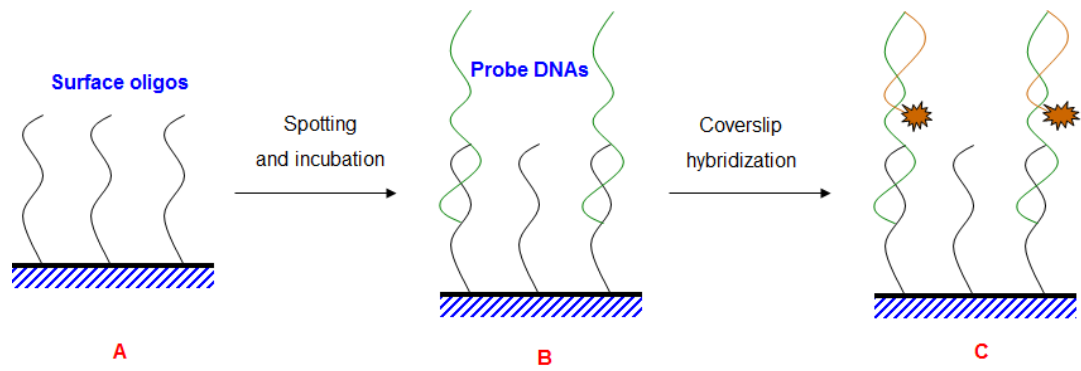
Figure 1.7. The process overview of my DNA microarray platform. (A) Short ss-DNA strands are chemically synthesized on a glass slide surface to provide anchor sites for attachmen. (B) DNA probes of interest containing an end region complementary to the surface strands are printed as a pattern on the chip surface, and then incubated to facilitate their immobilization. (C) When used to obtain genomic information, the surface DNA probes are presented for hybridization to fluorescently-tagged DNA sequences.

surface plasmon resonance that work well for gold surfaces but not those commonly used

as supports for microarrays. This section begins by reviewing studies on *in situ* detection

of surface association and/or dissociation reactions by using one of two commonly used

techniques, either surface plasmon resonance spectroscopy (section 1.4.1) or total internal

reflection fluorescence (1.4.2), and then it discusses the motivation of using the latter

technique to acquire kinetics data for DNA adsorption and desorption in an array format

(section 1.4.3).

1.4.1 Surface Plasmon Resonance Spectroscopy (SPR)

Surface plasmons are electromagnetic surface waves that can propagate along

the interface between a metal (gold is commonly used) and a dielectric[19,20]. When a

polarized incident light illuminates a gold film, total internal reflection will be achieved

when the incident angle is greater than the critical angle. An evanescent wave will be

generated and can penetrate the metal thin film. At a particular angle of illumination, the

evanescent wave can be coupled into surface plasmon modes, and a portion of the energy

of the light wave is transferred to the metal's electrons, causing an observable decrease in

reflectivity[20,21]. The generated evanescent wave will decay exponentially beyond the

gold film by a short distance between 100 to 600 nm[21]. As a result, the particular angle at

which the surface plasmons occur is sensitive to changes in the refractive index of any

medium very close to the surface of the gold film[20,22]. This ability provides SPR with the

potential for detecting species that occupy within the range of the evanescent wave

without any requirements of labeling. The main applications of SPR include *in situ* detection of antibody-antigen interactions, protein adsorption, and DNA-DNA hybridization and denaturization at surfaces.

Using two-color SPR spectroscopy, Georgiadis *et al*. quantified the amount of thiol-tethered DNA on a gold surface and monitored the kinetics of hybridization and the process of thermally-induced dehybridization to these DNA strands [22]. They developed an adsorption/desorption/diffusion model to fit the kinetics data of 25-mer DNA hybridization [23]. They showed that the hybridization kinetics for their DNA oligomers were sensitive to the presence of base pair mismatches, the location at which the hybridization occurs [24], and the probe density [25]. Different from SPR spectroscopy, SPR imaging uses a collimated beam to illuminate the entire surface, and the reflected light is collected by a CCD camera. Researchers have applied SPR imaging for *in situ* DNA hybridization detection and hybridization kinetics studies [20,26-28].

Although SPR techniques have been used extensively in the studies of DNA hybridization kinetics, SPR has its shortcomings. The surface preparation, i.e. attaching probes onto a gold surface, remains as the main barrier for SPR to play a bigger role in DNA microarrays, as current microarrays are done on glass slide surfaces for reasons of cost and availability. Nonspecific interactions with the surface are another problem as any change in the refractive index in the near-surface region within the evanescent field will affect the SPR signal. The change of the refractive index depends on the concentration and temperature of the bulk solution, sometimes making it difficult to distinguish the SPR signals from the surface binding events and those from the response to bulk effects [29]. In addition, the attachment of DNA molecules to gold for use in SPR

experiments is usually formed using gold-thiol interactions. These interactions do not produce covalent bonds, and the films on gold can detach from the surface at temperature below those of melting for DNA duplexes. As my experiments require routine exposure of surfaces to elevated temperatures as for examinations of melting transitions, I conclude that SPR is not suitable for this work. However, the SPR studies have provided a good database for comparison.

1.4.2 Total Internal Reflection Fluorescence (TIRF)

Total internal reflection fluorescence (TIRF) is a technique that detects local amounts of fluorescently tagged species near a surface. This technique is sometimes also referred to as evanescent wave-induced fluorescence (EWIF) [30]. As shown in Figure 1.8, when light is incident on an interface between glass and a medium having a lower refractive index than glass at an incident angle greater than the critical angle, light is totally reflected at that interface [31]. This condition under total internal reflection generates an evanescent field in the medium. The intensity of this evanescent wave decays exponentially from the interface and is negligible in less than a wavelength, as shown in the following equation [32]:

$$I(z) = I(0)e^{-z/d} , \tag{1.1}$$

where $d = \left(\dfrac{2\pi}{\lambda_0} \sqrt{n_1^2 \sin^2 \theta_i - n_2^2} \right)^{-1}$, z is the perpendicular distance from the interface to the solution. λ_0 is the wavelength of the incident light in vacuum, n_1 and n_2 are the refractive indices for the high-index and low-index media, respectively, and θ_i is the incident angle.

18
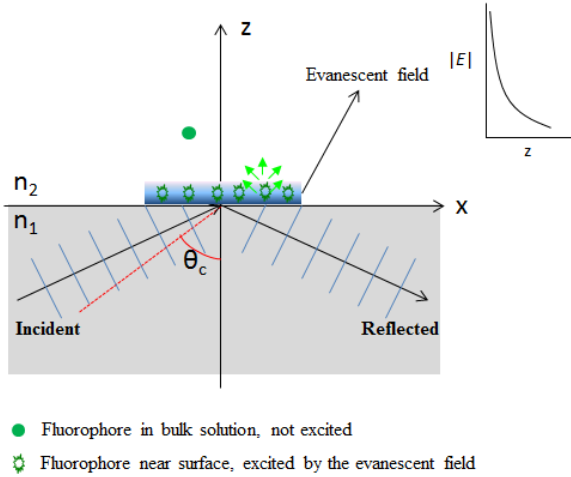
Figure 1.8. The schematic illustration of total internal reflection. In the figure, n_1 and n_2 are the refractive indices of two media, such as glass and water solution, respectively ($n_1 > n_2$). The incident light is totally reflected at the interface at an incident angle greater than the critical angle θ_c. The generated evanescent field decays exponentially from the interface toward the solution. The fluorophores near the surface (for $z \leq 100$ nm) are excited by the evanescent field, while those in the bulk solution are not. More information on TIRF can be found in a review paper [32].

The depth d decreases with increasing incident angles θ_i, and is in the order of or less

than the wavelength λ_0 (unless at $\theta_i = \theta_c$, d is infinite).

As a result, the evanescent wave can be used to excite fluorophores

immediately adjacent to the interface while those in the bulk solution are outside the

evanescent field and thus not affected. Thereby the TIRF technique can be similarly used

for *in situ* measurements as with SPR; however, a primary difference is that fluorescently

labeled species are required for TIRF. The resulting fluorescence in TIRF can be

detected continuously by a CCD camera, thereby allowing the technique to monitor real

time changes that occur at a glass surface. These attributes make TIRF attractive for a

variety of studies involving surface adsorption and desorption. For example, TIRF has

been used to study cell and substrate interactions [33-35], protein adsorption [36-38], specific

ligand-receptor interactions [39,40], antibody-antigen interactions [41], and receptor cluster

formation [42]. Although there are broad studies on applying TIRF to problems in cell

biology [43,44], there are few reports that have used TIRF to study nucleic acid interactions

at surfaces [45,46]. For a recent review on TIRF and its applications, see the reference [32].

1.4.3 Motivation for in situ measurements of DNA interactions

Currently, DNA microarrays are typically scanned to obtain static fluorescent

images of slides after they have undergone hybridization and washing steps. The

measured fluorescent intensity indicates the equilibrium level of the hybridization

reaction between probe and target DNA molecules under specific experimental

conditions. However, the microarray scanning experiment does not provide kinetics data before the system reaches equilibrium, and thus is lack of quantitative information to describe the DNA-DNA molecular interactions in real time.

Here, a focus is on the use of an *in situ* technique that is compatible with the substrate used for DNA chips (glass) and that allows multiple spots to be investigated simultaneously. TIRF is such a technique as it is able to detect fluorescent signal at glass/water interface. To obtain quantitative kinetics data of DNA interactions, in this work, I aim at (1) measuring DNA hybridization kinetics under room temperature, and (2) obtaining DNA thermal melting curves under a temperature sweep. I first assemble a TIRF system to observe the hybridization process at a DNA chip surface, and use the kinetics data to determine parameters such as association and dissociation constants, and affinity constants. Secondly, to further study behaviors of DNA interactions at surface, a temperature control system is integrated with the TIRF setup and DNA melting behaviors at surface are able to be monitored in real time. The DNA melting experiments provide useful additional information on DNA thermal stability at surface.

From these studies, the expectation is that more detailed kinetic and thermodynamic information will be obtained regarding DNA interactions [47,48]. Further, such information will provide a greater understanding of how DNA behaves at surfaces and allow more quantitative information to be obtained for genetic analysis.

1.5 Summary

This work is directed toward establishing methods and surface architectures that allows the monitoring of DNA hybridization and dehybridization at microarrayed surfaces in real time. Coupled with this goal is the development of an approach that allows the employed DNA microarrays to be prepared using readily available instrumentation so to allow their in-house construction and flexible customization (Chapter II). DNA hybridization and thermal desorption kinetics were monitored *in situ* on homogeneous surfaces by total internal reflection fluorescence (Chapter III and IV). DNA thermal desorption behaviors were further investigated on patterned surfaces (Chapter V). The data from the hybridization and dehybridization processes were obtained in real-time, providing information that is presently not available using current commercial microarrays.

References

1   Schena, M.; Shalon, D.; Davis, R. W.; Brown, P. O., "Quantitative Monitoring of Gene Expression Patterns with a Complementary DNA Microarray", *Science* **1995**, *270*, 467-470.

2   DeRisi, J. L.; Iyer, V. R.; Brown, P. O., "Exploring the Metabolic and Genetic Control of Gene Expression on a Genomic Scale", *Science* **1997**, *278*, 680-686.

3   Oh, S. J.; Ju, J.; Kim, B. C.; Ko, E.; Hong, B. J.; Park, J.-G.; Park, J. W.; Choi, K. Y., "DNA Microarrays on a Dendron-modified Surface Improve Significantly the Detection of Single Nucleotide Variations in the p53 Gene", *Nucleic Acids Research* **2005**, *33*, e90.

4   Cannon, C. H.; Kua, C. S.; Lobenhofer, E. K.; Hurban, P., "Capturing Genomic Signatures of DNA Sequence Variation Using a Standard Anonymous Microarray Platform", *Nucleic Acids Research* **2006**, *34*, e121.

5   Fodor, S.; Read, J.; Pirrung, M.; Stryer, L.; Lu, A.; Solas, D., "Light-directed, Spatially Addressable Parallel Chemical Synthesis", *Science* **1991**, *251*, 767-773.

6   *http://www.marketresearch.com (search for "DNA microarrays: A market update")*.

7   Voet, D.; Voet, J. G.; Pratt, C. W. *Fundamentals of Biochemistry, Upgrade Edition*; John Wiley & Sons, Inc.: New York, NY, 2002, 42.

8   Watson, J. D.; Crick, F. H. C., "Molecular Structure of Nucleic Acids: A Structure for Deoxyribose Nucleic Acid", *Nature* **1953**, *171*, 737 - 738.

9   Shalon, D.; Smith, S. J.; Brown, P. O., "A DNA Microarray System for Analyzing Complex DNA Samples Using Two-color Fluorescent Probe Hybridization", *Genome Res* **1996**, *6*, 639-645.

10   Eisen, M. B.; Brown, P. O., "DNA Arrays for Analysis of Gene Expression ", *Methods in Enzymology* **1999**, *303*, 179-205.

11   Kozarova, A.; Petrinac, S.; Ali, A.; Hudson, J. W., "Array of Informatics: Applications in Modern Research", *J. Proteome Res.* **2006**, *5*, 1051-1059.

12   Lee, C.-Y.; Harbers, G. M.; Grainger, D. W.; Gamble, L. J.; Castner, D. G., "Fluorescence, XPS, and TOF-SIMS Surface Chemical State Image Analysis of DNA Microarrays", *J. Am. Chem. Soc.* **2007**, *129*, 9429-9438.

13   Lipshutz, R. J.; Fodor, S. P. A.; Gingeras, T. R.; Lockhart, D. J., "High Density Synthetic Oligonucleotide Arrays", *Nature Genetics* **1999**, *21*, 20-24.

14   Pease, A. C.; Solas, D.; Sullivan, E. J.; Cronin, M. T.; Holmes, C. P.; Fodor, S. P., "Light-generated Oligonucleotide Arrays for Rapid DNA Sequence Analysis ", *Proc. Natl. Acad. Sci. USA* **1994**, *91*, 5022-5026.

15   Bruhn, L.; Caren, M. P.; Schembri, C. T.; Schleifer, A., "Method and Apparatus for Making Nucleic Acid Arrays", US 6458583 (**2002**).

16   McGall, G. H.; Barone, A. D.; Diggelmann, M.; Fodor, S. P. A.; Gentalen, E.; Ngo, N., "The Efficiency of Light-Directed Synthesis of DNA Arrays on Glass Substrates", *J. Am. Chem. Soc.* **1997**, *119*, 5081-5090.

17   Glazer, M.; Fidanza, J. A.; McGall, G. H.; Trulson, M. O.; Forman, J. E.; Suseno, A.; Frank, C. W., "Kinetics of Oligonucleotide Hybridization to Photolithographically Patterned DNA Arrays", *Analytical Biochemistry* **2006**, *358*, 225-238.

18   https://www.chem.agilent.com/Library/applications/5989-9159Scanner%20app%20note%20(2).pdf

19   Raether, H. *Surface Plasmons on Smooth and Rough Surfaces and on Gratings*; Springer-Verlag: New York, 1988,

20   Thiel, A. J.; Frutos, A. G.; Jordan, C. E.; Corn, R. M.; Smith, L. M., "In Situ Surface Plasmon Resonance Imaging Detection of DNA Hybridization to Oligonucleotide Arrays on Gold Surfaces", *Anal. Chem.* **1997**, *69*, 4948-4956.

21   Homola, J., "Surface Plasmon Resonance Sensors for Detection of Chemical and Biological Species", *Chem. Rev.* **2008**, *108*, 462-493.

22   Peterlinz, K. A.; Georgiadis, R. M.; Herne, T. M.; Tarlov, M. J., "Observation of Hybridization and Dehybridization of Thiol-Tethered DNA Using Two-Color Surface Plasmon Resonance Spectroscopy", *J. Am. Chem. Soc.* **1997**, *119*, 3401-3402.

23   Georgiadis, R.; Peterlinz, K. P.; Peterson, A. W., "Quantitative Measurements and Modeling of Kinetics in Nucleic Acid Monolayer Films Using SPR Spectroscopy", *J. Am. Chem. Soc.* **2000**, *122*, 3166-3173.

24   Peterson, A. W.; Heaton, R. J.; Georgiadis, R., "Kinetic Control of Hybridization in Surface Immobilized DNA Monolayer Films", *J. Am. Chem. Soc.* **2000**, *122*, 7837-7838.

25   Peterson, A. W.; Wolf, L. K.; Georgiadis, R. M., "Hybridization of Mismatched or Partially Matched DNA at Surfaces", *J. Am. Chem. Soc.* **2002**, *124*, 14601-14607.

26   Wolf, L. K.; Fullenkamp, D. E.; Georgiadis, R. M., "Quantitative Angle-Resolved SPR Imaging of DNA−DNA and DNA−Drug Kinetics", *J.Am. Chem. Soc.* **2005**, *127*, 17453-17459.

27   Jordan, C. E.; Frutos, A. G.; Thiel, A. J.; Corn, R. M., "Surface Plasmon Resonance Imaging Measurements of DNA Hybridization Adsorption and Streptavidin/DNA Multilayer Formation at Chemically Modified Gold Surfaces", *Anal. Chem.* **1997**, *69*, 4939-4947.

28   Lee, H. J.; Goodrich, T. T.; Corn, R. M., "SPR Imaging Measurements of 1-D and 2-D DNA Microarrays Created from Microfluidic Channels on Gold Thin Films", *Anal. Chem.* **2001**, *73*, 5525-5531.

29   Grassi, J. H.; Georgiadis, R. M., "Temperature-Dependent Refractive Index Determination from Critical Angle Measurements: Implications for Quantitative SPR Sensing", *Anal. Chem.* **1999**, *71*, 4392-4396.

30   Rondelez, F.; Ausserre, D.; Hervet, H., "Experimental Studies of Polymer Concentration Profiles at Solid-Liquid and Liquid-Gas Interfaces by Optical and X-ray Evanescent Wave Techniques", *Ann. Rev. Phys. Chem.* **1987**, *38*, 317-347.

31   Thompson, N. L.; Burghardt, T. P., "Total Internal Reflection Fluorescence : Measurement of Spatial and Orientational Distributions of Fluorophores Near Planar Dielectric Interfaces ", *Biophysical Chemistry* **1986**, *25*, 91-97.

32   Axelrod, D., "Total Internal Reflection Fluorescence Microscopy", *Biophysical Tools for Biologists* **2008**, *Vol 2: In Vivo Techniques*, 169-221.

33   Gingell, D.; Heavens, O. S.; Mellor, J. S., "General Electromagnetic Theory of Total Internal Reflection Fluorescence: the Quantitative Basis for Mapping Cell-Substratum Topography ", *J. of Cell Sci.* **1987**, *87*, 677-693.

34   Todd, I.; Mellor, J. S.; Gingell, D., "Mapping Cell-Glass Contacts of Dictyostelium Amoebae by Total Internal Reflection Aqueous Fluorescence Overcomes a Basic Ambiguity of Interference Reflection Microscopy ", *J. of Cell Sci.* **1988**, *89*, 107-114.

35   Burmeister, J. S.; Olivier, L. A.; Reichert, W. M.; Truskey, G. A., "Application of Total Internal Reflection Fluorescence Microscopy to Study Cell Adhesion to Biomaterials ", *Biomaterials* **1998**, *19*, 307-325.

36   Hlady, V.; Rickel, J.; Andrade, J. D., "Fluorescence of Adsorbed Protein Layers. II. Adsorption of Human Lipoproteins Studied by Total Internal Reflection Intrinsic Fluorescence ", *Colloids and Surfaces* **1988/89**, *34*, 171-183.

37   Robeson, J. L.; Tilton, R. D., "Spontaneous Reconfiguration of Adsorbed Lysozyme Layers Observed by Total Internal Reflection Fluorescence with a pH-Sensitive Fluorophore", *Langmuir* **1996**, *12*, 6104-6113.

38   Xu, Z.; Marchant, R. E., "Adsorption of Plasma Proteins on Polyethylene Oxide-Modified Lipid Bilayers Studied by Total Internal Reflection Fluorescence", *Biomaterials* **2000**, *21*, 1075-1083.

39   Poglitsch, C. L.; Thompson, N. L., "Interaction of Antibodies with Fc Receptors in Substrate-Supported Planar Membranes Measured by Total Internal Reflection Fluorescence Microscopy", *Biochemistry* **1990**, *29*, 248-254.

40   Kalb, E.; Engel, J.; Tamm, L. K., "Binding of Proteins to Specific Target Sites in Membranes Measured by Total Internal Reflection Fluorescence Microscopy", *Biochemistry* **1990**, *29*, 1607-1613.

41   Hlady, V.; Lin, J. N.; Andrade, J. D., "Spatially Resolved Detection of Antibody—Antigen Reaction on Solid/Liquid Interface Using Total Internal Reflection Excited Antigen Fluorescence and Charge-Coupled Device Detection", *Biosensors & Bioelectronics* **1990**, *5*, 291-301.

42   Wang, M. D.; Axelrod, D., "Time-Lapse Total Internal Reflection Fluorescence Video of Acetylcholine Receptor Cluster Formation on Myotubes", *Developmental Dynamics* **1994**, *201*, 29-40.

43   Axelrod, D., "Total Internal Reflection Fluorescence Microscopy in Cell Biology", *Traffic* **2001**, *2*, 764-774.

44   Toomre, D.; Manstein, D. J., "Lighting Up the Cell Surface With Evanescent Wave Microscopy", *Trends in Cell Biology* **2001**, *11*, 298-303.

45   Lehr, H.-P.; Reimann, M.; Brandenburg, A.; Sulz, G.; Klapproth, H., "Real-Time Detection of Nucleic Acid Interactions by Total Internal Reflection Fluorescence", *Anal. Chem.* **2003**, *75*, 2414-2420.

46   Michel, W.; Mai, T.; Naiser, T.; Ott, A., "Optical Study of DNA Surface Hybridization Reveals DNA Surface Density as a Key Parameter for Microarray Hybridization Kinetics", *Biophysical Journal* **2007**, *92*, 999-1004.

47   May, C. J.; Canavan, H. E.; Castner, D. G., "Quantitative X-ray Photoelectron Spectroscopy and Time-of-Flight Secondary Ion Mass Spectrometry Characterization of the Components in DNA", *Anal. Chem.* **2004**, *76*, 1114-1122.

48   Southern, E.; Mir, K.; Shchepinov, M., "Molecular interactions on microarrays", *Nature Genetics Supplement* **1999**, *21*, 5-9.

CHAPTER II

HYBRIDIZATION TO SURFACE END-IMMOBILIZED OLIGONUCLEOTIDES BY SPOTTING

2.1 Introduction

The purpose of this chapter is to provide a method for generating a surface architecture that allows end-immobilization of DNA probes with high sequence fidelity, as being discussed in Chapter I, section 1.3. This approach involves with combining the advantages of surface oligonucleotide synthesis chemistry and conventional microarray spotting, as a way to generate end-immobilized oligonucleotide structures at surfaces. Solid-phase oligonucleotide synthesis chemistry can generate covalently attached DNA strands at surface by a process involving single base additions. Single stranded DNA surfaces are used here as the basis for immobilizing secondary DNA strands that can be selected to be gene specific. Readily available microspotting systems provide an ability to locate probe DNA solutions on the surface of a substrate efficiently and precisely for the generation of microarrays. This chapter demonstrates the feasibility of this approach: single stranded DNA (17-20 mer) was synthesized on a glass slide surface; the synthesized single stranded DNA was able to bind to its complementary probe DNA strand and the bound probe DNA was used for later hybridization; and the binding events could be quantified by the fluorescence signal.

2.2 Materials and methods

2.2.1 Materials

The DNA synthesis reagents were obtained from Glen Research (Sterling, VA). Ultramild CE phosphoramidites that were used for oligonucleotide synthesis included 5'-dimethoxytrityl-N-phenoxyacetyl-2'-deoxyadenosine, 3'-[(2-cyanoethyl)-(N,N-diisopropyl)]-phosphoramidite (Pac-dA-CE Phosphoramidite), 5'-dimethoxytrityl-N-acetyl-2'-deoxycytidine,3'-[(2-cyanoethyl)-(N,N-diisopropyl)]-phosphoramidite (Ac-dC-CE Phosphoramidite), and 5'-dimethoxytrityl-N-p-isopropyl-phenoxyacetyl-deoxyguanosine, 3'-[(2-cyanoethyl)-(N,N-diisopropyl)]-phosphoramidite (iPr-Pac-dG-CE Phosphoramidite). For T bases, standard 5'-dimethoxytrityl-2'-deoxythymidine,3'-[(2-cyanoethyl)-(N,N-diisopropyl)]-phosphoramidites (dT-CE Phosphoramidite) were used as T bases had no protective groups. The chemical structures of the four phosphoramidites are shown in Figure 2.1. DNA sequences noted in Table 2.1 as Tags #1 and #2, and Probes #1 and #2 were supplied by Integrated DNA Technologies, Inc. (Coralville, IA). N-(3-triethoxysilylpropyl)-4-hydroxy-butyramide was obtained from Gelest Inc. (Morrisville, PA). Betaine, 20×SSC, and SDS were purchased from Sigma (St. Louis, MO). Ethylenediamine was supplied by Acros Organics (Morris Plains, NJ).
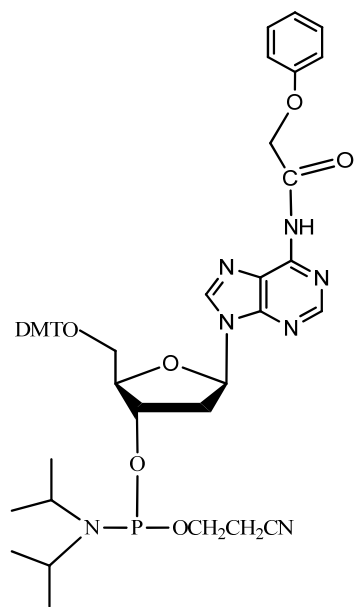
Pac-dA-CE Phosphoramidite
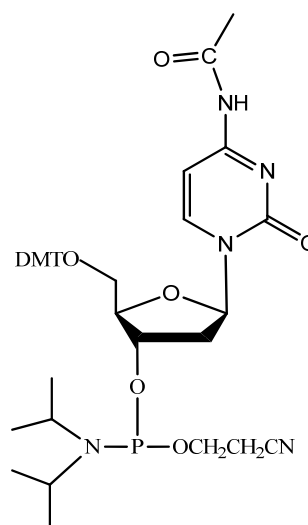
Ac-dC-CE Phosphoramidite
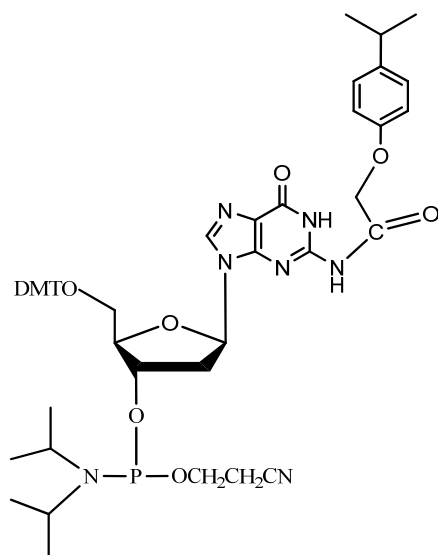
iPr-Pac-dG-CE Phosphoramidite
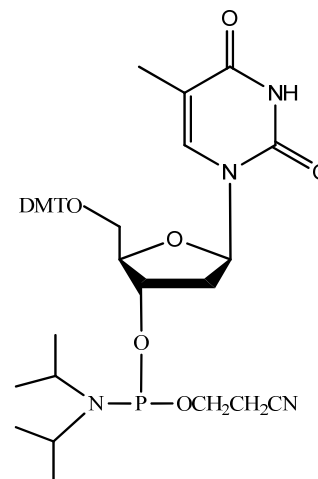
dT-CE Phosphoramidite

Figure 2.1. Chemical structures of Pac-dA-CE, Ac-dC-CE, iPr-Pac-dG-CE, dT-CE phosphoramidites.

2.2.2 Slide preparation

Microscopic slides were cleaned in piranha solution (7:3(v/v), concentrated H_2SO_4 : 30% H_2O_2. Caution: "piranha" solution reacts violently with organic material and should be used with great care.) for 30 min, followed by rinsing with copious quantities of deionized water and drying under a N_2 stream. The slides were then immersed into a 1 wt.% N-(3-triethoxysilylpropyl)-4-hydroxy-butyramide (Gelest, Morrisville, PA) solution in 95% ethanol for 16 hours to produce a hydroxyl silane surface. The slides were removed from the silane solution, rinsed sequentially with ethanol and water, and then blown dry with N_2. Then the slides were heated in an oven at ~110 °C for 30 min to anneal the films.

The samples exhibited advancing contact angles of water (θ_a) of 60-63° and 33-43° before and after the annealing step, respectively. Water contact angles were measured using a Ramé-Hart goniometer 100-01 S under ambient conditions. For the measurements of advancing contact angles, the pipette tip was remained in the water drop. Contact angles were measured on both sides of the drop. At least three measurements were performed at different positions on each sample surface.

2.2.3 DNA synthesis on the slide surface

An Applied Biosystems Model 392 DNA Synthesizer (Life Technologies Corporation, Carlsbad, California) was modified to direct reagent flow across the surface of a hydroxyl-derivatized slide, as shown in Figure 2.2. Reaction conditions such as
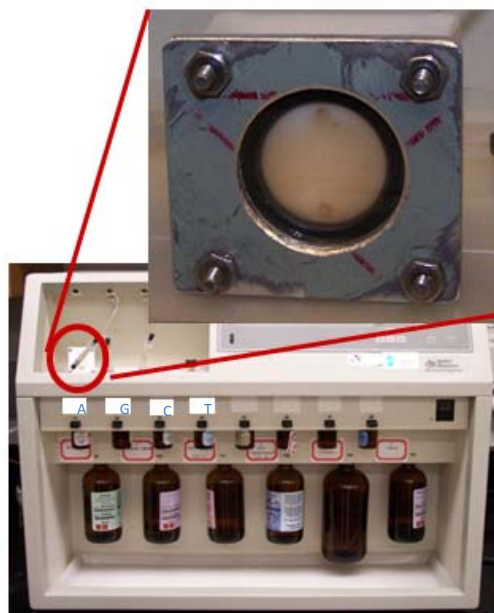
Figure 2.2. The Applied Biosystems Model 392 DNA synthesizer with a custom-modified cell assembly which allows reagents flow across a slide surface.

coupling time were selected to satisfy the reaction at the slide surface. The ammonium

hydroxide cleavage step was omitted to retain the synthesized oligos on the surface [1].

Oligonucleotide strands were synthesized on the reactive hydroxyl surfaces

using standard phosphoamidite chemistry. The synthesis cycle is depicted in Figure 2.3,

and consists of four reaction steps: coupling, capping, oxidation, and detritylation [2].

First, a phosphoramidite in solution is activated by a weak acid, tetrazole, and the

reactive intermediate, tetrazoyl phosphoramidite, is coupled to the surface hydroxyl

group. Next, unreacted hydroxyl groups on the surface are capped by acetylation using

acetic anhydride and 1-methylimidazole. The capping step minimizes the length of the

impurities, and thus the chances for non-specific binding. Then the phosphite is

converted to the phosphotriester using Iodine as the oxidizing agent and water as the

oxygen donor. Finally, the dimethoxytrityl group is removed with trichloroacetic acid to

expose the 5' hydroxyl group as the coupling point for the next phosphoramidite. The

synthesis cycle is repeated until desired chain elongation is completed.

After the synthesis, the slide was removed from the synthesizer, rinsed

sequentially with ethanol and water, and then immersed into an ethylenediamine/ethanol

(50/50, v/v) solution for one hour to remove both the base and phosphate protective

groups [3,4]. Following the deprotection, the sample was rinsed sequentially with ethanol

and water, blown dry with N_2, and used as a substrate in spotting experiments.

The sequences synthesized on a slide surface are given in Table 2.1 with

notations as Surf A and Surf B. The oligonucleotides (17-mer or 20-mer) were produced

in the 3'$\rightarrow$ 5' direction. The first five bases (all T's) were used as spacers. Table 2.1

shows the complementarity between the various probes, tags, and surface sequences.
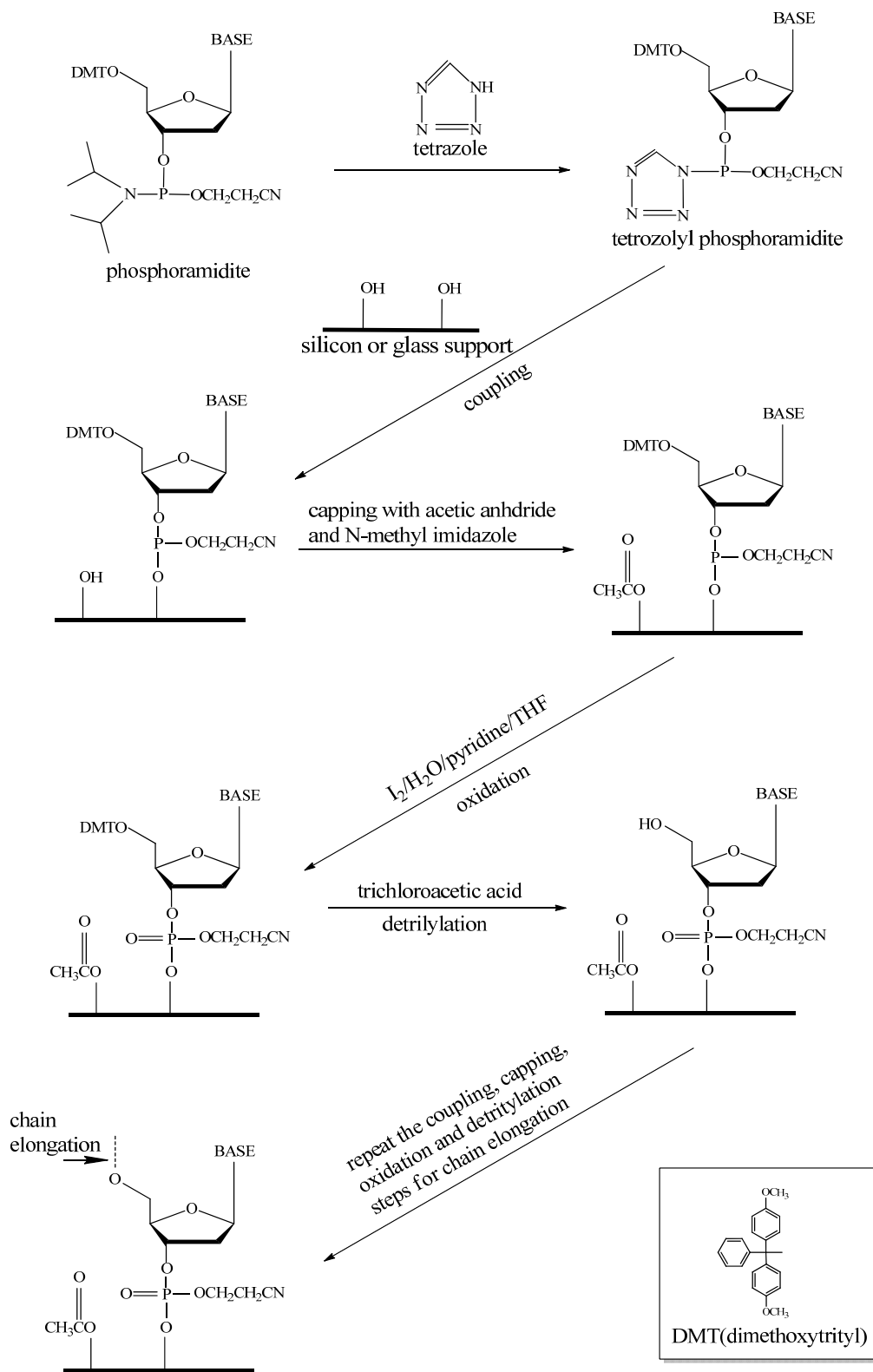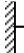
Figure 2.3. The synthesis cycle of surface oligos using standard phosphoamidite chemistry on a slide surface derivatized with OH silane.

Table 2.1 Oligomer nomenclature and sequences

Name	Sequence
Surf A	╟—3'-TTTTT<u>GCCTCCACGATT</u>-5'
Tag #1	5'-<u>CGGAGGTGCTAA</u>GAT Cy3 -3' (complementary to Surf A)
Tag #2	5'-<u>TCCGACCCAGTA</u>TTC Cy3 -3' (noncomplementary to Surf A)
Surf B	╟—3'-TTTTT<u>ACGCTACAAGTACGG</u>-5'
Probe #1	5'-<u>TGCGATGTTCATGCC</u>TTTTT<u>ATCTTAGCACCTCCG</u>-3' (Tag #1 3'- Cy3 <u>TAGAATCGTGGAGGC</u>-5')
Probe #2	5'-<u>TGCGATGTTCATGCC</u>TTTTT<u>GAATACTGGGTCGGA</u>-3' (Tag #2 3'- Cy3 <u>CTTATGACCCAGCCT</u> -5')

Both Tag #1 and Tag #2 were fluorescently modified at the 3' end by dye Cy3, and Tag #1 was complementary to Surf A, and Tag #2 was not. For non-fluorescently tagged Probe #1 and Probe #2, their 5' ends were complementary to Surf B, 3' ends were complementary to Tag #1 and Tag #2, respectively, and there were 5 T's in between as spacers.

With the above 3'-phosphoramidites as mentioned in section 2.2.1, the oligonucleotides were produced in the 3'→ 5' direction. Alternatively, the oligonucleotides can be synthesized in the 5' → 3' direction by using 5'-phosphoramidites [5].

2.2.4 Spotting

Lyophilized DNA was dissolved in 1× TE buffer (10mM Tris buffer and 1mM EDTA, pH 8.0) to form 100 μM DNA solutions that were stored at -20 °C. For spotting experiments, the DNA solutions were brought to room temperature and diluted to 0.02~5 μM using various buffer solutions. Spotting was performed with a single solid pin using a Microarray Spotting Station (MiraiBio Inc., South San Francisco, CA). The spotting volume of each spot was ~2 nL according to the manufacturer's specification and the spot size was about 200~260 μm in diameter. Each concentration was spotted 24 times. The relative humidity inside the spotting chamber was controlled using a humidifier to be about 50% at room temperature.

2.2.5 Post-spotting Treatment

After spotting, the slide was placed in a Corning hybridization chamber (the chamber contains two humidification wells that were filled with 10 μL of 1×TE buffer (10 mM Tris buffer and 1mM EDTA, pH 8.0)) and stored at 4 °C for 16 hours.

Following 16 hours hybridization, the slides were washed sequentially in three washing solutions: 2×SSC-0.1% SDS, 1×SSC, and 0.1×SSC, each for 5 min at room temperature with gentle stirring (the washing procedure was developed at Vanderbilt Microarray Shared Resource). The slides were blown dry with N_2 and ready for scanning. The scanner used was GenePix 4000B (Molecular Devices, Sunnyvale, CA). The scanner gain was set at 350 and the power was set as 100%. All the slides in this chapter were scanned at the same setting as above. The GenePix 4.1 software was used to obtain and analyze the scanning images. Microsoft Excel was also used to analyze the data.

2.2.6 Coverslip hybridization

To determine the uniformity of the surface and to obtain the background information of each spot, 40 μL of 2 μM complementary DNA solution (Tag #1) was pipetted on the probe region of the scanned slide (Surf A) and a 22×22 mm glass coverslip (Fisher Scientific) was used to cover the DNA solution at the surface. The slide was loaded into a hybridization chamber (Corning, Corning, NY) and the wells of the

chamber were filled with 10 μL of 1×TE buffer (10 mM Tris buffer and 1mM EDTA, pH 8.0), and the chamber was kept at 4 °C for 16 hours allowing for hybridization.

2.2.7 Probe spotting and detection

Surf B oligo slides were prepared as described in section 2.2.3 (as schematically illustrated in Figure 2.4(A)). The Probes #1 and #2 were spotted onto the slides in a patterned arrangement. The slides were incubated for 16 hours at 4 °C to allow probe attachment (Figure 2.4(B)), followed by the washing steps as described earlier in section 2.2.5. Slides were coverslip-hybridized with 40 μL of 2 μM Tag #1 and Tag #2 DNA solutions, respectively at 4 °C for 16 hours (Figure 2.4(C)). After the hybridization, the samples were washed and scanned.

2.3 Results and discussion

2.3.1 Calibration

As a goal of this work was to attach DNA probes to a surface during a spotting operation, we need estimate the amounts of attached oligonucleotide on our surfaces. To quantify the densities of attached DNA molecules, we obtained a calibration line using
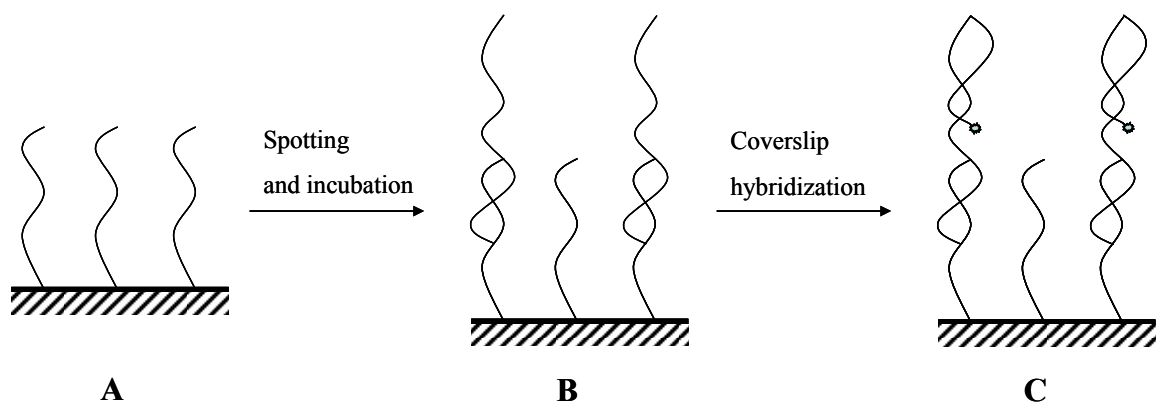
Figure 2.4. Cartoon schematics. (A) oligo DNA synthesized at surface through covalent bonding. (B) probe attachment by spotting. (C) Fluorescence DNA tags binding to the probes.

Tag #1 to relate measured fluorescence intensities from our surfaces to DNA surface density.

To quantify the surface oligo molecules from the scanning fluorescence intensity signal, a variety of Tag #1 DNA concentrations diluted in 1×TE buffer, ranging from 0.02 μM to 2 μM, were spotted on both a piranha-cleaned bare slide surface and an oligo surface. The spots were air dried and scanned without washing steps, as shown in Figure 2.5(A). In Figure 2.5(B), the obtained fluorescent intensities show a linear relationship with DNA concentrations, and the substrate surface does not affect the calibration line. The DNA concentrations can be translated into DNA surface densities, shown as the top abscissa axis.

2.3.2 Hybridization with 3× SSC and 0.05% SDS

To examine the synthesized oligo surface (Surf A in Table 2.1), the Cy3 labeled complementary DNA solution (Tag #1 in Table 2.1) were spotted onto the surface and the fluorescence signal was measured after washing steps. Researchers suggested that 3× SSC (1× SSC = 150 mM NaCl + 15 mM trisodium citrate), 0.05 % (w/v) SDS (1% SDS = 34.7 mM), and zwitterionic detergent 0.001% Chaps would be a good spotting solution [6]. Here as the first step we simply chose 3× SSC, 0.05% SDS (total $[Na^+]$ = 587 mM) as our spotting/hybridization solution. After spotting, the solutions dried in seconds and the salts crystallized at 50% relative humidity and room temperature. The slide was then loaded into the hybridization chamber, and the wells of the chamber were filled with 10 μL of 1×TE buffer for rehydating the dried spots. The
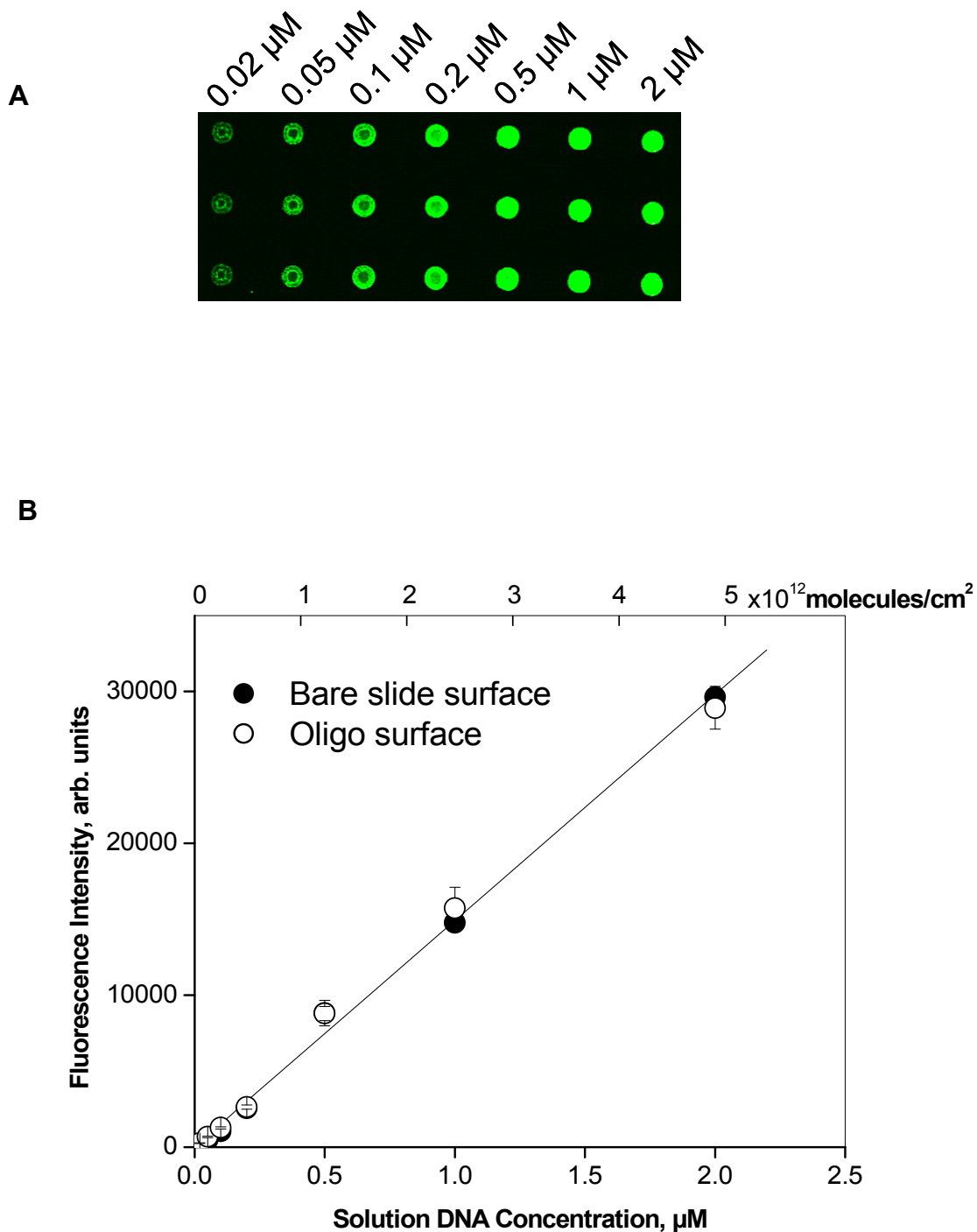
Figure 2.5. (A) Fluorescence image of various DNA Tag #1 concentrations air-dried on a bare slide surface. Each column was spotted from the same DNA spotting solution. (B) The linear relationship between the fluorescent intensity and the DNA concentrations (bottom x axis) or the corresponding surface density (top x axis). Data for two slides are shown: DNA solutions spotted on a bare slide surface are shown as solid circles, and those on an oligo surface are shown as open circles. The error bars are one standard deviation based on 20 spots. The straight line is a linear fitting for solid circles.

chamber was kept at 4 °C for 16 hours. Figure 2.6(A) shows a schematic illustration of the surface and the scanned image. The spots have a square shape and small size, and the spot diameter was set as 200 μm to obtain the mean intensity for each spot. The mean fluorescent intensity is plotted versus the target concentration, as shown in Figure 2.6(B).

A first order Langmuir isotherm, $I = \dfrac{KC}{1+KC} I_\infty$, was used to analyze the data. In this equation, I is the equilibrium intensity, and I_∞ is the intensity as the DNA concentration goes to infinity (i.e., the surface is saturated). K is the equilibrium constant between the target in solution and the surface oligos, and C is the target concentration. K and I_∞ was calculated using the double-reciprocal plot (I_∞=1/intercept, and K = intercept/slope), as shown in Figure 2.6(B) inset. Note that data points lower than 0.1 μM were not included in the reciprocal plot as the depletion effect at such low concentrations is significant. Then the intensity at each concentration was obtained using the Langmuir isotherm, which fits the data very well (Figure 2.6(B)).

However, there are a couple of concerns with Figure 2.6. First, the data do not show a plateau at higher concentrations, and we could not tell if the target has saturated the surface at the highest 5 μM target concentration. To calculate the final surface coverage, from the obtained final intensity $I_\infty \approx 5300$ (Figure 2.6(B)), the surface density of DNA duplex is about 1×10^{12} molecules/cm^2 using the calibration curve in Figure 2.5(B), which is corresponding to an average DNA target-target molecular separation distance of 10 nm, comparing with DNA width of 2 nm [7]. This indicates that theoretically the surface should be able to bind more target molecules. The second concern is that the shape of the spots looks like squares (not circular spots as expected), which also hints possible limitation during the hybridization reaction. In summary, both

A

Printing
(3xSSC, 0.05%SDS)
and incubation

Scanning

0.02 µM 0.05 µM 0.1 µM 0.2 µM 0.5 µM 1 µM 2 µM 5 µM

B
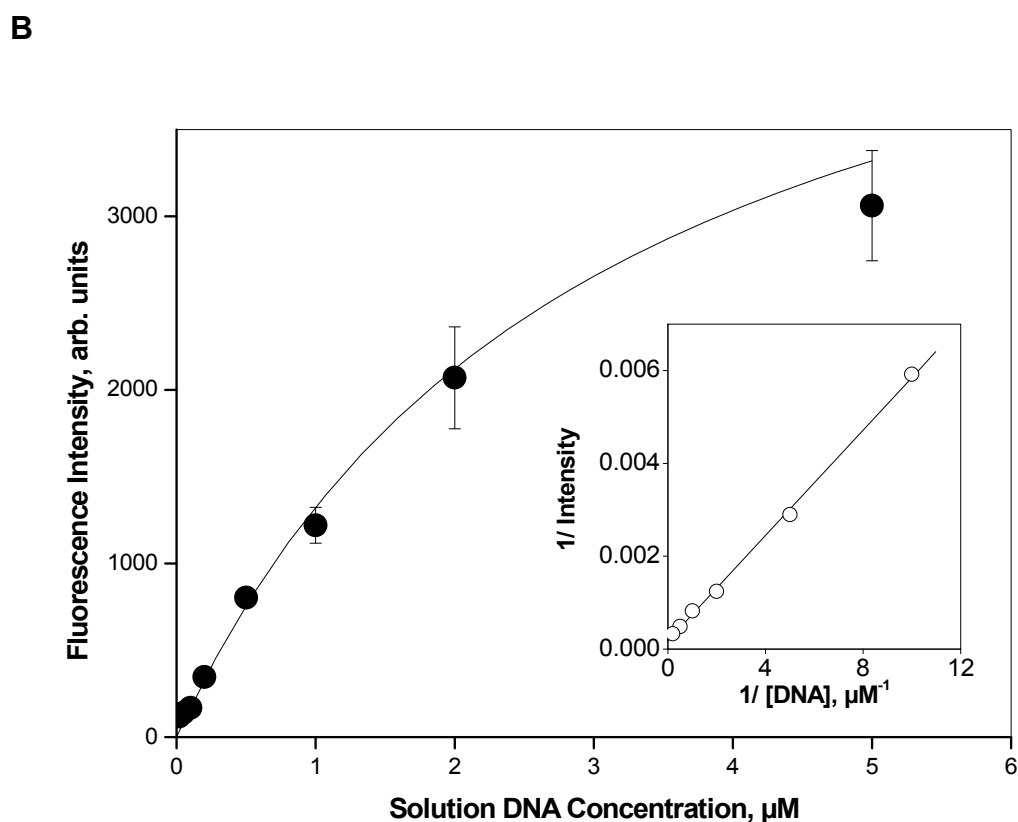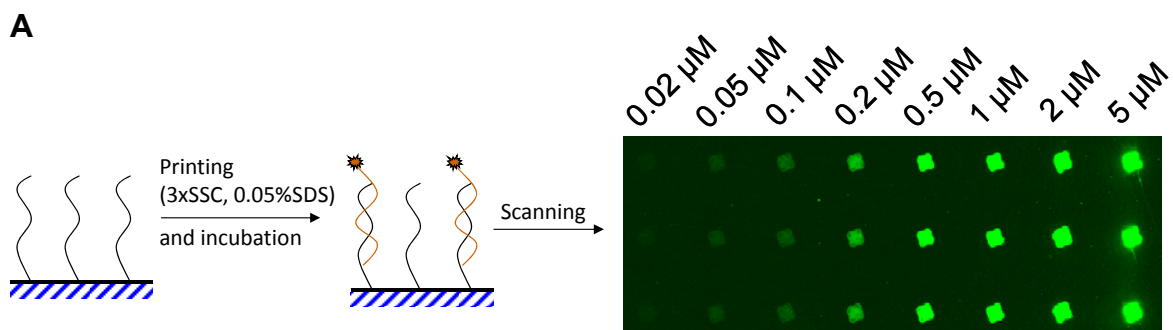
Figure 2.6. 16 hours DNA Hybridization using 3×SSC and 0.05% SDS as the printing/hybridization buffer. (A) Schematic illustration of the printing process and the fluorescence image of the spotting matrix. Each column was spotted from the same DNA solution. (B) Fluorescence intensity as a function of the spotting DNA concentrations (solid circles). The error bars are one standard deviation from the mean based on 8 spots. The curve is a Langmuir isotherm fitting, and the fitting parameters $K = 0.33$ µM^{-1} and $I_\infty = 5300$ were determined from the inset linear plot (open circles).

the low final surface coverage and the square spot shape indicate that the hybridization was limited under the experimental conditions.

To improve the hybridization signal, I initially thought the low intensity or surface coverage was probably due to the fast drying process of the spots during the printing step, and speculated higher spotting humidity would probably slow down the drying of the spots and thus help improve the fluorescence signal. To test the effect of the spotting humidity, same Tag #1 DNA solutions as in Figure 2.6(A) were spotted on a Surf A oligo slide at 80% humidity. The obtained data did not show increase on the intensity signal (not shown). I observed that the spots could not remain fully wet even during 80% humidity spotting process, and they were dried when they were transferred from the spotting station to the hybridization chamber. Since the spots are dried before they are loaded into the rehydration chamber, at what level of humidity they are prepared during the spotting process (50% or 80% humidity) does not affect the hybridization signal much. Instead, this shows that using $3\times$ SSC and 0.05 % (w/v) SDS as the spotting/hybridization solution is not appropriate. And other conditions that can keep the spots wet during the spotting process will be discussed next.

2.3.3 Hybridization with betaine and various SSC and SDS

In section 2.3.2, we learned that it is important to choose an appropriate spotting solution which allows remaining the printed spots fully wet before they are loaded into the rehydration chamber to achieve better hybridization signal. To serve this

purpose, we need find the printing solution that has minimum evaporation rate under the experimental conditions. Researchers showed that a zwitterionic and hygroscopic substance betaine (trimethylglycine) as a printing additive can give the least intraspot variation and can reduce the evaporation of the printing solution [8]. Except to betaine, detergent SDS is also applied to help reduce the evaporation of the printing solution. Although SDS was commonly used at low concentration ranging from 0.05%~0.5% for hybridization [9-11], higher concentration of SDS (7% w/v) was also used for DNA hybridization and Northern blotting analysis [12,13]. To verify the effect of betaine and SDS on hybridization, 9 spotting solutions were investigated on a Surf A oligo slide, as shown in Figure 2.7(A). The printing solutions consist of 1 μM solution DNA (Tag #1) with 17 wt.% (~ 2.9 M) betaine; SDS with various concentrations from 2.5%, 5%, to 10%; and SSC with various concentrations from 0.21×SSC, 0.42×SSC, to 0.84×SSC. The resulting [Na^+] for each solution is listed in the Figure 2.7(A). With using hygroscopic betaine, the spots remained wet during and after spotting, and the spots look round on the scanned image. The obtained fluorescent intensity roughly shows a linear relationship with the [Na^+] in solution, as shown in Figure 2.7(B), and the higher the [Na^+], the higher the fluorescence intensity. This behavior shows that sodium ionic concentration affects the equilibrium level.

Comparing to 16 hours hybridization, another slide was spotted with the same solutions but only hybridized for 4 hours (also in Figure 2.7(B)), and the data show similar intensity trend with [Na^+], indicating the hybridization underwent in the first several hours [14].
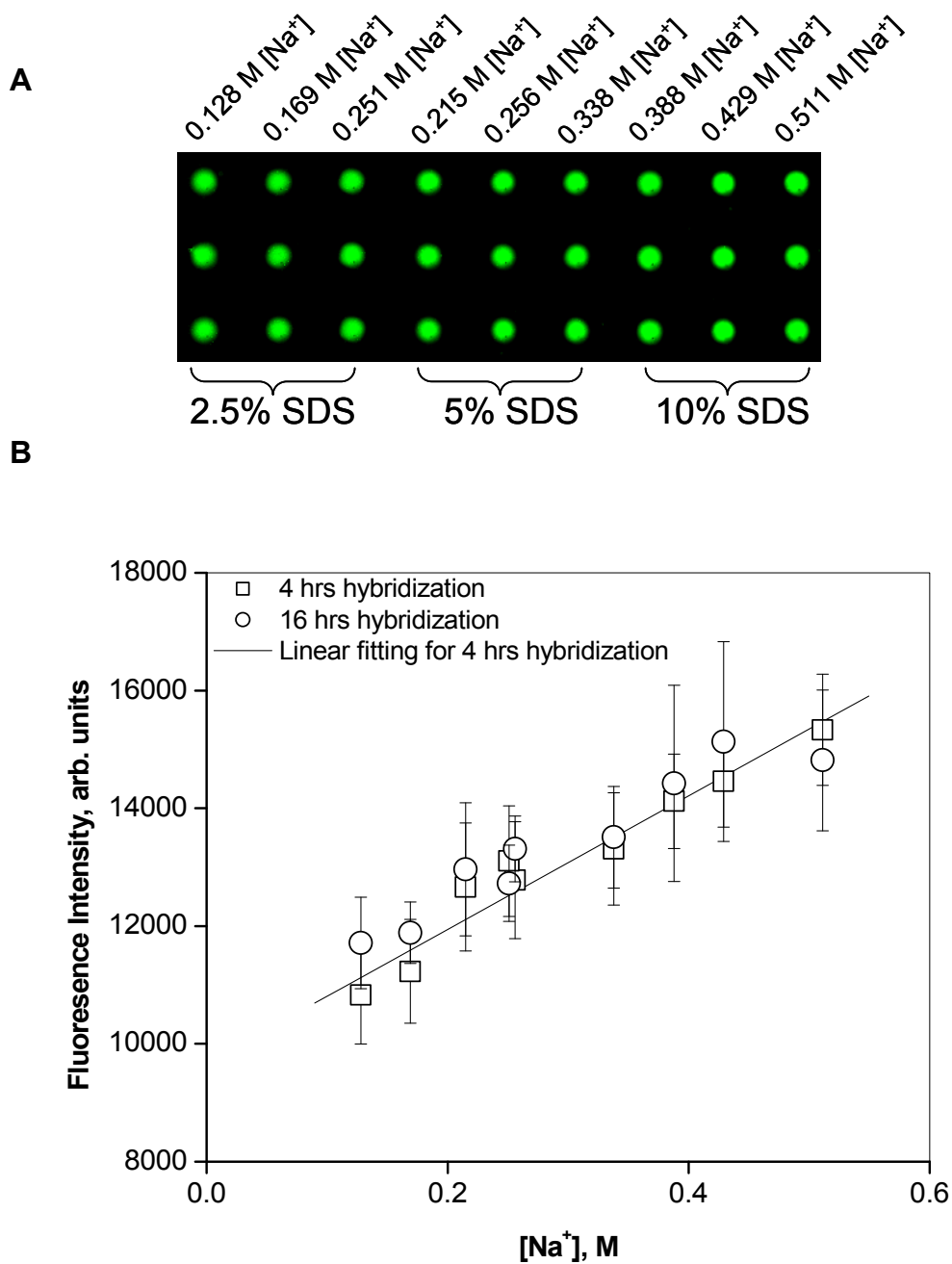
Figure 2.7. (A) Fluorescence image of 16 hour hybridization with 1 μM solution DNA with 17% betaine, various SDS and SSC (i.e., various [Na$^+$]). Each column was spotted with the same DNA solution. (B) Intensity has a linear relationship with the sodium ion concentration in the spotting/hybridization solution. Each open square represents the mean intensity from 20 replicates for 4 hours hybridization, and each open circle represents the mean intensity from 20 replicates for 16 hours hybridization. The error bars are one standard deviation of the 20 replicates. The straight line is the linear fitting for the 4 hours hybridization.

2.3.4 DNA hybridization with various concentrations in 17% betaine, 5% SDS, and 0.42×SSC

To do a parallel experiment as the one in section 2.3.2 but instead using betaine and SDS to minimize the evaporation rate of printing spots, a variety of DNA solutions were diluted in the following spotting solution: 17% betaine, 5% SDS, and 0.42×SSC ($[Na^+] = 256$ mM). The spotting solution was chosen to have a medium sodium ion concentration from Figure 2.7(A). Eight complementary DNA Tag #1 solutions ranging from 0.1 µM to 5 µM, and three noncomplementary DNA Tag #2 solutions (2 µM, 3 µM and 5 µM) were spotted on a slide, as shown in Figure 2.8(A). After 16 hours hybridization, followed by washing and scanning steps, the intensity signal from the complementary and noncomplementary solutions, and the background signal were plotted with the spotting DNA concentrations (Figure 2.8(B)). Similarly as in Figure 2.6, we plot $1/I$ vs $1/C$, and then obtain the equilibrium constant $K \approx 0.66$ µM^{-1} and $I_\infty \approx 12800$. It is clear that the intensity signal is three to four times higher when using betaine as the printing additive, as betaine kept the solution wet and thus target DNA molecules were able to diffuse to hybridize with the surface oligos. Higher DNA concentrations generate higher level of background signal after washing steps. Non-complementary DNA targets did not bind to surface oligos, and their fluorescence intensities are at the same level as the background signals. Note that the higher non-complementary signal of 2 µM Tag #2 than 5 µM Tag #2 is due to its closer location to 5 µM complementary DNA spots. As $I_\infty \approx 12800$, the DNA duplex density is about 2.1×10^{12} molecules/cm^2 from the calibration curve in Figure 2.5(B), which is corresponding to an average DNA molecule-molecule

A

Printing
(betaine, SDS, and SSC)
and incubation

Scanning

0.1 µM c 0.17 µM c 0.25 µM c 0.5 µM c 1 µM c 2 µM c 3 µM c 5 µM c 2 µM nc 3 µM nc 5 µM nc

c: complementary

nc: noncomplementary
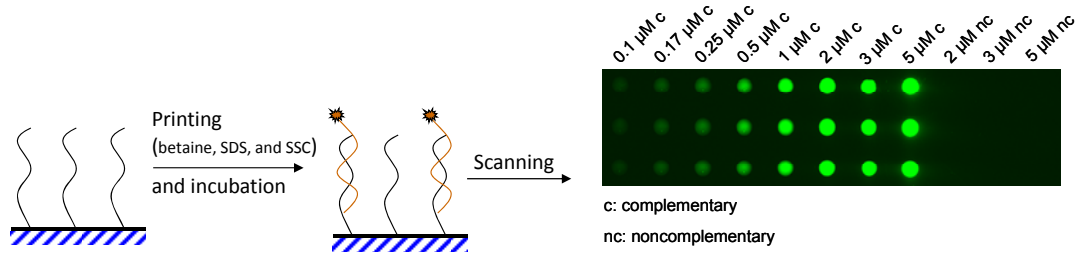
B
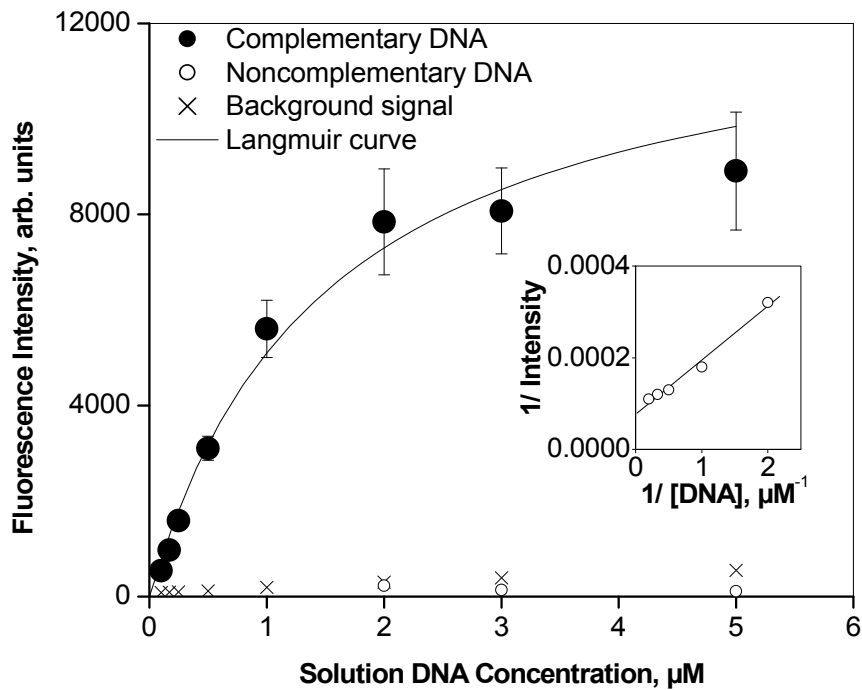
Figure 2.8. 16 hours Hybridization using 17% betaine, 5% SDS and 0.42×SSC as the printing/hybridization buffer. (A) Schematic illustration of the printing process and the fluorescence image of the spotting matrix. Each column was spotted from the same DNA solution. (B) Fluorescence intensity as a function of the spotting DNA concentrations (solid circles). The error bars are one standard deviation from the mean based on 20 spots. The cross symbols represent the corresponding background signals for each concentration. The open circles represent the mean intensity for the non-complementary solution (20 replicates for each concentration). The curve is a Langmuir isotherm fitting, and the fitting parameters $K = 0.66$ µM^{-1} and $I_\infty = 12800$ were determined from the inset reciprocal plot.

separation distance of 7 nm. This duplex density is doubled than using $3\times$ SSC and 0.05 % (w/v) SDS.

2.3.5 Printing a functional microarray

In section 2.3.4, I showed that target molecules were able to be immobilized to the surface by hybridization between targets and surface oligos. With this approach, specially designed DNA probes can be immobilized onto surface at their 5' ends, and their 3' ends are available to capture the complementary strands. Specifically, DNA probes are designed to have a common sequence at 5' ends which is used to hybridize with surface oligos and different sequences at 3' ends to provide different specific binding abilities. Figure 2.9(A) shows a proof-of-concept experiment with the spotting pattern and the scanning images of two slides. The image with double columns was hybridized with Tag #1, which is complementary to the 3' end of Probe #1. The bottom image with single column was hybridized with Tag #2, which is complementary to the 3' end of Probe #2. Figure 2.9(B) shows the obtained fluorescence intensity of these two slides. The signal/noise ratio is between 21:1 and 31:1, indicating the immobilized DNA probes have a high selectivity to their complementary strands. In addition, the similar fluorescence intensity between two step hybridization in Figure 2.9 and one step hybridization in Figure 2.8 indicates that the second step coverslip hybridization has a high efficiency.
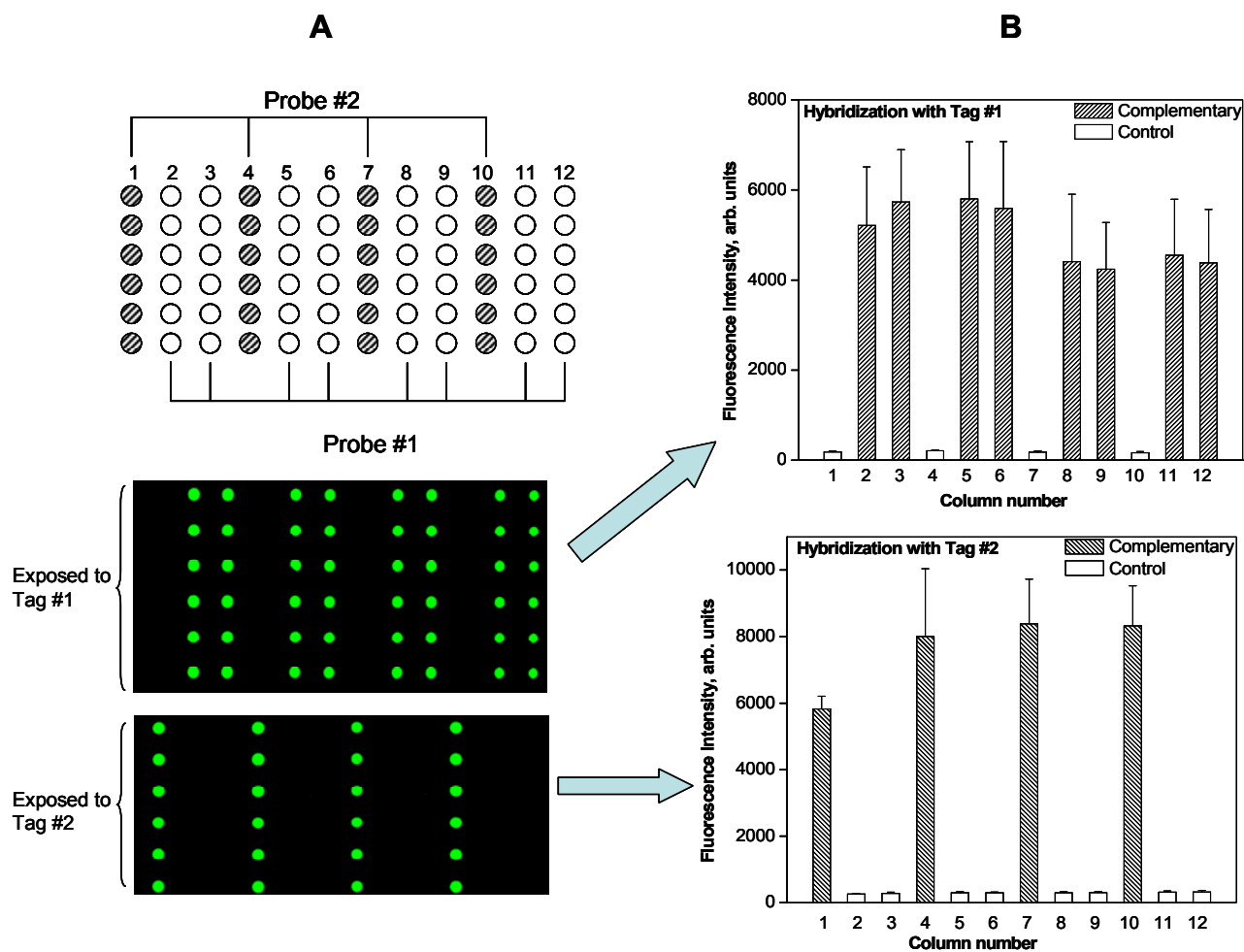
Figure 2.9. (A) Spotting pattern and scanning images of two slides. The surface immobilized DNA probes selectively captured their complementary strands. The image with double columns was hybridized with DNA Tag #1, and the bottom image with single column was hybridized with DNA Tag #2. The fluorescence data of both images are shown in (B). The intensity is the average of 20 spots with one standard deviation of the 20 spots.

2.4 Conclusions

Complementary base pair interactions between solution-surface DNA pairs can be used to end-immobilize DNA probes onto a chip surface. Patterning of end-immobilized ss-DNA strands on a chip surface can be accomplished by printing probe solutions onto covalently bound oligonucleotide surfaces using a robotic microspotter. Optimum spotting/hybridization solution with zwitterionic betaine can provide nice spot shape and good intensity signal, and signal/noise ratio. The immobilization efficiency (i.e., hybridization intensity) has a linear relationship with $[Na^+]$ in the spotting solution. The end-immobilized DNA probes are functional and selective in their binding toward secondary species containing complementary target sequences. This approach allows user preparation of microarrays with an end-immobilized architecture.

References

1   Lee, I. H., "Covalent End-Immobilization of Oligonucleotides onto Solid Surfaces", PhD Dissertation, Massachusetts Institute of Technology, 2001.

2   Porter, M. D.; Bright, T. B.; Allara, D. L.; Chidsey, C. E. D., "Spontaneously Organized Molecular Assemblies. 4. Structural Characterization of n-Alkyl Thiol Monolayers on Gold by Optical Ellipsometry, Infrared Spectroscopy, and Electrochemistry", *J. Am. Chem. Soc.* **1987**, *109*, 3559-3568.

3   Eric LeProust, H. Z., Peilin Yu, Xiaochuan Zhou, and Xiaolian Gao, "Characterization of oligodeoxyribonucleotide synthesis on glass plates", *Nucleic Acids Res.* **2001**, *29*, 2171-2180.

4   Michael C. Pirrung, L. F., and Glenn McGall, "Proofing of photolithographic DNA synthesis with 3',5'-dimethoxybenzoinyloxycarbonyl-protected deoxynucleoside phosphoramidites", *J. Org. Chem.* **1998**, *63*, 241-246.

5   Thomas J. Albert, J. N., Markus Ott, Todd, Richmond, Kate Nuwaysir, Emile F. Nuwaysir, Klaus-Peter Stengele, and Roland D. Green, "Light-directed 5' ' 3' synthesis of complex oligonucleotide microarrays", *Nucleic Acids Res.* **2003**, *31*, e35.

6   Erica D. Dawson, A. E. R., Kathy L. Rowlen, and Laura R. Kuck, "Spotting optimization for oligo microarrays on aldehyde-glass", *Anal. Biochem.* **2005**, *341*, 352-360.

7   Voet, D.; Voet, J. G.; Pratt, C. W. *Fundamentals of Biochemistry*; Upgrade ed.; John Wiley & Sons, Inc., 2001, p728.

8   Mark K. McQuain, K. S., Joel Peek, Shawn Levy, and Frederick R. Haselton, "Effects of relative humidity and buffer additives on contact printing of microarrays by quill pins", *Anal. Biochem.* **2003**, *320*, 281-291.

9   S.D. Gillmor, A. J. T., T.C. Strother, L.M. Smith, and M.G. Lagally, "Hydrophilic/hydrophobic patterned surfaces as templates for DNA arrays", *Langmuir* **2000**, *16*, 7223-7228.

10   Andrew J. Thiel, A. G. F., Claire E. Jordan, Robert M. Corn, and Lloyd M. Smith, "In situ surface Plasmon resonance imaging detection of DNA hybridization to oligonucleotide arrays on gold surfaces", *Anal. Chem.* **1997**, *69*, 4948-4956.

11   Sebastian A. Lange, V. B., Dieter P. Kem, J.K. Heinrich H?rber, and André Bemard, "Microcontact printing of DNA molecules", *Anal. Chem.* **2004**, *76*, 1641-1647.

12   Marianne Suter, a. C. R., "Fragmented mitochondrial DNA Is the predominant carrier of oxidized DNA bases", *Biochemistry* **1999**, *38*, 459-464.

13   M.T. Sanchez-Ballesta, L. Z., A. Granell, and M.T. Lafuente, "Accumulation of Pal transcript and Pal activity as affected by heat-conditioning and low-temperature storage and its relation to chilling sensitivity in Mandarin fruits", *J. Agric. Food Chem.* **2000**, *48*, 2726-2731.

14   Kevin A. Peterlinz, R. M. G., Tonya M. Herne, and Michael J. Tarlov, "Observation of hybridization and dehybridization of thiol-tethering DNA using two-color surface Plasmon resonance spectroscopy", *J. Am. Chem. Soc.* **1997**, *119*, 3401-3402.

CHAPTER III

KINETICS OF DNA HYBRIDIZATION ON A HOMOGENEOUS SURFACE

3.1 Introduction

DNA microarray technology has extensive applications in genetic investigations. It has been used for gene expression profiling [1,2], and for identifying single nucleotide polymorphisms [3] in genetic samples, as well as characterizing entire genomes. For an introduction and details on DNA microarray technology, see Chapter I. One of the key steps during the use of microarray devices is the hybridization, i.e., the interaction between target DNA molecules in a free solution and oligos immobilized on a solid surface. There have been numerous studies on DNA hybridization kinetics at surface using surface plasmon resonance (SPR) spectroscopy or SPR imaging [4-12]. Among these studies, various mathematical models have been used to extract kinetic and/or equilibrium parameters from the experimental hybridization data. These models include the most commonly used classic Langmuir model for a constant solution concentration without depletion and reaction rate limited kinetics [8,10,13], and modified diffusion-limited Langmuir models to account for mass transport effect [4,12]. Considering such diffusion-reaction problems, it is reasonable to think that the binding events are reaction-limited on the short time scale, and the kinetics becomes diffusion-limited in the long-time range [14]. Reaction-diffusion model is used to account for the kinetics which is

partially transported-limited and partially surface reaction rate-limited [14]. Although total

internal reflection fluorescence (TIRF) has been an important tool for a wide range of

applications [15], using TIRF to study DNA-DNA binding events at surface is relatively

limited [16]. In this chapter, my goals are to (1) obtain the binding kinetics of target DNA

molecules with surface oligos prepared by methods described in Chapter II with the TIRF

system as described in Chapter III; (2) investigate the effects of target DNA

concentrations, and salt concentrations to the binding kinetics and equilibrium; (3) use

the diffusion-reaction model to analyze the experimental kinetics data and extract the

equilibrium and kinetics parameters and compare them with available literature data; (4)

analyze the depletion effect in the bulk solution under different target DNA

concentrations.

3.2 Methods and Materials

Slide preparation. Microscopic slides were cleaned in piranha solution (7:3(v/v),

concentrated H_2SO_4 : 30% H_2O_2. Caution: "piranha" solution reacts violently with

organic material and should be used with great care.) for 30 min, followed by rinsing

with copious quantities of DI water and drying under a N_2 stream. The slides were then

immersed into a 1 wt.% N-(3-triethoxysilylpropyl)-4-hydroxy-butyramide (Gelest,

Morrisville, PA) solution in 95% ethanol for 16 hours to produce a hydroxyl silane

surface. The slides were removed from the silane solution, rinsed sequentially with

ethanol and water, and then blown dry with N_2. Then the slides were heated in an oven at ~110 °C for 30 min to anneal the films. Surface oligonucleotides were synthesized from the hydroxyl group using phosphoramidite chemistry (see Chapter II).

Oligonucleotide sequences. The sequence of the synthesized end-immobilized surface oligos was Surface-3'-TTTTTGCCTCCACGATT-5'. The sequence of fluorescently-tagged target was 5'-CGGAGGTGCTAAGAT Cy3 -3' (Integrated DNA Technologies, Coralville, IA.). The target DNA strands were modified with the fluorescent dye Cy3 at the 3' end.

Target DNA solutions. (1) For hybridization under various target concentrations, four different target concentrations were used: 0.2 μM, 0.35 μM, 0.5 μM, and 0.7 μM. All the four solutions were prepared in 0.5M NaCl containing TE buffer (10mM Tris buffer (pH 8.0) and 1mM EDTA). (2) For hybridization under different salt concentrations, two NaCl concentrations were used: 0.1M NaCl or 0.5M NaCl. Both solutions were prepared at 0.35 μM target concentration containing 1× TE buffer (10mM Tris buffer and 1mM EDTA, pH 8.0).

TIRF instrument. A TIRF system was constructed for measurements of DNA hybridization kinetics at surface. Shown in Figure 3.1(A) is the schematic illustration of the experimental TIRF system. The light source was a diode-pumped solid-state (DPSS) laser that emitted light at a wavelength of 532 nm and an output power at 30 mW (Laserglow Technologies, Toronto, Canada). The diameter of the produced laser spot was about 1~2 mm. The laser beam was expanded by passing the light through a plano-

A

CCD Camera
with lens

Emission Filter

DNA chip

Flow cell

Coupling fluid

Expanded
laser beam

Dove prism

Y

X

B

PDMS channel

Load DNA solution

1D oligo sample
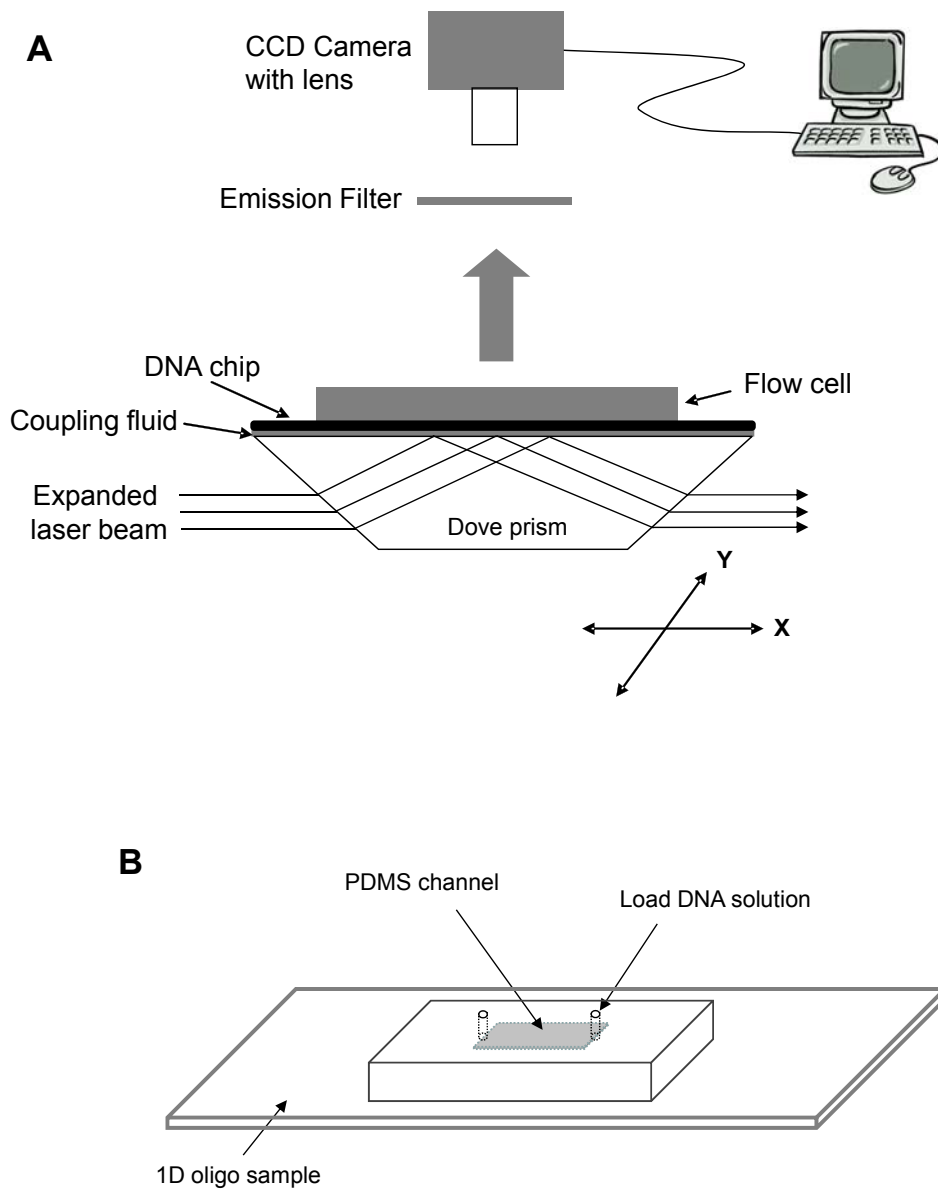
Figure 3.1. Schematic illustrations of (A) a TIRF system for measuring hybridization kinetics on a DNA chip surface, and (B) the PDMS channel covering a 1D oligo surface.

concave lens (material N-BK7, standard broadband AR coating for wavelength 350~700 nm, dia = 12.7 mm, f = -25.0 mm, Thorlabs, Newton, NJ) and a plano-convex lens (material N-BK7, standard broadband AR coating for wavelength 350~700 nm, dia = 25.4 mm, f = 250.0 mm, Thorlabs, Newton, NJ), consecutively. A normally closed beam shutter (Thorlabs, Newton, NJ) was placed between the laser and the concave lens to allow sub-millisecond shutter operations using a shutter controller (Thorlabs, Newton, NJ). The expanded laser beam size was further adjusted using an Iris Diaphragm with a maximum aperture size of 20.0 mm (Thorlabs, Newton, NJ), and then passed through a dove prism and totally internal reflected at the interface (see Figure 3.1(A)). The DNA chip surface was attached to the prism surface by using a couple of drops of index-matching oil (Cargille Laboratories, Cedar Grove, NJ). The emitted fluorescent light above the chip surface passed through an emission filter (Omega Optical, Brattleboro, VT), and a macro video lens (Optem International), and was detected by a Retiga 1300 CCD camera (QImaging, Surrey, BC, Canada). The camera and the shutter controller were connected to a PC, and controlled using custom-written MATLAB code.

For DNA hybridization studies, the oligonucleotide slide surface was covered with a PDMS channel, as shown in Figure 3.1(B). The channel was 22 mm long, ~10 mm wide and ~ 200 µm thick. To prepare the PDMS channel, a piece of 22×22 mm microscope cover glass (Fisher Scientific) was cut into halves, and one half of the glass coverslip (22 mm long, ~10 mm wide, and ~200 µm thick) was placed onto a plain microscope glass slide surface (75 mm long, 25 mm wide, and 1mm thick), and a drop of

water was applied between the coverslip and the glass slide to help them connect with each other, then vacuum degassed PDMS pre-polymers were poured onto the coverslip/glass slide surface. The PDMS pre-polymers were made by a 10:1 ratio (w:w) mixture of SYLGARD silicone elastomer 184 and SYLGARD silicone elastomer 184 curing agent (Dow Corning Corporation, Midland, MI). After curing the PDMS at 80 °C for one hour, the stamp was peeled off the slide surface, and a rectangular channel was formed on the PDMS surface, which was a negative from the shape of the coverslip on the slide surface. There were two holes drilled at each end of the channel which allow adding target DNA solutions to the channel and contact with surface oligonucleotides. In all hybridization experiments, 70 μL target DNA solutions were added into the channel through one of the two holes. The slide and the PDMS channel were coupled to the prism surface using a couple of drops of index-matching oil as mentioned above (Type DF, Cargille Laboratories, Cedar Grove, NJ).

Hybridization kinetics. In a typical hybridization kinetics experiment, the Retiga 1300 CCD camera (QImaging, Surrey, BC, Canada) was first started to acquire images from the surface every one second, and then 70 μL target DNA was pipetted into the PDMS channel in about one second. The time series of the fluorescent images at surface were recorded using the camera controlled in the MATLAB environment. The data were acquired and analyzed using custom-written MATLAB code. The size of the region of interest from the image was chosen as 60×60 pixels, and each pixel has a surface area of $400 \ \mu m^2$. The surface was regenerated for multiple hybridization experiments by rinsing

it sequentially with 65°C DI water and room temperature DI water, and then the slide was blown dry under N_2.

Numerical method. The partial differential equation (eq (3.4)) was solved numerically by approximating the left side by a forward first order difference quotient in τ and the right side by a centered second order difference quotient in $\tilde{y}$ [17]. In the y direction, the height was divided into 100 equal parts, thus the first part, which was the closest to the surface, was about 2 μm thick since the whole channel height was ~ 200 μm. The dimensionless time τ was set between zero and 0.6, with a step interval of 0.00005. To calculate the surface coverage θ, the ordinary differential equation (eq 3.5b,

$$\frac{d\theta}{d\tau} = \left[\tilde{k}_a \cdot \tilde{C}(\tilde{y} \to 0, \tau)(1 - \theta) - \tilde{k}_d \theta\right] at \ \tilde{y} = 0$$

) was solved analytically and θ was calculated at each time step, assuming the target concentration 2 μm above the surface $\tilde{C}(\tilde{y} \to 0, \tau)$ a constant during each time step.

The calculated kinetics data were fitted with the experimental data (Figure 3.4). The fitting parameters were the association rate constant k_a, the dissociation constant K_D, and the surface probe density P_0. The best fitting values of these variables were determined using nonlinear least squares fitting with Gauss-Newton line-search algorithm. The code was custom-written in MATLAB 7.4.0 environment.

3.3 Results and discussion

3.3.1 Hybridization kinetics with various target concentrations

Shown in Figure 3.2 is the hybridization kinetics of target DNA molecules at different concentrations (0.2 µM, 0.35 µM, 0.5 µM, and 0.7 µM) in 0.5 M NaCl. For all four targets, the surface fluorescent intensity increases fast between 0 and ~70 seconds. At selected reaction times, the higher target DNA concentration, the higher fluorescent intensity. After 100 seconds, the surface reaches the saturation/equilibrium state, and the level of final intensity is corresponding to the target concentration. The flatness of the equilibrium data indicates there is negligible photobleaching under experimental conditions.

The fluorescence intensities in Figure 3.2 can be normalized if we know the final fluorescence intensity when the surface is 100% saturated. Next the Langmuir isotherm is used to determine the value of the final fluorescence intensity. The reciprocal form of Langmuir isotherm is

$$\frac{1}{I(C_0, t \to \infty)} = \left[\frac{1}{K \cdot I_{final}} \right] \frac{1}{C_0} + \frac{1}{I_{final}} , \qquad (3.1)$$

where $I(C_0, t \to \infty)$ represents the equilibrium fluorescent intensity at target concentration C_0, K is the equilibrium constant, I_{final} is the final fluorescent intensity as C_0 goes to infinity and reaction time goes to infinity. The equilibrium data in Figure 3.2 is chosen and fitted using eq (3.1) to obtain final intensity I_{final} and the equilibrium constant K

61
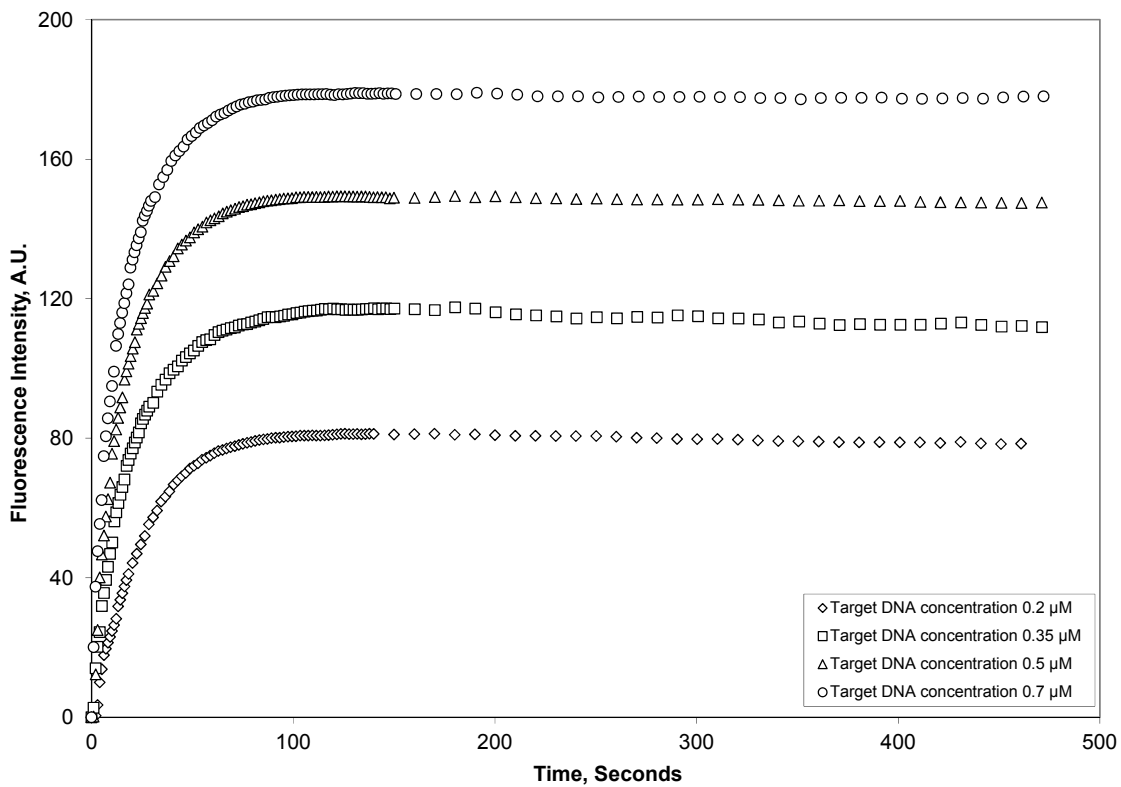
Figure 3.2. Hybridization kinetics of four different target DNA concentrations in 0.5M NaCl. All the four targets were hybridized to the same surface oligos repeatedly.

(Figure 3.3). From the intercept and the slope, we have $I_{final} = 339$, and $K = 1.56 \ \mu M^{-1}$.

The dissociation equilibrium constant $K_D = 1/K = 0.64 \ \mu M$.

With I_{final} known, the kinetics data (taken at reaction time between 0 and 150

seconds) in Figure 3.2 are normalized by defining the surface coverage of DNA duplexes,

$\theta(t) = I(t)/I_{final}$, where $I(t)$ is the fluorescent intensity at time t. The normalized kinetics

data are shown in Figure 3.4.

3.3.2 Diffusion-reaction model

In the hybridization experiments, target DNA molecules were loaded into a

rectangular PDMS channel with height h, and transported by diffusion to reach the

surface and interact with surface oligos. Since the width and length of the PDMS channel

are 20~50 x greater than its height, we assume the diffusion in both the width and length

directions are negligible. If we take y axis as the direction normal to the surface, $y = 0$ is

the solid/solution interface, and $y = h$ is the top wall of the channel. As there is no flow

in the channel, the mass transport of target DNA in the solution phase is governed by the

following 1-D diffusion equation:

$$\frac{\partial C}{\partial t} = D\frac{\partial^2 C}{\partial y^2}, \qquad\qquad (3.2)$$
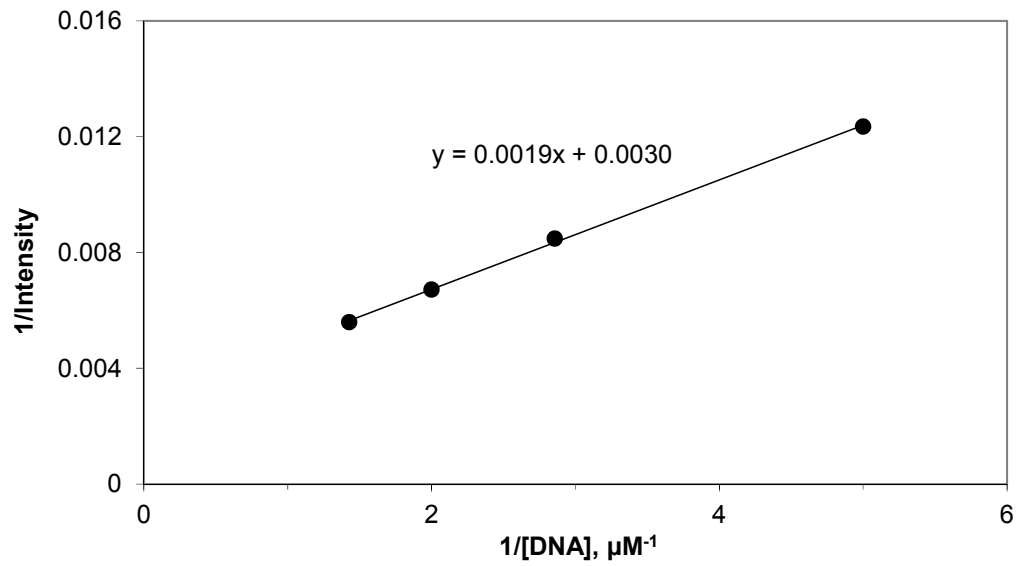
Figure 3.3. Langmuir Isotherm plot. $1/I(C_0, t\to\infty)$ has a linear relationship with $1/C_0$.
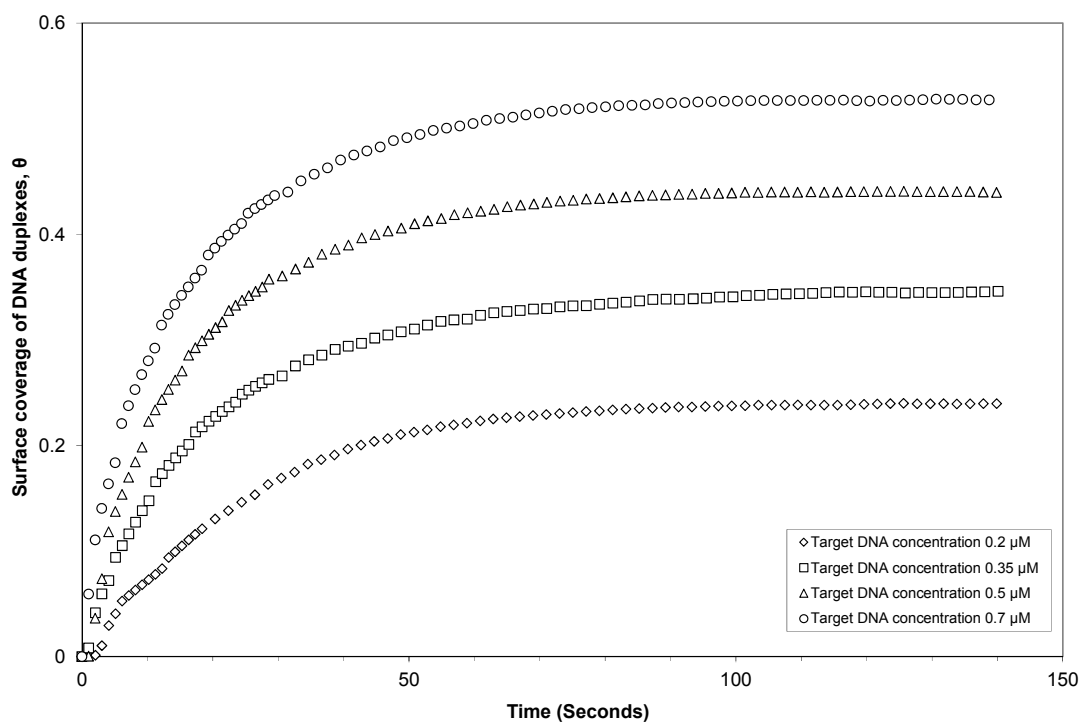
Figure 3.4. Hybridization kinetics of four different target DNA concentrations in 0.5 M NaCl (normalized surface coverage *vs* time). All the four targets were hybridized to the same surface oligos repeatedly.

where C is the target concentration in solution, which is a function of position y and time t ($C = C(y,t)$), and D is the diffusion coefficient of target DNA molecules in solution (see section 3.3.3). With an impermeable and inert surface at $y = h$, we have

$$\frac{\partial C}{\partial y} = 0 \qquad at \quad y = h.$$ (3.3a)

While at the solid/solution interface, the diffusive flux of target should equal the surface reaction rate

$$D\frac{\partial C}{\partial y} = \frac{dH(t)}{dt} = k_a C(y \to 0,t)P(t) - k_d H(t) \qquad at \quad y = 0,$$ (3.3b)

where $H(t)$ is the surface density of the DNA duplexes, $\#/cm^2$, k_a is the association rate constant, $M^{-1}s^{-1}$, k_d is the dissociation reaction rate constant, s^{-1}, $C(y \to 0,t)$ is the target DNA concentration just above the oligo surface, and $P(t)$ is the surface density of available probe DNA sites, $\#/cm^2$. The available probe sites $P(t) = P_0 - H(t)$, here P_0 is the initial surface density of available DNA probes.

At the beginning of the reaction ($t = 0$), the target concentration everywhere inside the channel is equal to C_0, and surface coverage of DNA duplexes at $t = 0$ is equal to zero. Thus the initial conditions are $C(y, t = 0) = C_0$ and $H(t = 0) = 0$. Using dimensionless groups defined as $\widetilde{C} \equiv \frac{C}{C_0}$, $\theta(t) \equiv \frac{H(t)}{P_0}$, $\widetilde{y} \equiv \frac{y}{h}$, $\tau \equiv \frac{Dt}{h^2}$, $\widetilde{k}_a \equiv \frac{k_a C_0 h^2}{D}$, and

$\widetilde{k}_d \equiv \frac{k_d h^2}{D}$, eqs (3.2-3.3) can be transformed as follows [18]

$$\frac{\partial \widetilde{C}}{\partial \tau} = \frac{\partial^2 \widetilde{C}}{\partial \widetilde{y}^2},$$ (3.4)

$$\frac{\partial \widetilde{C}}{\partial \widetilde{y}} = 0 \qquad at \quad \widetilde{y} = 1,$$ (3.5a)

66

$$\frac{C_0 h}{P_0} \frac{\partial \tilde{C}}{\partial \tilde{y}} = \frac{d\theta}{d\tau} = \left[\tilde{k}_a \cdot \tilde{C}(\tilde{y} \to 0, \tau)(1-\theta) - \tilde{k}_d \theta \right] \qquad at \ \tilde{y} = 0 \qquad (3.5b)$$

with initial conditions of $\tilde{C}(\tilde{y}, \tau = 0) = 1$ and $\theta(\tau = 0) = 0$.

3.3.3 Diffusion coefficient, D

The translational diffusion coefficient of a rigid rod DNA molecule with length L and diameter d is given by the following expression [19-22]:

$$D = \frac{k_B T}{3\pi\eta L} \left[\sigma - \frac{1}{2}(\gamma_\perp + \gamma_\parallel) \right], \qquad (3.6)$$

where D is the translational diffusion coefficient, k_B is Boltzmann's constant, T is the absolute temperature, and η is the viscosity of the solvent. Parameters σ and end-effect corrections $\gamma_\perp$ (translating perpendicularly) and $\gamma_\parallel$ (translating parallel) are given as

$$\sigma = \ln\left(\frac{2L}{d}\right), \qquad (3.7a)$$

$$\gamma_\perp = -0.193 + 0.15\sigma^{-1} + 8.1\sigma^{-2} - 18\sigma^{-3} + 9\sigma^{-4}, \qquad (3.7b)$$

$$\gamma_\parallel = 0.807 + 0.15\sigma^{-1} + 13.5\sigma^{-2} - 37\sigma^{-3} + 22\sigma^{-4}. \qquad (3.7c)$$

The expression is valid for $0 \le 1/\sigma < 0.45$ [21].

The contour length of one monomer for ssDNA is 0.43 nm, and the diameter of ssDNA backbone is about 1.1 nm [23]. The viscosity of the solvent η is taken as 0.001 Pa•s, and temperature T is at 293 K. Using the rigid model, we can obtain the

translational diffusion coefficient D for 15-mer ssDNA molecules in an aqueous solution

as

$$D = 1.15 \times 10^{-6} \text{ cm}^2/\text{s}$$

For comparison, the experimental diffusion coefficient for an 18-mer ssDNA in 7 M urea

at 30 °C was measured by capillary electrophoresis as $(0.98 \pm 0.04) \times 10^{-6} \text{cm}^2/\text{s}$ [23].

3.3.4 Fitting the experimental data

The diffusion-reaction model was used to globally fit the experimental kinetics

data (Figure 3.4) at various target concentrations. The fitting curves are shown in Figure

3.5. The three fitting parameters are the association rate constant k_a, the equilibrium

dissociation constant K_D, and the surface probe density P_0. The dissociation rate constant

is then calculated as $k_d = K_D \cdot k_a$, and the equilibrium constant is calculated as $K = 1/K_D$.

The diffusion coefficient D is determined as in section 4.3.4 and used as a constant. The

obtained values of parameters k_a, k_d, K, P_0, and D are listed in Table 3.1, and compared

with literature data. Direct comparison of the data is difficult as the oligonucleotide

length and sequence, surface chemistry for immobilization of oligos, probe density, ionic

strength are all different. However, it is clear that the associate rate constant k_a for 12-

mer (this work) is at the same order of magnitude as those 15-mer, 16-mer or 22-mer

obtained using various surface measurements. For comparison, the dissociation rate k_d

for 12-mer (this work) is about 2 to 3 orders of magnitude higher than those oligomers,
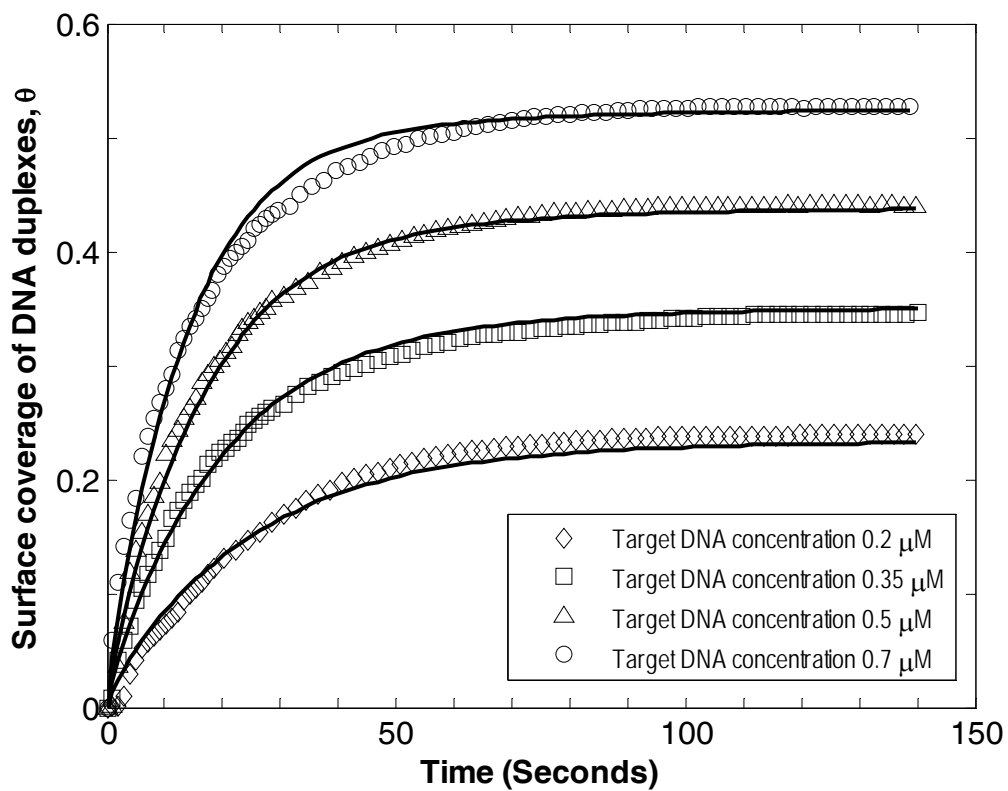
Figure 3.5. Global fitting of the experimental kinetics data by the diffusion-reaction model. The lines are fitting curves. The experimental data are taken from Figure 3.4.

Table 3.1 Association and dissociation rates (k_a and k_d), equilibrium constant K, probe density P_0 and diffusion coefficient D from this work, and compared with literature data

oligo length	k_a ($\times 10^{-4}$) M^{-1}s^{-1}	k_d ($\times 10^4$) s^{-1}	K ($\times 10^{-7}$) M^{-1}	P_0 ($\times 10^{-12}$) #/cm^2	Method	Reference
12-mer	7.2	420	0.17	1.1	TIRF; Diffusion-reaction model; 0.5 M NaCl, target 0.2~0.7 µM; no flow.	this work
15-mer	6.58	1.32	49.8	2.9	SPDS; Langmuir model; HBS-EP buffer (including 150 mM NaCl), target 1 µM; no flow.	24
15-mer	4.6	0.4	115	N/A	SPFS; Langmuir model; 50 nM target in phosphate buffer at pH 7; no flow.	25
16-mer	7.0	0.61	110	11	SLCFM; Langmuir model; 6×SSPE buffer (including 1 M NaCl), target 1~100 nM; flow rate at 80 ml/min.	13
22-mer	9.0	2.2	41	0.52	TIRF; Extended Langmuir model with depletion consideration; 1~10 nM in 3×SSC hybridization buffer containing 0.01% SDS (w/v) and 1mM EDTA; no flow.	26
12-mer (solution phase)	440	81	54	N/A	Stopped-flow kinetics; DNA target 5 µM, DNA ligand 0.5 µM, both in 100 mM NaCl, 10 mM MgCl2, and 10 mM Na•PIPES.	27

TIRF: total internal reflection fluorescence; SLCFM: scanning laser confocal fluorescence microscope; SPDS: surface plasmon diffraction sensor; 6×SSPE buffer: 1 M NaCl, 0.07 M Na$_2$HPO$_4$, and 0.07 M ethylenediaminetetraacetic acid [EDTA], pH 7.8; HBS-EP: degassed 10 mM HEPES buffer saline, pH 7.4, 150 mM NaCl, 3 mM EDTA, 0.005% v/v surfactant P-20; SPFS: surface plasmon enhanced fluorescence spectroscopy; EDTA: ethylenediaminetetraacetic acid

which indicates that the 12-mer is much easier to dissociate from the surface and less

stable, and the dissociate rate constant is probably more sensitive to the sequence length

than the associate rate constant, especially when the sequence length is shorter than 15-

mer. In Table 3.1, the rate constants of 12-mer measured on surface is also compared

with those of a 12-mer (with different sequence) in solution phase obtained by stopped-

flow kinetics. Both association and dissociation rates for solid phase are slower than

those for solution phase, and the equilibrium constant is also two orders of magnitude

lower [28].

　　　　To test the sensitivity of the diffusion-reaction model to the value used for the

diffusion coefficient, the model was used to fit the kinetics data by using either 80% or

120% of the calculated value (section 4.3.3). Table 3.2 lists fitting values of adsorption

and desorption rates (k_a and k_d), equilibrium constant K, probe density P_0 at three

different values of diffusion coefficient: 1.15×10^{-6} cm^2/s (calculated value D, section

4.3.4), 0.92×10^{-6} cm^2/s ($0.8D$), and 1.38×10^{-6} cm^2/s ($1.2D$). It shows that the diffusion-

reaction model is not sensitive to the diffusion coefficient in the range of decreasing or

increasing D by 20%.

3.3.5 Depletion in the solution phase

　　　　Under surface hybridization conditions, the increase of hybridized molecules at

surface is equal to the loss of molecules in the bulk solution [26]. Depending on the probe

Table 3.2 Sensitivity analysis for diffusion coefficient D (cm^2/s)

	k_a	k_d	K	P_0
	$(\times 10^{-4})$	$(\times 10^{2})$	$(\times 10^{-7})$	$(\times 10^{-12})$
	$M^{-1}s^{-1}$	s^{-1}	M^{-1}	$\#/cm^2$
$D = 1.15 \times 10^{-6} cm^2/s$	7.2	4.2	0.17	1.1
80% of D	7.3	4.3	0.17	1.0
120% of D	7.1	4.2	0.17	1.1

density and solution concentration, the change in the bulk concentration might have a significant effect on the hybridization kinetics, and determines if Langmuir model applies or not since the classic Langmuir model assumes a constant solution concentration. It is challenging to estimate the depletion effect near the surface experimentally. To allow using a Langmuir model to analyze the data, researchers have used a peristaltic pump to circulate the target solution to remove the transport limitation [13]. However, for standard DNA hybridization experiments, the targets are often not flowing or circulating across the surface. Under these circumstances, the target concentration profile above the surface provides useful information on how much depletion in solution and the dynamics of the solution concentration at the interface. Such information is readily available from a diffusion-reaction model.

Figure 3.6 shows four normalized target DNA concentration profiles at the position just 2μm above the surface, each line represents a different initial target concentration. The profiles give details of the dynamics of target concentration just above the surface. At the first 10 to 20 seconds, the concentrations are depleted by about 25% due to surface reactions, and then the concentrations relatively slowly back up to the equilibrium concentrations as the surface reaction rates slow down and finally reach their equilibrium states. Among the four concentrations, the lowest initial concentration, 0.2 μM, has the most depletion initially, and also has the lowest equilibrium bulk concentration.

The normalized target concentration profiles along the y-axis at different reaction times are shown in Figure 3.7 (Figure 3.7(A) at an initial target concentration of 0.2 μM, and Figure 3.7(B) 0.5 μM). The time interval between the lines is 4 s. Initially,

73

the target concentration is normalized as one everywhere. As the surface reaction starts,

target molecules in the solution phase bind to surface and immediately cause depletion in

solution. This forward reaction rate is dominant at the beginning stage, and causes the

depletion zone more and more evident. While the reaction time increases, the forward

reaction rate slows down as the target concentration just above the surface depletes

(Figure 3.6) and the available probe sites decreases; at the same time, the surface density

of DNA duplexes increases and thus the reverse reaction rate becomes more and more

significant. Consequently the total surface reaction rate slows down, and transported

target molecules through diffusion gradually fill up the depletion zone. Finally, the

forward and reverse reaction rate reaches equilibrium and the target concentration in

solution becomes homogeneous and the depletion zone disappears. At different initial

target concentrations, here I am comparing 0.2 µM to 0.5 µM, the target concentration

profiles are similar but there is slightly more depletion and lower equilibrium

concentration at 0.2 µM, and this observation is consistent with that in Figure 3.6.
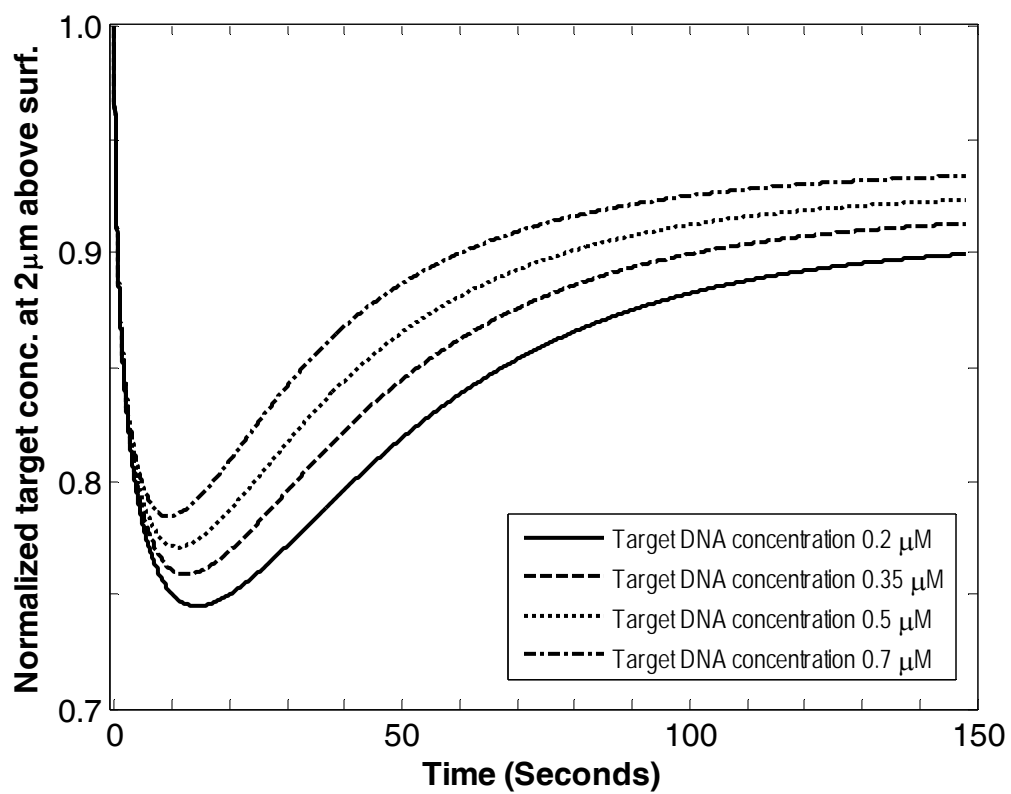
Figure 3.6. Target DNA concentration 2 μm above the surface changes with time. Each line represents different starting target concentration.

A
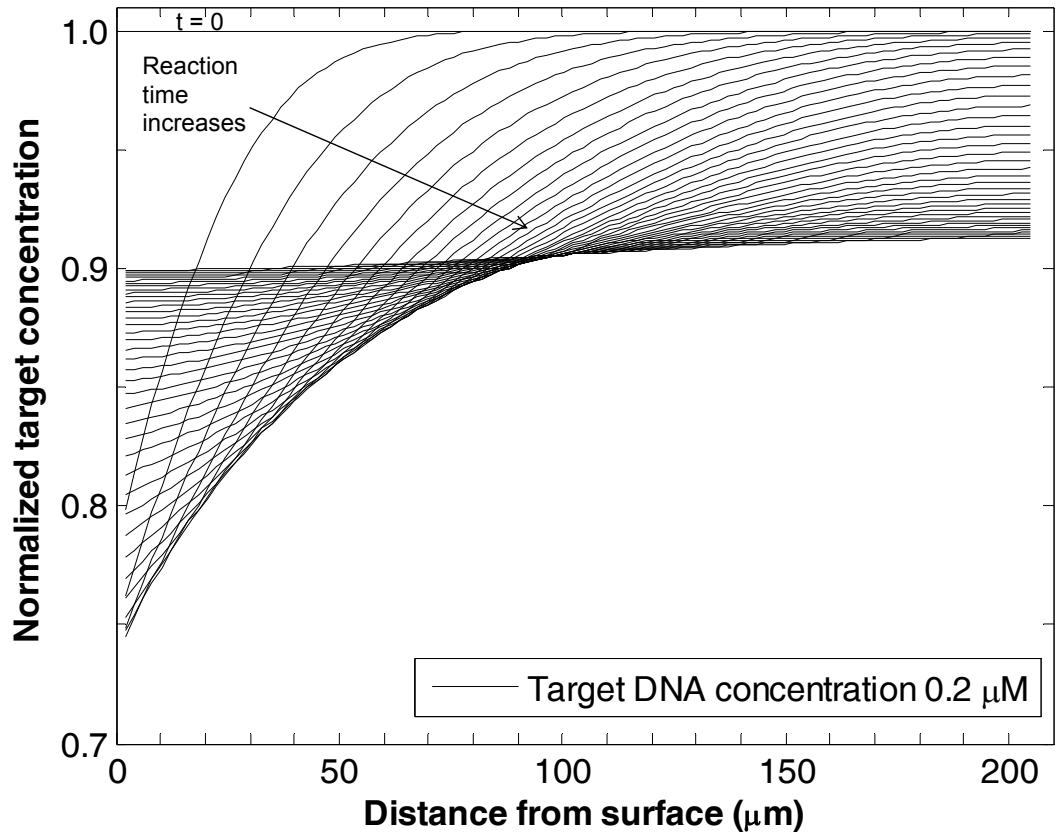
B
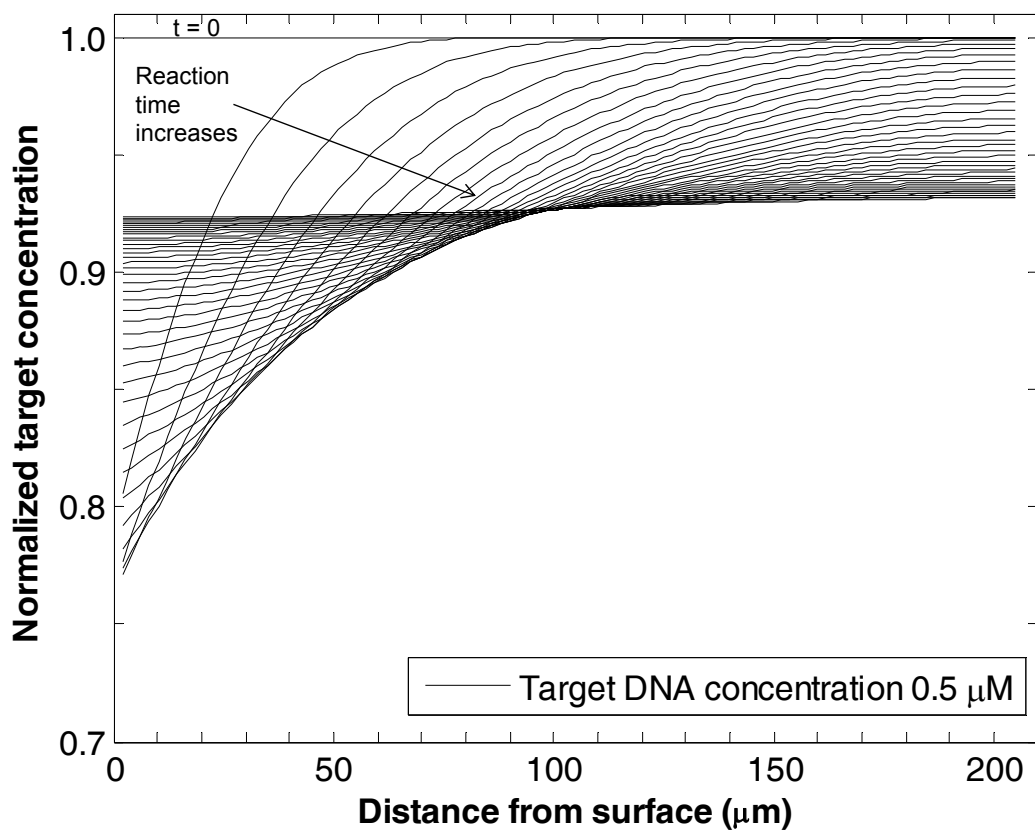
Figure 3.7. Normalized target concentration profiles along *y*-axis with reaction time interval of 4 s at two selected initial target concentrations: (A) 0.2 μM and (B) 0.5 μM.

3.3.6 Salt concentrations

The stability of hybridized DNA duplexes at surface is related to salt concentrations (Chapter II, Figure 2.7). Literature data are often obtained under various conditions (salt concentration, buffer solution, target concentration, etc.), which makes direct comparison of data difficult (for example, see this chapter, Table 3.1). In this section, two sets of hybridization kinetics data under different salt concentrations are presented. The target concentration was held constant at 0.35 μM, and the salt concentration was at either 0.1 M NaCl or 0.5 M NaCl (Figure 3.8). The equilibrium surface coverage of DNA duplexes at 0.5 M NaCl is much greater (a factor of 3) than that at 0.1 M NaCl. At 0.1 M NaCl, the target DNA reaches and maintains a surface coverage of 0.11 in less than 40 s, while at 0.5 M NaCl, the target DNA reaches and maintains a surface coverage of 0.34 in less than 90 s. The two data sets were fitted by the diffusion-reaction model separately. The fitting parameters were association rate k_a and equilibrium dissociation constant K_D. The diffusion coefficient D, and probe density P_0 were set as constants, and $D = 1.15 \times 10^{-6}$ cm^2/s, and $P_0 = 1.1 \times 10^{12}$ #/cm^2 for both salt concentrations. The obtained association and dissociation rates (k_a and k_d), and equilibrium constant K are listed in Table 3.3. By decreasing the salt concentrations from 0.5 M NaCl to 0.1 M NaCl, the association rate decreases by 40% while the dissociation rate increases by a factor of 2.6, indicating the dissociation rate is more sensitive to ionic strength in solution than the association rate. As equilibrium constant $K = k_a/k_d$, both changes in k_a and k_d contribute to the decrease of K.
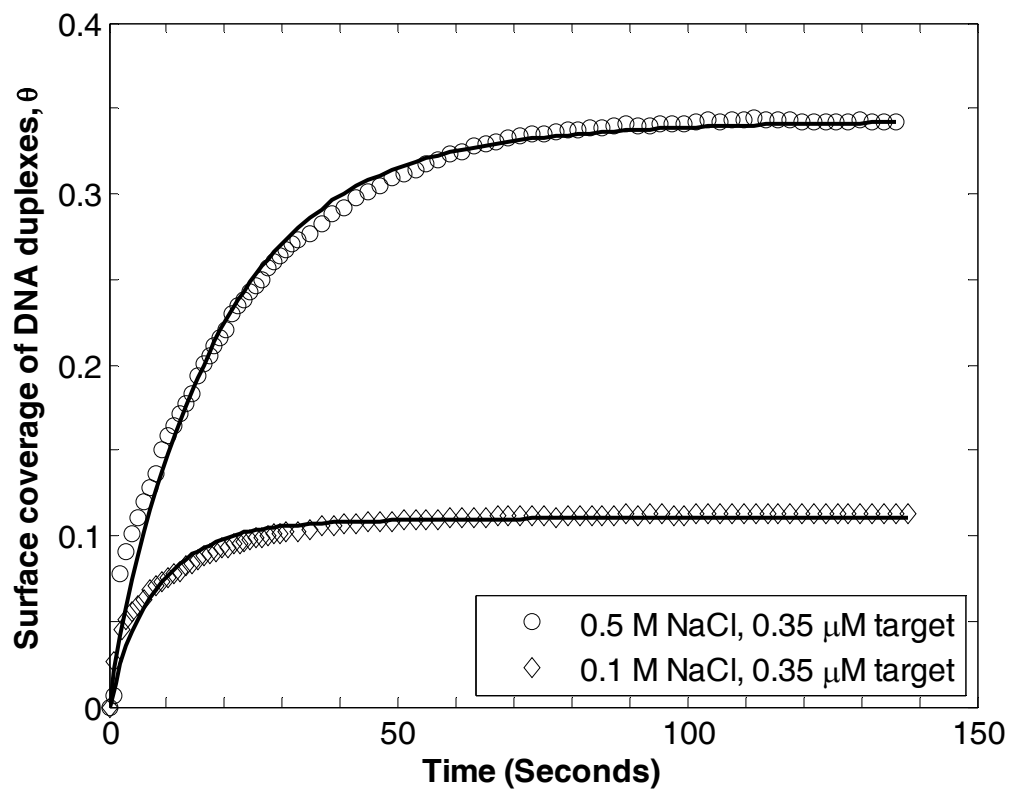
Figure 3.8. Hybridization kinetics at two different salt concentrations: 0.1 M or 0.5 M NaCl. The target DNA was the same at 0.35 μM. The lines are the fitting curves (note: two separate fittings, not global fitting) to the experimental data using the diffusion-reaction model.

Table 3.3 Association and dissociation rates (k_a and k_d), and equilibrium constant K at two different salt concentrations

	k_a	k_d	K
	$(\times 10^{-4})$	$(\times 10^{4})$	$(\times 10^{-7})$
	$M^{-1}s^{-1}$	s^{-1}	M^{-1}
0.1 M NaCl	4.5	1200	0.038
0.5 M NaCl	7.5	460	0.16

Note: the target DNA is at 0.35 μM for both NaCl concentrations. The association and dissociation rates and equilibrium constant are obtained by fitting experimental data with the diffusion-reaction model. The fitting parameters were association rate k_a and equilibrium dissociation constant K_D. Dissociation rate $k_d = k_a \cdot K_D$, and Equilibrium constant $K = k_a/k_d$. The diffusion coefficient D, and probe density P_0 are set as constants, and $D = 1.15 \times 10^{-6}$ cm^2/s, and $P_0 = 1.1 \times 10^{12}$ #/cm^2.

3.4 Conclusions

TIRF imaging of the microarray allows in situ measurements of the hybridization kinetics of target DNA molecules with surface oligos. The hybridization kinetics of target DNA with various concentrations to a surface has been measured using TIRF. Langmuir isotherm was used to analyze the equilibrium data and obtain the equilibrium constant and the intensity at final coverage. A diffusion-reaction model that includes the effects of diffusion and solution-phase depletion was used to obtain estimates for surface hybridization rate constants, equilibrium constants, and the surface probe densities. The depletion in solution was estimated from the model data. The model is further used to extract kinetics data at two different ionic strength (0.1M NaCl and 0.5M NaCl). Comparing with the association reaction rate, the dissociation rate is more sensitive to either the length of the oligo sequence or the ionic strength in solution. In Chapters V and VI, I examine DNA melting at surface, which is a process that only involved with the dissociation reaction under the temperature influence.

References

1	Schena, M.; Shalon, D.; Davis, R. W.; Brown, P. O., "Quantitative Monitoring of Gene Expression Patterns with a Complementary DNA Microarray", *Science* **1995**, *270*, 467-470.

2	DeRisi, J. L.; Iyer, V. R.; Brown, P. O., "Exploring the Metabolic and Genetic Control of Gene Expression on a Genomic Scale", *Science* **1997**, *278*, 680-686.

3	Oh, S. J.; Ju, J.; Kim, B. C.; Ko, E.; Hong, B. J.; Park, J.-G.; Park, J. W.; Choi, K. Y., "DNA Microarrays on a Dendron-modified Surface Improve Significantly the Detection of Single Nucleotide Variations in the p53 Gene", *Nucleic Acids Research* **2005**, *33*, e90.

4	Georgiadis, R.; Peterlinz, K. P.; Peterson, A. W., "Quantitative Measurements and Modeling of Kinetics in Nucleic Acid Monolayer Films Using SPR Spectroscopy", *J. Am. Chem. Soc.* **2000**, *122*, 3166-3173.

5	Peterson, A. W.; Heaton, R. J.; Georgiadis, R., "Kinetic Control of Hybridization in Surface Immobilization DNA Monolayer Films", *J. Am. Chem. Soc.* **2000**, *122*, 7837-7838.

6	Peterson, A. W.; Heaton, R. J.; Georgiadis, R. M., "The Effect of Surface Probe Density on DNA Hybridization", *Nucleic Acids Research* **2001**, *29*, 5163-5168.

7	Wolf, L. K.; Fullenkamp, D. E.; Georgiadis, R. M., "Quantitative Angle-Resolved SPR Imaging of DNA-DNA and DNA-Drug Kinetics", *J. Am. Chem. Soc.* **2005**, *127*, 17453-17459.

8	Peterson, A. W.; Wolf, L. K.; Georgiadis, R. M., "Hybridization of Mismatched or Partially Matched DNA at Surfaces", *J. Am. Chem. Soc.* **2002**, *124*, 14601-14607.

9	Thiel, A. J.; Frutos, A. G.; Jordan, C. E.; Corn, R. M.; Smith, L. M., "In Situ Surface Plasmon Resonance Imaging Detection of DNA Hybridization to Oligonucleotide Arrays on Gold Surfaces", *Anal. Chem.* **1997**, *69*, 4948-4956.

10   Nelson, B. P.; Grimsrud, T. E.; Liles, M. R.; Goodman, R. M.; Corn, R. M., "Surface Plasmon Resonance Imaging Measurements of DNA and RNA Hybridization Adsorption onto DNA Microarrays", *Anal. Chem.* **2001**, *73*, 1-7.

11   Tawa, K.; Yao, D.; Knoll, W., "Matching Base-pair Number Dependence of the Kinetics of DNA-DNA Hybridization Studied by Surface Plasmon Fluorescence Spectroscopy", *Biosensors and Bioelectronics* **2005**, *21*, 322-329.

12   Peterlinz, K. A.; Georgiadis, R. M.; Herne, T. M.; Tarlov, M. J., "Observation of Hybridization and Dehybridization of Thiol-Tethered DNA Using Two-Color Surface Plasmon Resonance Spectroscopy", *J. Am. Chem. Soc.* **1997**, *119*, 3401-3402.

13   Glazer, M.; Fidanza, J. A.; McGall, G. H.; Trulson, M. O.; Forman, J. E.; Suseno, A.; Frank, C. W., "Kinetics of Oligonucleotide Hybridization to Photolithographically Patterned DNA Arrays", *Analytical Biochemistry* **2006**, *358*, 225-238.

14   Pappaert, K.; Hummelen, P. V.; Vanderhoeven, J.; Baron, G. V.; Desmet, G., "Diffusion-Reaction Modelling of DNA Hybridization Kinetics on Biochips", *Chemical Engineering Science* **2003**, *58*, 4921-4930.

15   Axelrod, D., "Total Internal Reflection Fluorescence Microscopy", *Biophysical Tools for Biologists* **2008**, *Vol 2: In Vivo Techniques*, 169-221.

16   Lehr, H.-P.; Reimann, M.; Brandenburg, A.; Sulz, G.; Klapproth, H., "Real Time Detection of Nucleic Acid Interactions by Total Internal Reflection Fluorescence", *Anal. Chem.* **2003**, *75*, 2414-2420.

17   Zauderer, E. *Partial Differential Equations of Applied Mathematics*; Third ed.; John Wiley & Sons, Inc.: Hoboken, New Jersey, 2006,

18   Myszka, D. G.; He, X.; Dembo, M.; Morton, T. A.; Goldstein, B., "Extending the Range of Rate Constants Available from BIOCORE: Interpreting Mass Transport-Influenced Binding Data", *Biophysical Journal* **1998**, *75*, 583-594.

19   Broersma, S., "Rotational Diffusion Constant of a Cylindrical Particle", *J. Chem. Phys.* **1960**, *32*, 1626-1631.

20   Broersma, S., "Viscous Force Constant for a Closed Cylinder", *J. Chem. Phys.* **1960**, *32*, 1632-1635.

21   Broersma, S., "Viscous Force and Torque Constants for a Cylinder", *J. Chem. Phys.* **1981**, *74*, 6989-6990.

22   Sorlie, S. S.; Pecora, R., "A Dynamic Light Scattering Study of Four DNA Restriction Fragments", *Macromolecules* **1990**, *23*, 487-497.

23   Nkodo, A. E.; Garnier, J. M.; Tinland, B.; Ren, H.; Desruisseaux, C.; McCormick, L. C.; Drouin, G.; Slater, G. W., "Diffusion Coefficient of DNA Molecules During Free Solution Electrophoresis", *Electrophoresis* **2001**, *22*, 2424-2432.

24   Yu, F.; Yao, D.; Knoll, W., "Oligonucleotide Hybridization Studied by a Surface Plasmon Diffraction Sensor (SPDS)", *Nucleic Acids Research* **2004**, *32*, e75.

25   Zhang, Z.; Knoll, W.; Foerch, R.; Holcomb, R.; Roitman, D., "DNA Hybridization on Plasma-Polymerized Allylamine", *Macromolecules* **2005**, *38*, 1271-1276.

26   Michel, W.; Mai, T.; Naiser, T.; Ott, A., "Optical Study of DNA Surface Hybridization Reveals DNA Surface Density as a Key Parameter for Microarray Hybridization Kinetics", *Biophysical Journal* **2007**, *92*, 999-1004.

27   Wang, S.; Friedman, A. E.; Kool, E. T., "Origins of High Sequence Selectivity: A Stopped-Flow Kinetics Study of DNA/RNA Hybridization by Duplex- and Triplex-Forming Oligonucleotides", *Biochemistry* **1995**, *34*, 9774-9784.

28   Levicky, R.; Horgan, A., "Physicochemical Perspectives on DNA Microarray and Biosensor Technologies", *Trends in Biotechnology* **2005**, *23*, 143-149.

CHAPTER IV

DNA NON-EQUILIBRIUM THERMAL DESORPTION ON A HOMOGENEOUS SURFACE

4.1 Introduction

The preceding chapter was concerned with the real-time detection of the adsorption and desorption of DNA target molecules onto a homogeneous oligonucleotide surface at room temperature. It showed that the dissociation rate is more sensitive to the oligonucleotide sequence than the association rate. This chapter focuses on the thermal desorption kinetics of DNA duplexes on a homogeneous oligonucleotide surface, and specifically looks at the possibility of using thermal desorption curves to discriminate between DNA strands having a single base pair mismatch. Total internal reflection fluorescence is applied as the detection method here, same as in Chapter III.

This section provides an introduction to melting behaviors of DNA probe-target duplexes and their detection methods, both in solution and at surfaces, and the motivation to discriminate single base pair mismatches in otherwise complementary sequences.

4.1.1 DNA melting in solution

DNA melting behaviors have been studied extensively in aqueous solutions for more than 50 years as a way to examine interactions between DNA strands [1-4]. When DNA duplexes in a solution are heated, the double helical structure of a DNA deplex starts to unravel and eventually it will separate into its two parent strands. During this denaturation process, the ultraviolet (UV) absorbance of DNA strands will change. The UV absorbance of DNA is mainly due to its aromatic bases, and it will increase by ~40% upon denaturation as a result of the disruption of interactions among the neighboring bases of DNA [5]. By monitoring the changes in UV absorbance at 260 nm with temperature, a DNA melting curve can be obtained as shown in Figure 4.1. The melting temperature (T_m) is defined as the temperature where half of the base pairs are in a dissociated form and half remain in the double-helical structure. T_m provides a measure of the stability of a DNA double helix, and its value can depend on the DNA sequence itself, and other environmental factors such as solvent, pH, and the types and concentrations of ions in the solvent [5].

Various empirical equations have been developed to calculate the melting temperatures of a DNA duplex from its chain length and the mole fraction of GC pairs in it, the concentration of [Na$^+$] in the solution, and the presence of organic denaturants such as formamide [6]. A couple of representative equations are as follows:

$$T_m = 81.5 + 16.6 \times \log([Na^+]) + 0.41 \times f(GC) - 0.61 \times f(formamide) - \frac{500}{L} \tag{4.1}$$

$$T_m = 81.5 + 16.6 \times \log\left(\frac{[Na^+]}{1 + 0.7[Na^+]}\right) + 0.41 \times f(GC) - \frac{500}{L} - 0.63 \times f(formamide) \tag{4.2}$$

where T_m is the melting temperature in °C, $[Na^+]$ is the sodium ionic concentration in M, $f(GC)$ is the mole fraction of GC pairs in DNA sequence, $f(formamide)$ is the mole fraction of formamide in the solution, and L is the DNA chain length. The above equations illustrate that the melting temperatures depend not only on DNA chains, but also on solution conditions.

Except to the chain length and composition, the sequence of a DNA duplex also affects its melting temperature. Given a set of solution conditions, the stability of a DNA duplex will depend on its base sequence, and primarily depend on the identity of the nearest-neighbor (NN) bases [7]. There are ten different NN stacking interactions in any Watson-Crick DNA duplex structure, and they are AA/TT, AT/TA, TA/AT, CA/GT, GT/CA, CT/GA, GA/CT, CG/GC, GC/CG, and GG/CC [7,8]. Nearest-neighbor (NN) model indicates that the helix-coil transition during a DNA melting process is related to the stacking free energy in the DNA helix structure [7-11]. The thermodynamic parameters of these base pairs under standard salt concentrations (i.e., standard enthalpy change $\Delta H°$ and standard entropy change $\Delta S°$) are reported in the literature [7,8,11] and listed in Table 4.1. The NN model assumes that the standard enthalpy change or the standard entropy change of a DNA sequence will be the summation of the enthalpy or entropy of its NN base pairs in the sequence, with correction terms such as "initiation with terminal GC", "initial with terminal AT", or "symmetry of self-complementary duplexes" [8]. Using the NN base interaction model, T_m of an oligonucleotide to its complement can be calculated as [8]

$$T_m = \frac{\Delta H}{\Delta S + R \bullet \ln C_T} ,$$

(4.3)

where ΔH is the enthalpy change and ΔS is the entropy change for formation of the duplex (both ΔH and ΔS are determined by the DNA sequence using the NN base stacking energies), C_T is the total oligonucleotide strand concentration, and R is the gas constant, 1.987 cal/(K·mol). T_m calculated from eq (4.3) uses 1 M [Na$^+$] as the standard reference buffer, and empirical models have been derived for calculating the melting temperatures of DNA oligomers at other salt concentrations [4]. A representative equation is as follows:

$$\frac{1}{T_m(2)} = \frac{1}{T_m(1)} + (4.29 f(GC) - 3.95) \times 10^{-5} \ln \frac{[Na^+]_2}{[Na^+]_1} + 9.40 \times 10^{-6} (\ln^2 [Na^+]_2 - \ln^2 [Na^+]_1) \qquad (4.4)$$

where $f(GC)$ is the mole fraction of GC base pairs, [Na$^+$]$_1$ and [Na$^+$]$_2$ are two different sodium ion concentrations, and $T_m(1)$ is the melting temperature at [Na$^+$]$_1$, and $T_m(2)$ is the melting temperature at [Na$^+$]$_2$.

The aforementioned models have been applied by many researchers to predict nucleic acid stability in a solution phase. It is noted that experimental observations indicate that DNA melting behaviors in solutions satisfy equilibrium conditions throughout melting transitions [4].
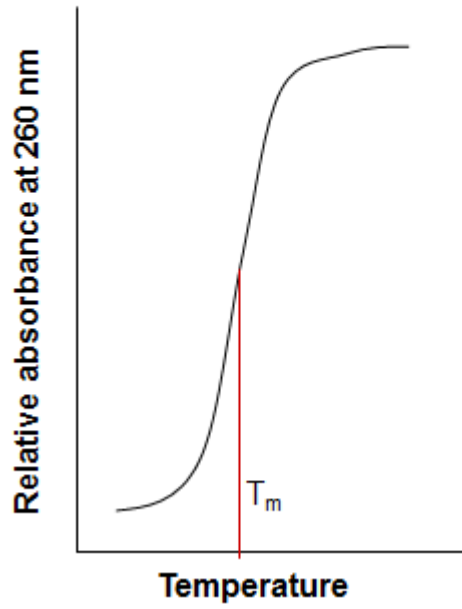
Figure 4.1. Schematic of a DNA melting curve. T_m is the melting temperature where half of the maximum increase in UV absorbance is attained [5].

Table 4.1 Stacking energies for 10 possible dimers in 1 M NaCl [8]

Interactions	ΔH (kcal/mole)	ΔS (cal/mole/K)
AA/TT	-7.9	-22.2
AT/TA	-7.2	-20.4
TA/AT	-7.2	-21.3
CA/GT	-8.5	-22.7
GT/CA	-8.4	-22.4
CT/GA	-7.8	-21.0
GA/CT	-8.2	-22.2
CG/GC	-10.6	-27.2
GC/CG	-9.8	-24.4
GG/CC	-8.0	-19.9
Init. w/term. GC	0.1	-2.8
Init. w/term. AT	2.3	4.1
Symmetry correction	0	-1.4

4.1.2 DNA melting at a surface

In contrast with solution, the melting behaviors of a DNA duplex at a surface are more complex and much less understood. As in solution, when DNA duplexes are heated above their melting temperature, the duplex separates into two single-stranded DNA chains. When this process is performed where one of the strands in the duplex is attached to a surface, the other strand will leave the surface during the melting process. To monitor this process, a variety of detection methods have been used to acquire DNA melting curves at a surface [12-15]. O´Sullivan et al. explored DNA melting behaviors on an electrode surface by differential pulse voltammetry [12]. Georgiadis et al. studied DNA dehybridization on a gold surface using a two-color surface plasmon resonance spectroscopy [13]. Mirkin et al. investigated DNA melting on surfaces by labeling oligonucleotide targets with gold nanoparticles [14]. In these studies, the oligonucleotides (~20-mer) were immobilized onto surfaces by Au-thiol bonding. The Au-thiol bonding is not covalent and such systems may not be stable under a typical melting temperature range between 25 ºC to 80 ºC. An alternative method that can be used to acquire melting curves at a surface is to fluorescently tag target DNA molecules and monitor the fluorescence signal from the surface using a method such as TIRF as the duplexes undergo an increase in temperature. Lehr et al. measured melting curves of a 140-mer single-stranded PCR product that hybridized with two oligonucleotide spots, a 15-mer allele-specific wild-type and a 15-mer allele-specific mutant, on a silane-derivatized glass surface [15]. The authors showed that the melting temperatures of the two spots differed by 10 ºC. This work demonstrated the ability of TIRF to detect the presence of sub-

monolayer amounts of fluorescently-labeled DNA strands at a surface, and that a DNA

melting process could be followed *in situ* by this technique. From this study, it is not

clear how the 140-mer PCR product hybridized with the 15-mer oligonucleotides at the

surface as no details on surface hybridization were given. Further, little quantitative

analysis was provided by the authors on the obtained melting curves.

All the aforementioned indicate that the melting curves at surface were often

obtained under non-equilibrium conditions, although the authors did not mention that.

The measured surface melting temperatures depend on ionic strength in the buffer

solution [13] and probe sequence [15]. These studies [12,13] also showed that the measured

surface melting temperatures were lower than the calculated ones in solution (T_m) using

the prediction models. Except to these studies, a few groups have purposely investigated

the non-equilibrium desorption kinetics of DNA melting at surfaces, and it has been

proposed as an alternative approach to obtain DNA melting curves, with a focus on

discriminating single base mismatches [16-21]. Such non-equilibrium desorption

experiments used either an epifluorescence microscope [16-19,21] or a microarray scanner [20]

to detect the fluorescence signals from the chip surface. These detection methods are not

surface sensitive and high background signals can be included in the experimental data.

In addition, using a microarray scanner required ~35 repeated manual washing and

scanning steps to obtain the melting curves for one sample, and the melting curves were

not acquired in real time [20].

4.1.3 Discrimination of single base mismatch

Single nucleotide polymorphisms (SNPs) are one set of single base-pair mismatches and occur in abundance as a variation in the human DNA sequence [22]. Discovery and genotyping SNPs provides a tool for high resolution genetic analysis with the expectation to understand genetic contribution to diseases and expand clinical abilities in prognosis, diagnosis, and treatment. Commonly used DNA microarrays for such variation analysis [23,24] rely on hybridization specificity and washing stringency to identify the presence of a single mismatched base pair. This method is often limited by the difficulties in finding appropriate experimental conditions that allow for distinguishing between sequences. Such factors include the probe density, as well as the hybridization and washing conditions. For example, the equilibrium hybridization efficiencies between a surface with 25-mer oligonucleotides and three targets -- perfectly matched, one base-pair mismatch and two base-pair mismatch -- were very close and the base pair mismatches are indistinguishable at a probe density of $3 \times 10^{12}/cm^2$, while these mismatches between targets are discerned at a probe density of $1.5 \times 10^{12}/cm^2$ [25].

The purpose of this study was to (1) provide an approach to detect DNA non-equilibrium melting kinetics at a surface *in situ* using a convenient fluorescence method (2) obtain kinetic parameters and apply appropriate mathematical models to describe kinetics of DNA melting at a surface, and (3) quantify differences in the melting temperatures between perfectly matched and one base-pair mismatched sequences, and compare the melting temperatures at a surface with those in solution as obtained by nearest-neighbor model predictions.

4.2 Methods and materials

Slide preparation. Microscopic slides were cleaned in piranha solution (7:3(v/v), concentrated H_2SO_4 : 30% H_2O_2. Caution: "piranha" solution reacts violently with organic material and should be used with great care.) for 30 min, followed by rinsing with copious quantities of DI water and drying under a N_2 stream. The slides were then immersed into a 1 wt.% N-(3-triethoxysilylpropyl)-4-hydroxy-butyramide (Gelest, Morrisville, PA) solution in 95% ethanol for 16 hours to produce a hydroxyl silane surface. The slides were removed from the silane solution, rinsed sequentially with ethanol and water, and then blown dry with N_2. Then the slides were heated in an oven at ~110 °C for 30 min to anneal the films. Surface oligonucleotides were synthesized from the hydroxyl groups using phosphoramidite chemistry (see Chapter II).

Oligonucleotide sequences. The sequence of the perfectly matched (PM) surface oligo was 3'-TTTTTGCCTCCACGATTCTA-5'. The sequence of the one mismatched (1MM) surface oligos was 3'-TTTTTGCCTCCA*T*GATTCTA-5' (Italic and bold base T at position 8 from the 5'-terminus was designed as a single mismatch with the target). For both sequences, the 3' ends were attached to the surface. The five T bases at 3'-terminus were used as spacers. The sequence of the Cy3 fluorescently-tagged target DNA was 5'-CGGAGGTGCTAAGAT Cy3 -3' (Integrated DNA Technologies, Coralville, IA.). There was one base mismatch between surface oligos 1MM and target DNA, i.e., the G-T mismatch in the center at base position 8 from the 5'-terminus.

94

Surface hybridization. Hybridization to the synthesized surface oligos was performed with 40 μL of 2 μM target DNA solution. The target was pipetted onto the probe region and covered by a 22×22 mm glass coverslip (Fisher Scientific). The slide was transferred into a hybridization chamber (Corning Inc., Corning, NY) and the humidification wells of the chamber were filled with 1×TE buffer (10mM Tris buffer and 1mM EDTA, pH 8.0), and the chamber was kept at room temperature for 16 hours to allow for hybridization. Afterward the surface was washed at room temperature with 1×SSC buffer. The surface was scanned with a GenePix 4000B laser scanner (Molecular Devices, Sunnyvale, CA) to check surface uniformity and estimate surface density.

TIRF instrument. A TIRF system was constructed for measurements of DNA non-equilibrium desorption kinetics at a surface (Figure 4.2). The light source was a diode-pumped solid-state (DPSS) laser that emitted light at a wavelength of 532 nm and an output power at 30 mW (Laserglow Technologies, Toronto, Canada). The diameter of the produced laser spot was about 1~2 mm. The laser beam was expanded by passing the light through a plano-concave lens (material N-BK7, standard broadband AR coating for wavelength 350~700 nm, dia = 12.7 mm, f = -25.0 mm, Thorlabs, Newton, NJ) and a plano-convex lens (material N-BK7, standard broadband AR coating for wavelength 350~700 nm, dia = 25.4 mm, f = 250.0 mm, Thorlabs, Newton, NJ), consecutively. A normally closed beam shutter (Thorlabs, Newton, NJ) was placed between the laser and the concave lens to allow sub-millisecond shutter operations using a shutter controller (Thorlabs, Newton, NJ). The expanded laser beam size was further adjusted using an Iris Diaphragm with a maximum aperture size of 20.0 mm (Thorlabs, Newton, NJ), and then

passed through a dove prism and totally internal reflected at the interface (see Figure 4.2(A)). The DNA chip surface was attached to the prism surface by using a couple of drops of index-matching oil (Cargille Laboratories, Cedar Grove, NJ). The emitted fluorescent light above the chip surface passed through an emission filter (Omega Optical, Brattleboro, VT), and a macro video lens (Optem International), and was detected by a Retiga 1300 CCD camera (QImaging, Surrey, BC, Canada). The camera and the shutter controller were connected to a PC, and controlled using custom-written MATLAB code.

Surface melting curves (desorption kinetics). In the melting experiments, a customized flow cell (volume ~2 mL) was attached on top of the chip surface, as illustrated in Figure 4.2(B). The DNA chip surface and the flow cell were mounted on top of the prism of the TIRF system. Two liters of 0.5 M NaCl (aq.) buffer solution were placed in a Pyrex® glass beaker and the beaker was placed inside a VWR Signature refrigerated/heating circulating bath with a programmable temperature controller. The buffer solution was agitated, heated simultaneously with a linear temperature rise, and circulated through the flow cell at ~ 34 mL/min using a peristaltic pump (Cole-Parmer Instrument, Vernon Hills, Illinois). Before the temperature ramp, the buffer solution was circulating through the flow cell for ~5 minutes at ~25 °C. At the same time, the QImaging Retiga 1300 CCD camera (Surrey, BC, Canada) camera was started to acquire images from the surface every 20 s. The time series of surface fluorescent images were recorded using the camera that was controlled in MATLAB environment, and the temperatures at both the inlet and outlet of the flow cell were also recorded. The data were acquired and analyzed using a custom-written MATLAB code.

Temperature measurements. Two T-type (Copper-Constantan) thermocouples (Omega Engineering, Inc., Stamford, CT) were inserted at the inlet and outlet of the flow cell to measure the buffer solution temperature at these two locations. A portable USB-based DAQ card for thermocouples (National Instruments, Austin, TX) was used to acquire the temperature data using a custom-written MATLAB code. The non-equilibrium melting curves for both PM and 1MM surface oligos were determined between 25 °C and 60 °C with a temperature ramp rate at 0.85 °C/min. Figure 4.3 shows a typical temperature ramp profiles from both the inlet and outlet of the flow cell. This figure shows temperature variation across the flow cell to be < 0.2 °C. It also shows that the outlet temperature was more stable than the inlet one, as the latter was affected by the movement of the peristaltic pump. The outlet temperature was thus used as the solution temperature in the cell.

Emission efficiency of fluorescent dye Cy3 with temperature. Cyanine dye Cy3 is a commonly used fluorescent dye in DNA microarrays. Liu *et al.* have reported that the fluorescence from Cy3 is affected by solution temperature [26]. The data for Cy3 emission efficiency with respect to temperature changes in a 0.5 M NaCl aqueous solution from literature [26] were extracted and fitted by a polynomial curve, as shown in Figure 4.4. A fluorescent dye correction coefficient $f(T)$, at each temperature T, was calculated using the polynomial curve, and normalized using $f_{norm}(T) = f(T)/f(T_0)$, where $f_{norm}(T)$ is the normalized dye correction coefficient at temperature T, and $f(T)$ and $f(T_0)$ are the calculated dye correction coefficients using the polynomial fitting curve at temperatures T and T_0, respectively.

Data analysis. The size of the selected region of interest (ROI) for each image was 10×10 pixels, and each pixel had a surface area of 400 μm^2 (the surface area of the ROI is close to that of an arrayed spot). The background-subtracted mean intensity of the ROI was first normalized using the equation $I_{norm}(T) = I(T)/I(T_0)$, where $I_{norm}(T)$ is the normalized intensity of the ROI at temperature T, $I(T)$ is the background-subtracted intensity at temperature T, and $I(T_0)$ is the background-subtracted intensity at initial temperature T_0. The normalized fluorescent intensity with dye correction was obtained using the following equation, $\theta(T) = I_{norm,dyecorrection}(T) = I_{norm}(T)/f_{norm}(T)$.

To determine the Redhead peak temperature, the desorption rate ($-d\theta/dt$) at each temperature was calculated from the slope of the desorption curve of surface coverage θ with respect to time t, by linearly fitting eleven data points composing the data point at that time, five data points before and five data points after the given temperature. The desorption rate constants, k_d's, were calculated using $k_d = (-d\theta/dt)/\theta$ at each temperature, assuming first-order kinetics.
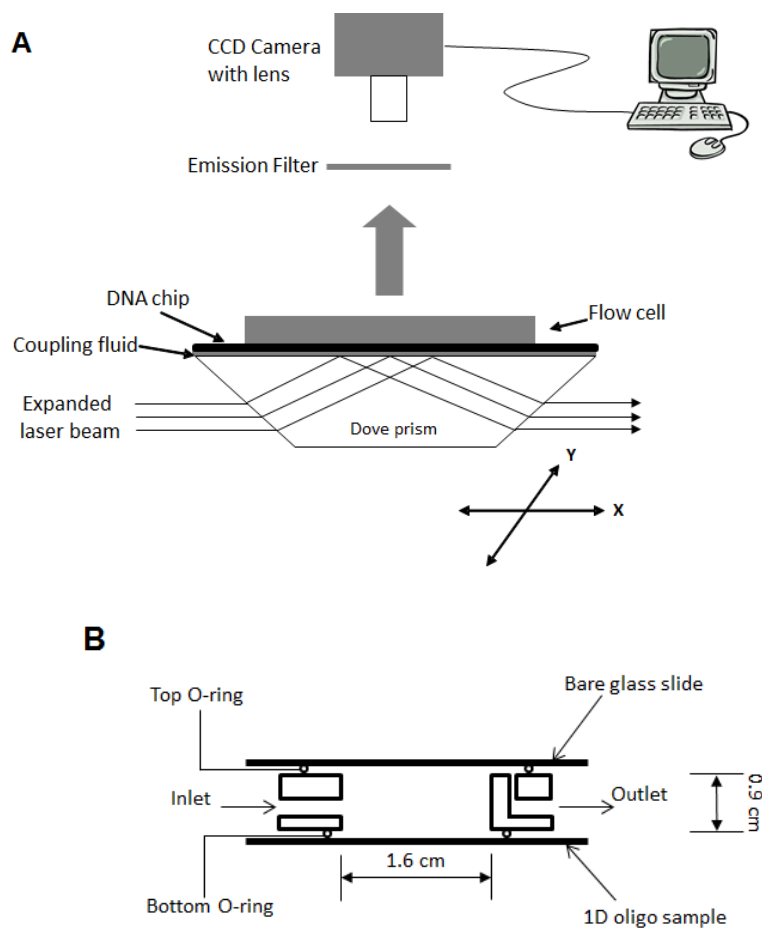
Figure 4.2. Schematic illustrations of (A) the experimental TIRF system for measuring non-equilibrium desorption kinetics at surface, and (B) a cross-section of the custom-made flow cell.
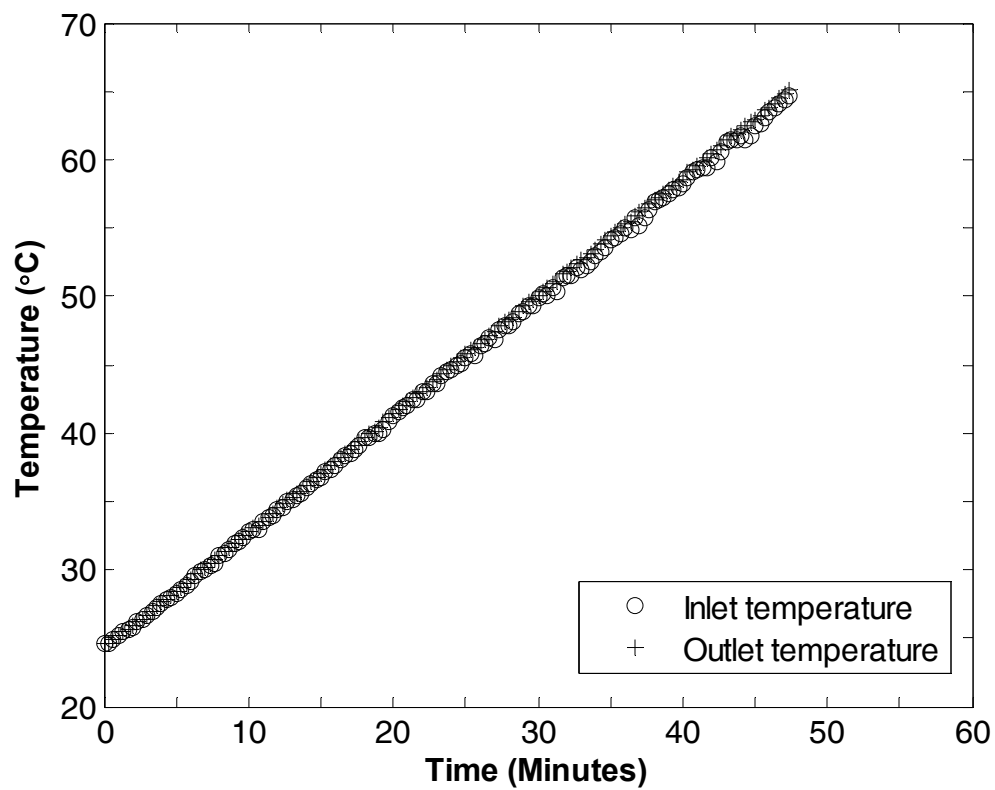
Figure 4.3. Linear temperature sweep profiles as recorded at both the inlet and outlet of the flow cell.
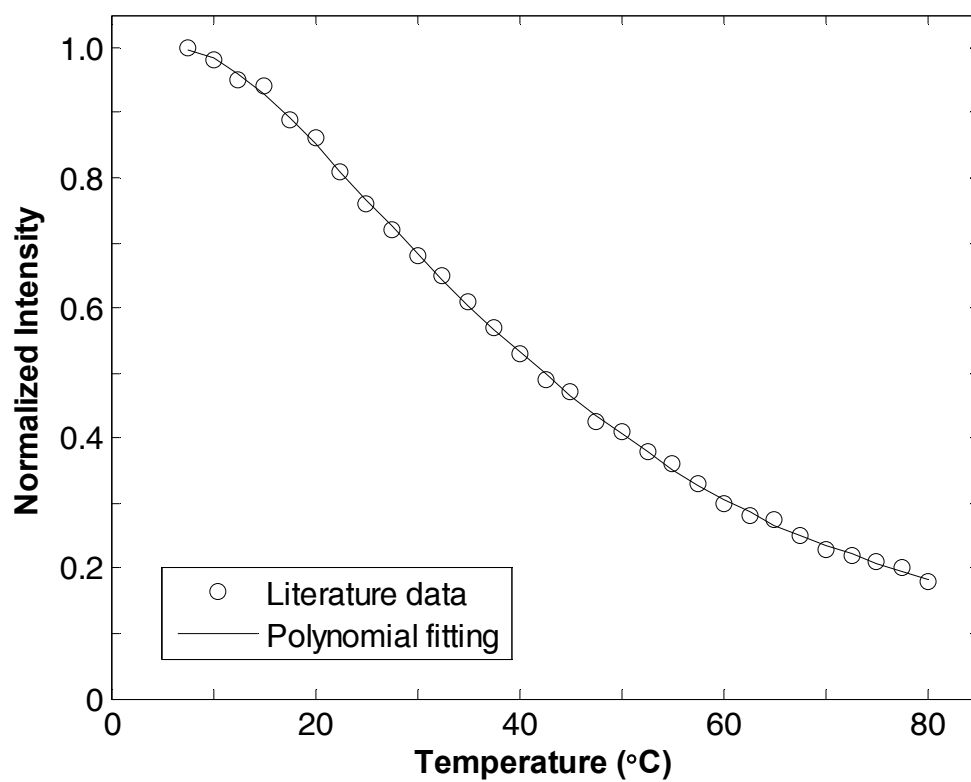
Figure 4.4. Emission coefficiency of Cy3 with respect to temperature on a gel-based microchip in 0.5 M NaCl. The experimental data were taken from Ref [26]. The data are fitted by a polynomial curve.

4.3 Results and discussion

Discrimination of one base pair mismatch by half temperatures ($T_{0.5}$'s). As shown in Figure 4.5 is the comparison of two separate non-equilibrium desorption curves. One curve was obtained from the melting of a 15-mer perfectly matched (PM) sequence, and the other was the melting profile from a 15-mer containing one G/T mismatch (1MM) in the middle of the sequence. Both the melting curves have a sigmoid shape, and they start to separate from each other when the solution temperature is greater than 38 °C. One characteristic temperature that often used to describe the desorption process is the half temperature ($T_{0.5}$), which is defined as the temperature at which 50% of the target molecules are remained at the surface [16]. From Figure 4.5, the half temperature for a 15-mer PM sequence ($T_{0.5,PM}$) is determined as 51.7 °C, and for the 1MM sequence $T_{0.5,1MM}$ ≈ 45.7 °C. The difference of the two half temperatures are 6.0 °C for a G/T mismatch.
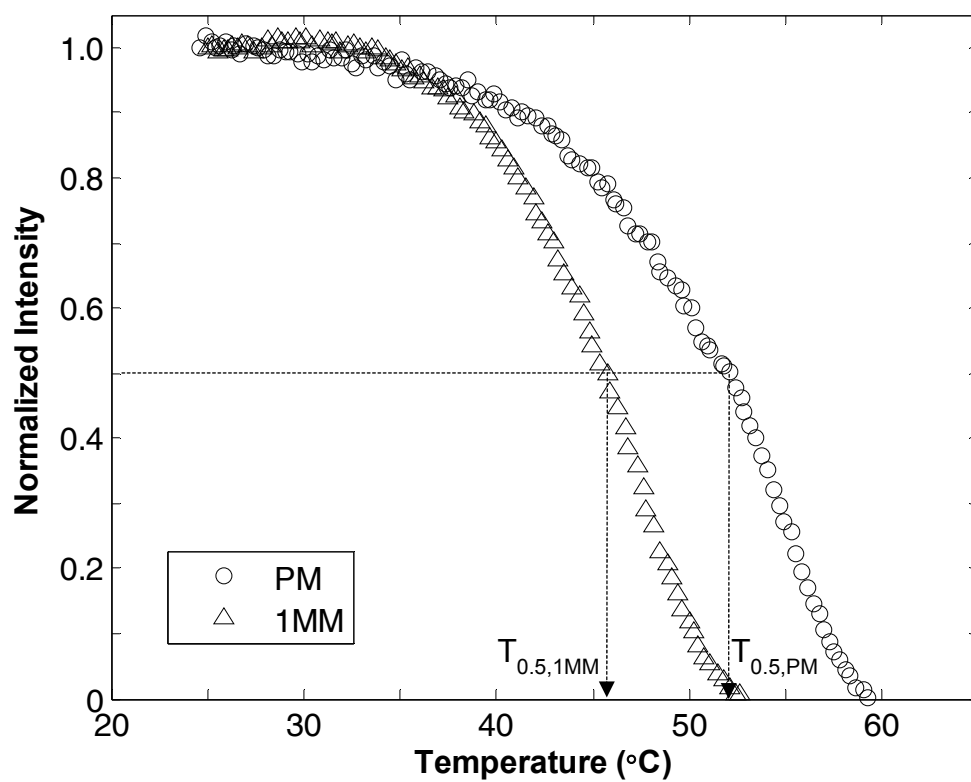
Figure 4.5. Non-equilibrium desorption curves of 15-mer perfectly matched (PM) and one G/T mismatched (1MM) probe-target duplexes. The half temperatures, $T_{0.5,PM}$ and $T_{0.5,1MM}$ are determined as the temperatures at which the normalized fluorescent intensity drops to 0.5.

Discrimination of one base pair mismatch by peak temperatures (T_p's). The

desorption rates as a function of buffer temperature was obtained and shown in Figure 4.6

for the 15-mer perfectly matched and the one G/T mismatched (1MM) sequences. The

noisy data between 25 °C and 35 °C were not included. Each spectrum shows a

maximum desorption rate, at which the temperature is defined as the peak temperature T_p.

From Figure 4.6, we have the peak temperature for PM sequence $T_{p,PM} \approx$ 54.9 °C, for

1MM sequence $T_{p,1MM} \approx$ 47.3 °C, and the difference of the two peak temperatures are

7.6 °C. Each desorption rate curve is asymmetric about the maximum at T_p. Redhead's

analysis indicated that the shape of the first-order desorption curve is asymmetric about

the maximum at T_p, while that for a second-order case is symmetric [27]. Eq (4.11) in the

appendix shows that given the peak temperature, the activation energy E_a can be

calculated if a value of the pre-exponential factor A_0 is assumed. For thermal desorption

of gaseous adsorbates from solid surfaces, the pre-exponential value is often assumed as

10^{13}/s. However, a survey of numerous literature results on such systems showed that the

pre-exponential factor is dependent on the surface coverage by more than a factor of 10^3,

in some cases even up to 10^{11} [28]. The behaviors of thermal desorption of DNA molecules

in a solution phase is not well understood. To determine an appropriate value for the pre-

exponential factor, Arrhenius plot is used next to obtain estimated values for the kinetic

parameters such as the pre-exponential factor and the activation energy.
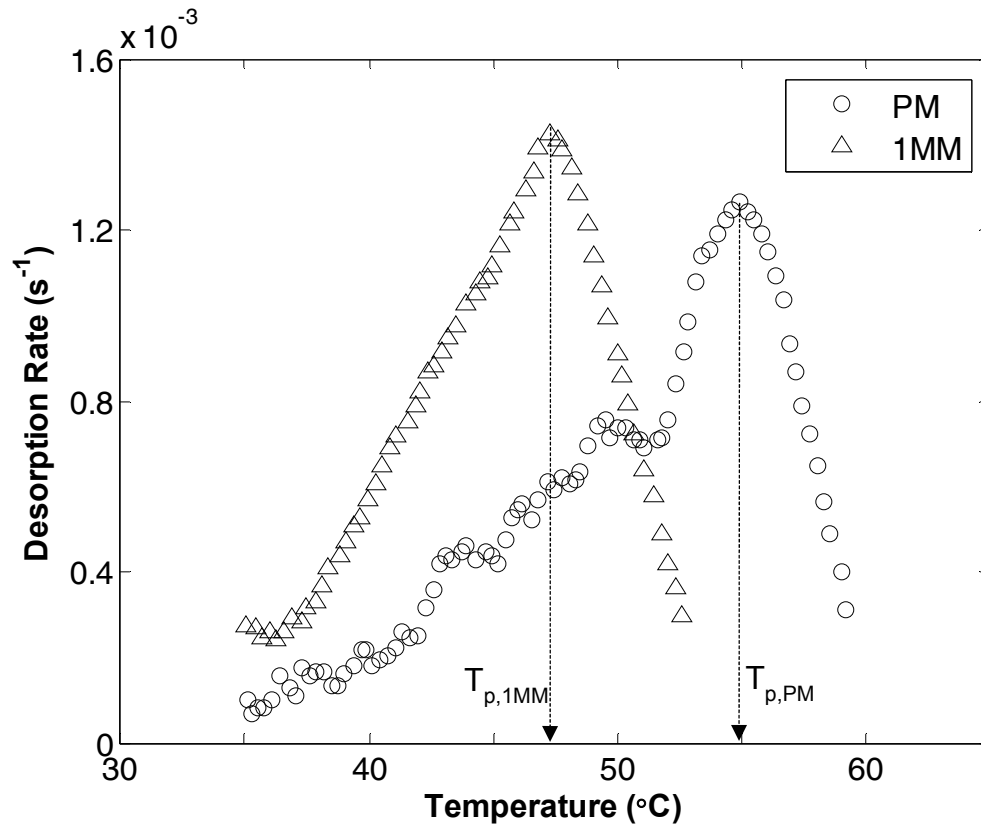
Figure 4.6. Desorption rates of 15-mer perfectly matched (PM) and one G/T mismatched (1MM) probe-target duplexes. The peak temperatures, $T_{p,PM}$ and $T_{p,1MM}$ are determined as the temperatures at which the desorption rate reaches a maximum.

Arrhenius plot. The desorption rate constants (k_d's) were plotted against the

temperature, as shown in Figure 4.7(A). The noisy data between 25 °C and 35 °C, and

those at a small surface coverage less than 0.1 were not included. The Arrhenius plot of

$\ln(k_d)$ against 1/T for both PM and 1MM assuming first-order kinetics are shown in

Figure 4.7(B). Theoretically the Arrhenius plot gives averages of the pre-exponential

factor and activation energy from the intercept and slope. The plot for 1MM shows the

linearity across the investigated temperature range. However, for PM it does not show a

singular linearity across the whole temperature range (35 °C to 57 °C). Instead it has two

different slopes: one is between 35 °C and 52 °C (the surface coverage changes from 0.96

to 0.5), and the other is between 52 °C and 57 °C (the surface coverage changes from 0.5

to 0.1).

The difference of the slopes for the PM sequence indicates that the activation

energy probably changes during the desorption process. Thermal desorption of gaseous

molecules from solid surface is often involved with simple monatomic or diatomic

adsorbates [28]. Comparing to these adsorbates, a 15-mer target molecule has a very

different and probably much more complicated binding state to the surface as each AT

base pair have two hydrogen bonds and each GC base pair has three hydrogen bonds.

The desorption of perfectly matched DNA duplexes at surface is like an unzipping

process. Initially at the room temperature, the surface coverage is at one, and the targets

and probes are perfectly matched with each other, assuming activation energy of E_a.

When the solution temperature is reached to the half temperature, i.e. at a surface

coverage of 0.5, half of the targets have left the surface and half of them remain on

surface. However, those targets remained at surface may not be at a perfect matched

condition with probes and the hydrogen bonds between a few base pairs may have been loosen up, as illustrated in Figure 4.8, and thus the activation energy between the probes and targets is lower than E_a. For such an unzipping/desorption process, the activation energy between probes and targets changes over time/temperature. This unzipping process is cooperative and the collapse of one part of the probe/target duplex structure destabilizes the remainder [5]. The half temperature is a transition point where the cooperative dissociation effect becomes more evident afterwards, as indicated by the PM desorption curve that does not have a smooth transition before and after the half temperature, and it is actually more evident to see the transition point from the rate constant plot in Figure 4.7(A), showing that the desorption rate has been "geared" to a different and faster mode. Comparing to PM, the desorption curve and rate constant plot for 1MM sequence are smooth and does not have such a transition point.

Using the intercepts of the fitting lines in Figure 4.7(B), the determined pre-exponential factor for 1MM are $A_0(1\text{MM}) \approx 2 \times 10^{31}$/s, and for PM, $A_0(\text{PM}, 0.5 < \theta < 0.96) \approx 2 \times 10^{20}$/s, and $A_0(\text{PM}, 0.1 < \theta < 0.5) \approx 8 \times 10^{46}$/s. The pre-exponential factors for 1MM and for PM at lower surface coverage is much higher than reported values in literature between 10^6/s to $10^{19.5}$/s [28], and probably due to the unzipping dissociation and cooperative effect of melting as aforementioned. Another reason is that the flowing buffer solution may also contribute to the higher-than-expected desorption rates. Above analysis raises the doubt of the validity of using the Arrhenius plot to accurately determine the kinetics parameters. Instead the pre-exponential factor is guessed to calculate the activation energy and the melting curves using Redhead's equations as discussed next.

A
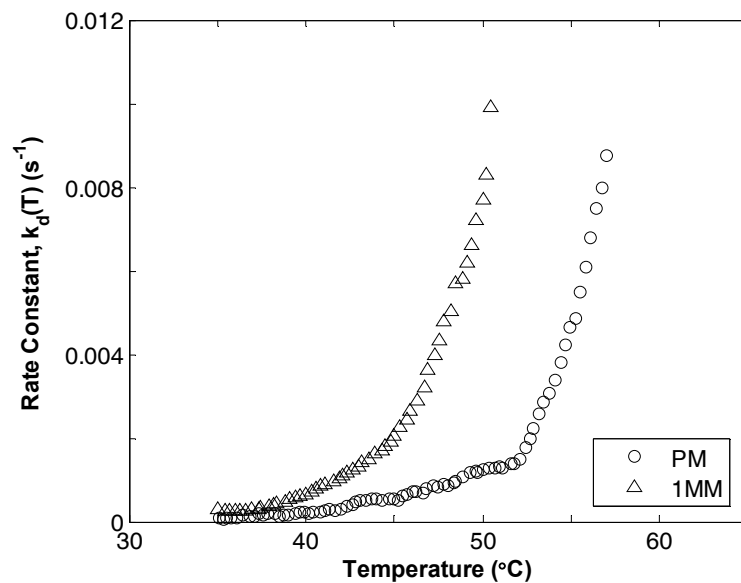
B
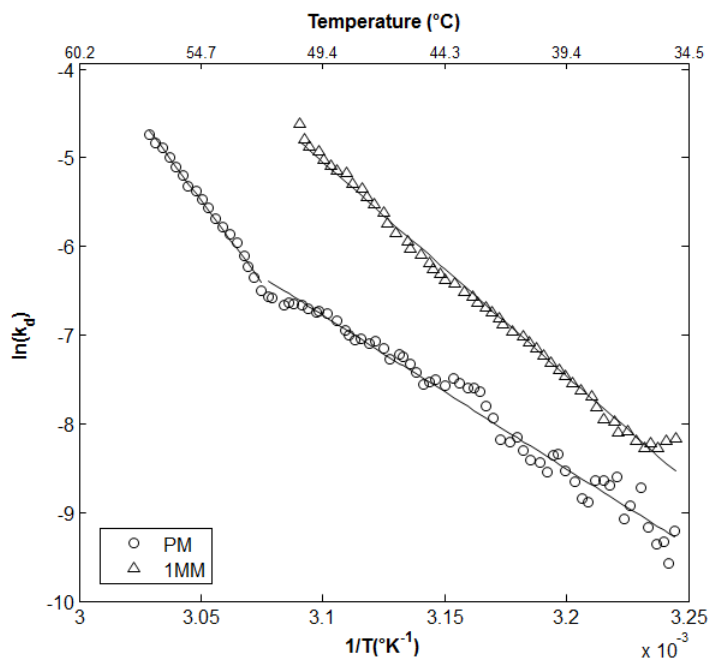
Figure 4.7. (A) Desorption rate constants (k_d's) of 15-mer perfectly matched (PM) and one G/T mismatched (1MM) probe-target duplexes, and (B) the Arrhenius plot for both sequences, and the lines are linear fittings to the selected data points.
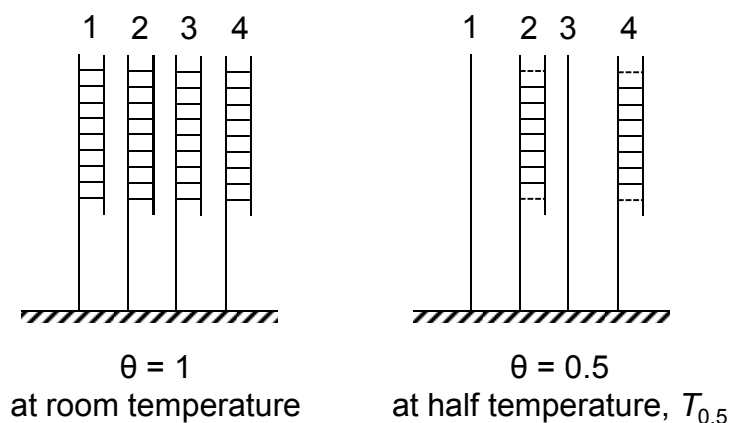
Figure 4.8. Schematic illustrations of the hydrogen bonding between probe-target duplexes at surface coverage $\theta = 1$ and $\theta = 0.5$. At $\theta = 1$ (at room temperature), probes 1 to 4 are perfectly matched with the complementary targets. At $\theta = 0.5$ (at half temperature $T_{0.5}$) targets with probes 1 and 3 has left the surface, and targets with probes 2 and 4 are still bound with the probes but a few base pairs has loosen their hydrogen bonding with probes, shown as the dashed lines.

Calculated melting curves. If we assume the pre-exponential factor $A_0 = 10^{13}$/s, same as Redhead's choice in the Ref. [27], and use eq (4.11) in the appendix, the activation energy for the perfectly matched sequence PM is $E_a(\text{PM}) \approx 23.7$ kcal/mole ($T_{p,\text{PM}} = 54.9\ ^\circ$C), and the activation energy for one G/T mismatched sequence 1MM is $E_a(\text{1MM}) \approx 23.1$ kcal/mole ($T_{p,\text{1MM}} = 47.3\ ^\circ$C). The difference of the activation energy between PM and 1MM is 0.6 kcal/mole. The calculated melting curves using eq (4.16) in the appendix for both PM and 1MM using the above kinetics parameters are shown in Figure 4.9, and it turns out that the calculated curves do not fit the experimental data well.

To better fit the experimental data, I assume $A_0 = 10^{26}$/s. Similarly, using eq (4.11), we have $E_a(\text{PM}) \approx 42.6$ kcal/mole ($T_{p,\text{PM}} = 54.9\ ^\circ$C) and $E_a(\text{1MM}) \approx 41.8$ kcal/mole. The difference of the activation energy between PM and 1MM is 0.8 kcal/mole. Shown in Figure 4.10 are the calculated melting curves using eq (4.16) for both PM and 1MM using the new set of kinetics parameters. It shows that higher pre-exponential factors and higher activation energies fit the experimental data better. Although the pre-exponential factor has changed by over ten orders of magnitude, the difference of the activation energy between PM and 1MM does not change much, indicating that the choice of the pre-exponential factor is not very critical to estimate the difference of the activation energy between PM and 1MM sequences.
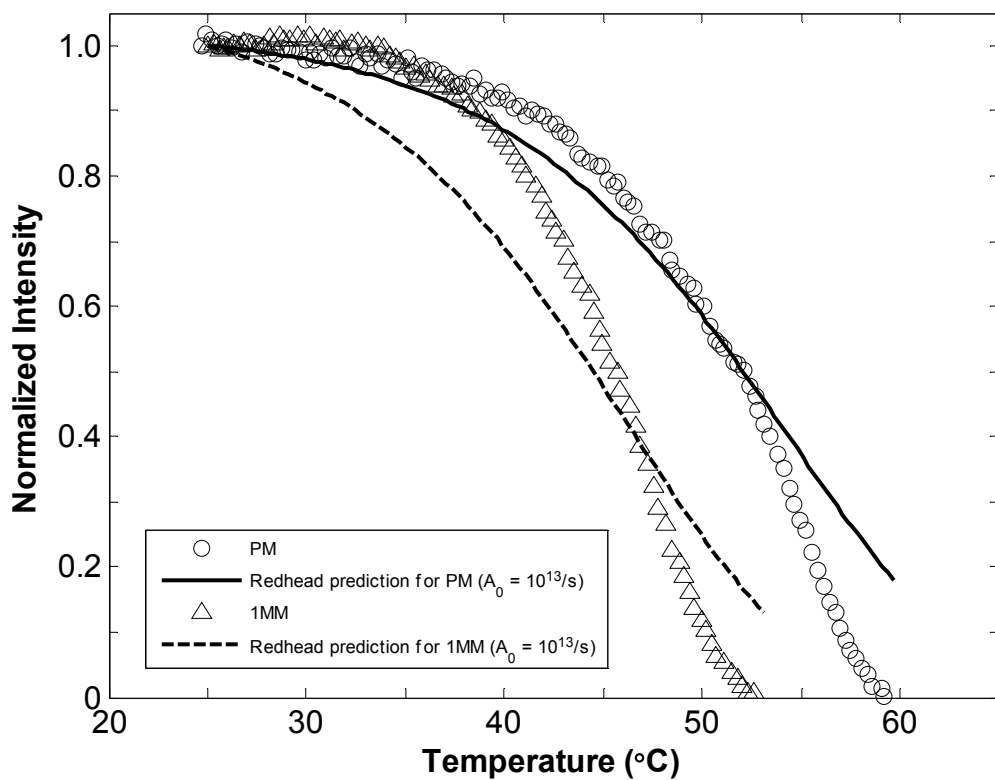
Figure 4.9. The experimental desorption curves and the calculated ones using Redhead equations assuming a pre-exponential factor of 10^{13}/s.
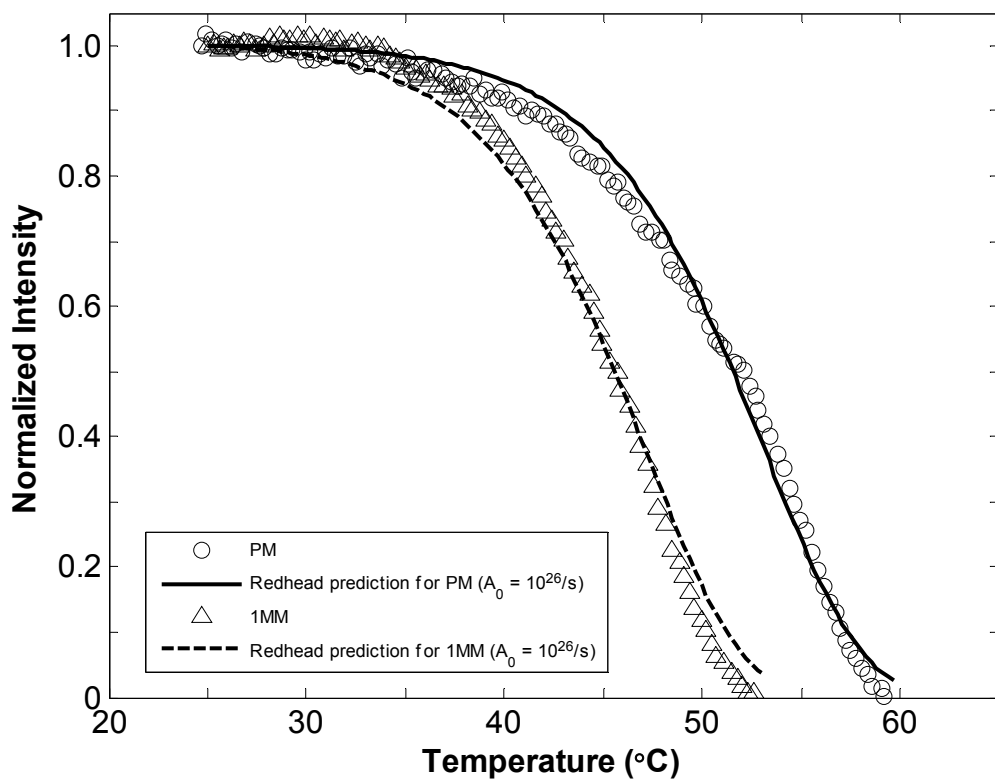
Figure 4.10. The experimental desorption curves and the calculated ones using Redhead equations assuming a pre-exponential factor of 10^{26}/s.

Nearest-Neighbor (NN) model. NN model has been used extensively to provide prediction of DNA melting in solution phase [7,8,11]. As shown in Figure 4.11, the thermodynamic parameters of the perfectly matched trimer pair TGC/ACG were calculated using the NN model, and compared with those of the one G/T mismatched trimer pair T*G*C/A*T*G (italic bases are mismatched). The G/T mismatch contributes to the difference of the change of enthalpy ($\Delta H°$) and the change of entropy ($\Delta S°$). The calculated $\Delta H°$ and $\Delta S°$ for the whole 15-mer sequences are shown in Table 4.2, as well as the melting temperature T_m. The calculated melting temperature in the solution phase using thermodynamic equations is compared with the half temperature and peak temperature determined from the non-equilibrium desorption curves from this study. It shows that both the half temperature and the peak temperature can be used to discriminate a single base pair mismatch, and peak temperature probably gives better resolution than the half temperature, although both temperatures from surface are smaller than T_m from the NN model prediction.

```
Target      5'   C   G   G   A   G   G ┆ T   G   C ┆ T   A   A   G   A   T   3'
Probe PM    3'   G   C   C   T   C   C ┆ A   C   G ┆ A   T   T   C   T   A   5'

                         ΔH° = -18.3 ± 1.0 kcal/mole
                         ΔS° = -47.1 ± 4.0 cal/K·mole




Target      5'   C   G   G   A   G   G ┆ T   G   C ┆ T   A   A   G   A   T   3'
Probe 1MM   3'   G   C   C   T   C   C ┆ A   T   G ┆ A   T   T   C   T   A   5'

                         ΔH° = -4.5 ± 1.0 kcal/mole
                         ΔS° = -14.1 ± 3.4 cal/K·mole
```

Figure 4.11. Comparison of the thermodynamic parameters (standard change of enthalpy ΔH° and standard change of entropy ΔS° in 1 M NaCl) for trimmer pairs TGC/ACG and T*GC*/A*T*G (Italic bases are mismatched). The G/T mismatch contributes to the changes of the thermodynamic parameters. For PM, the parameters are calculated using nearest-neighbor model [8], and for 1MM, the parameters are obtained from a reference paper [29].

Table 4.2 Comparison of temperatures and energies between DNA melting at surface and DNA melting in solution predicted by NN model for the 15-mer perfectly matched (PM) and one G/T mismatched sequences

	This study (at surface)[a]			Nearest-neighbor theory (solution phase)[b]		
	$T_{0.5}$ (°C)	T_p (°C)	E_a (kcal/mole)	T_m (°C)	$\Delta H°$ (kcal/mole)	$\Delta S°$ (cal/K·mole)
PM	51.7	54.9	23.7	54.5	-113.0	-306.5
1MM	45.7	47.3	23.1	45.1	-99.2	-273.5
PM - 1MM	6.0	7.6	0.6	9.4	-13.8	-33

Note: (a) the error of measurement for $T_{0.5}$ and T_p is ± 0.3 °C. The activation energy E_a is given by assuming the pre-exponential factor of 10^{13}/s. (b) T_m was calculated by assuming the total oligonucleotide strand concentration $C_T = 0.01$ µM in eq (4.3), and then adjusted to 0.5 M NaCl using eq (4.4). $\Delta H°$ and $\Delta S°$ are obtained in 1 M NaCl.

4.4 Conclusions

Non-equilibrium desorption melting curves of DNA probe-target duplexes at surface were obtained *in situ* using TIRF. Single base pair mismatch (a G/T mismatch for this study) was discriminated from the melting curves. Half temperature ($T_{0.5}$) and peak temperature (T_p) are two characteristic temperatures that can be used to quantify the melting behavior between a perfectly matched and a single base pair mismatched sequences. Arrhenius plot shows that the perfectly matched sequence has two different slopes before and after the half temperature, while one base mismatched sequence shows one slope. The Arrhenius plot indicates that DNA melting at surface is like an unzipping process. Redhead theory has been used to simulate the melting curves and calculate the activation energies for both PM and 1MM sequences. The discrimination ability of single base pair mismatch at surface has been compared with DNA melting behaviors as predicted by nearest-neighbor model, which shows that surface non-equilibrium desorption curves have similar resolution as equilibrium melting curves in solution.

APPENDIX: Non-equilibrium desorption kinetics

DNA non-equilibrium desorption kinetics is analogous to the kinetics of

temperature programmed desorption (TPD) of chemisorbed gases from the metal surface,

because in both cases the desorption of molecules from surfaces is due to the temperature

ramp. The differences between these two systems are that the DNA desorption is

performed in a liquid solution while the gaseous desorption is often in vacuum. Redhead

has developed analytical solutions to evaluate TPD of gases from metal surfaces [27]. This

appendix reviews the formulation and solution of Redhead theory which applies to

analyze DNA thermal melting at surface in the text.

For the desorption of an adsorbed species from a surface, the rate of desorption

can be written as

$$r_d = -\frac{d\theta}{dt} = k_d \theta^n \, , \tag{4.5}$$

where r_d is the rate of desorption, t is the time, k_d is the desorption rate constant, θ is the

surface coverage of adsorbed species, θ is between 0 and 1, as 1 represents that all the

surface probes are bound with their complementary strands. In eq (4.5), k_d is a function

of reaction temperature, and n is the order of the desorption reaction. Based on the

Arrhenius equation, the temperature dependence for rate constant k_d can be written as

$$k_d = A_0 \exp\left(-\frac{E_a}{RT}\right)$$

$$= A_0 \exp\left(-\frac{E_a}{R(T_0 + a \cdot t)}\right), \tag{4.6}$$

where A_0 is a pre-exponential factor of desorption, E_a is the activation energy of

desorption, T is the reaction temperature (here we consider a linear change of temperature

with time, $T = T_0 + a \cdot t$), T_0 is the initial temperature before the temperature sweep, a is the temperature sweep rate, t is the sweep time, and R is the molar gas constant, 8.314 J K^{-1} mole^{-1}.

By replacing k_d in eq (4.5) with the expression in the eq (4.6), the desorption rate for a first-order reaction ($n = 1$) becomes

$$\frac{d\theta}{dt} = -A_0 \exp\left(-\frac{E_a}{RT}\right)\theta .$$

(4.7)

For a linear temperature ramp given as $T = T_0 + a \cdot t$, we can make use of the expression that $dT = a\,dt$. Substitution of dt by dT/a in eq (4.7) yields

$$\frac{d\theta}{dT} = -\frac{A_0}{a} \exp\left(-\frac{E_a}{RT}\right)\theta .$$

(4.8)

The second derivative of θ with respect to temperature T is

$$\frac{d^2\theta}{dT^2} = -\frac{A_0}{a} \exp\left(-\frac{E_a}{RT}\right)\frac{d\theta}{dT} - \frac{A_0}{a} \exp\left(-\frac{E_a}{RT}\right)\theta\frac{E_a}{RT^2} .$$

(4.9)

At the maximum desorption rate, we have $\dfrac{d^2\theta}{dT^2} = 0$, thus eq (4.9) becomes

$$-\frac{A_0}{a} \exp\left(-\frac{E_a}{RT_p}\right)\frac{d\theta}{dT}\bigg|_{T=T_p} - \frac{A_0}{a} \exp\left(-\frac{E_a}{RT_p}\right)\theta_{T=T_p}\frac{E_a}{RT_p^2} = 0 ,$$

(4.10)

where T_p is the Redhead peak temperature at which the maximum desorption rate occurs. By rearrangements and using eq (4.8), we obtain

$$\frac{E_a}{RT_p^2} = -\frac{1}{\theta}\frac{d\theta}{dT}\bigg|_{T=T_p} = \frac{A_0}{a} \exp\left(-\frac{E_a}{RT_p}\right) .$$

(4.11)

Eq (4.11) is a Redhead equation that relates peak temperature T_p to the activation energy E_a, pre-exponential factor A_0, and the sweep rate a, and T_p is independent of surface coverage for first-order reactions [27].

By rearranging eq (4.8), and integrating both sides of the equation, we obtain

$$\int_{\theta_0}^{\theta} \frac{d\theta}{\theta} = -\frac{A_0}{a} \int_{T_0}^{T} \exp\left(-\frac{E_a}{RT}\right) dT . \tag{4.12}$$

Here we assume that $\theta = \theta_0$ at $T = T_0$, and θ_0 is the initial surface coverage. Using integrating by parts, eq (4.12) becomes

$$\ln\frac{\theta}{\theta_0} = -\frac{A_0}{a}\left(\left(T\exp\left(-\frac{E_a}{RT}\right)\right)\Big|_{T_0}^{T} - \int_{T_0}^{T} T\exp\left(-\frac{E_a}{RT}\right) d\left(-\frac{E_a}{RT}\right)\right)$$

$$= -\frac{A_0}{a}\left(T\exp\left(-\frac{E_a}{RT}\right) - T_0\exp\left(-\frac{E_a}{RT_0}\right) + \frac{E_a}{R}\int_{T_0}^{T} \frac{\exp\left(-\frac{E_a}{RT}\right)}{-\frac{E_a}{RT}} d\left(-\frac{E_a}{RT}\right)\right)$$

$$= -\frac{A_0}{a}\left(T\exp\left(-\frac{E_a}{RT}\right) - T_0\exp\left(-\frac{E_a}{RT_0}\right) + \frac{E_a}{R}\int_{-\frac{E_a}{RT_0}}^{-\frac{E_a}{RT}} \frac{\exp(u)}{u} du\right), \tag{4.13}$$

where $u = -\dfrac{E_a}{RT}$.

Using integration by parts repeatedly, we can obtain the following identity [27]

$$\int_{-\infty}^{x} \frac{e^y}{y} dy = \int_{-\infty}^{x} \frac{1}{y} de^y$$

$$= \frac{1}{y} e^y \Big|_{-\infty}^{x} - \int_{-\infty}^{x} e^y d\frac{1}{y}$$

$$= \frac{e^x}{x} + \int_{-\infty}^{x} \frac{e^y}{y^2} dy$$

$$= \frac{e^x}{x} + \int_{-\infty}^{x} \frac{1}{y^2} de^y$$

$$= \frac{e^x}{x} + \frac{1}{y^2} e^y \Big|_{-\infty}^{x} - \int_{-\infty}^{x} e^y d\frac{1}{y^2}$$

$$= \frac{e^x}{x} + \frac{e^x}{x^2} + 2\int_{-\infty}^{x} \frac{e^y}{y^3} dy$$

$$= \frac{e^x}{x}\left(1 + \frac{1}{x}\right) + 2\int_{-\infty}^{x} \frac{1}{y^3} de^y$$

$$= \frac{e^x}{x}\left(1 + \frac{1}{x}\right) + 2\left(\frac{e^x}{x^3}\right) - 2\int_{-\infty}^{x} e^y d\frac{1}{y^3}$$

$$= \frac{e^x}{x}\left(1 + \frac{1}{x} + \frac{2}{x^2}\right) + 3\cdot 2\int_{-\infty}^{x} \frac{1}{y^4} de^y$$

$$= \frac{e^x}{x}\left(1 + \frac{1}{x} + \frac{2}{x^2} + \frac{3!}{x^3} + \frac{4!}{x^4} + \ldots\right).$$

$$(4.14)$$

Redhead indicated that only taking the first two terms of eq (4.14) [27] ($E_a/2RT \gg 1$), and then eq (4.13) is estimated as follows:

$$\ln\frac{\theta}{\theta_0} = -\frac{A_0}{a}\left(T\exp\left(-\frac{E_a}{RT}\right) - T_0\exp\left(-\frac{E_a}{RT_0}\right) + \frac{E_a}{R}\int_{\frac{E_a}{RT_0}}^{\frac{E_a}{RT}} \frac{\exp(u)}{u} du\right)$$

$$= -\frac{A_0}{a}\left(T\exp\left(-\frac{E_a}{RT}\right) - T_0\exp\left(-\frac{E_a}{RT_0}\right) + \frac{E_a}{R}\left(-\int_{-\infty}^{\frac{E_a}{RT_0}} \frac{\exp(u)}{u} du + \int_{-\infty}^{\frac{E_a}{RT}} \frac{\exp(u)}{u} du\right)\right)$$

$$\approx -\frac{A_0}{a}\left(T\exp\left(-\frac{E_a}{RT}\right) - T_0\exp\left(-\frac{E_a}{RT_0}\right) + \frac{E_a}{R}\left(-\left(\frac{\exp(-\frac{E_a}{RT_0})}{-\frac{E_a}{RT_0}}\left(1 + \frac{1}{-\frac{E_a}{RT_0}}\right)\right) + \left(\frac{\exp(-\frac{E_a}{RT})}{-\frac{E_a}{RT}}\left(1 + \frac{1}{-\frac{E_a}{RT}}\right)\right)\right)\right)$$

$$= -\frac{A_0}{a}\left(T\exp\left(-\frac{E_a}{RT}\right) - T_0\exp\left(-\frac{E_a}{RT_0}\right) + T_0\left(1 - \frac{RT_0}{E_a}\right)\exp\left(-\frac{E_a}{RT_0}\right) - T\left(1 - \frac{RT}{E_a}\right)\exp\left(-\frac{E_a}{RT}\right)\right)$$

$$= -\frac{A_0}{a}\left(\frac{RT^2}{E_a}\exp\left(-\frac{E_a}{RT}\right) - \frac{RT_0^2}{E_a}\exp\left(-\frac{E_a}{RT_0}\right)\right).$$

$$(4.15)$$

So the surface coverage θ is given by

$$\theta = \theta_0 \exp\left(-\frac{A_0}{a} \left(\frac{RT^2}{E_a} \exp\left(-\frac{E_a}{RT} \right) - \frac{RT_0^2}{E_a} \exp\left(-\frac{E_a}{RT_0} \right) \right) \right).$$ (4.16)

Eq (4.16) relates the surface coverage θ with respect to temperature T, given activation

energy E_a and pre-exponential factor A_0. Here we use T_0 as the reference temperature, at

which the surface coverage set as 1.

Eqs (4.11) and (4.16) show that for first-order reactions with a linear temperature sweep

both the peak temperature T_p and surface coverage θ are governed by the activation

energy and pre-exponential factor. The activation energy and pre-exponential factor are

often determined using Arrhenius plot from experimental desorption kinetics data [30]. By

taking natural logarithm on both sides of eq (4.6), we obtain

$$\ln(k_d) = \ln(A_0) - \frac{E_a}{RT}$$ (4.17)

Thus a plot of $\ln(k_d)$ against $1/T$ should be linear, and averages of activation energy and

pre-exponential factor are given from the slope and the intercept.

References

1   Marmur, J.; Doty, P., "Determination of the Base Composition of
        Deoxyribonucleic Acid from its Thermal Denaturation Temperature", *J. Mol. Biol.*
        1962, *5*, 109-118.

2   Schildkraut, C.; Lifson, S., "Dependence of the Melting Temperature of DNA on
        Salt Concentration", *Biopolymers* **1965**, *3*, 195-208.

3   Berestetskaya, I. V.; Frank-Kamenetskii, M. D.; Lazurkin, Y. S., "Effect of Ionic
        Conditions on DNA Melting Curve Parameters", *Biopolymers* **1974**, *13*, 193-205.

4   Owczarzy, R.; You, Y.; Moreira, B. G.; Manthey, J. A.; Huang, L.; Behlke, M. A.,
        "Effects of Sodium Ions on DNA Duplex Oligomers: Improved Predictions of
        Melting Temperatures", *Biochemistry* **2004**, *43*, 3537-3554.

5   Voet, D.; Voet, J. G.; Pratt, C. W. *Fundamentals of Biochemistry*; Upgrade ed.;
        John Wiley & Sons, Inc., 2001,

6   Sambrook, J.; Fritsch, E. F.; Maniatis, T. *Molecular Cloning: A Laboratory
        Manual* 2nd ed.; Cold Spring Harbor Laboratory Press: Cold Spring Harbor, NY,
        1989,

7   Breslauer, K. J.; Frank, R.; Blocker, H.; Marky, L. A., "Predicting DNA Duplex
        Stability from the Base Sequence", *Proc. Natl. Acad. Sci. USA* **1986**, *83*, 3746-
        3750.

8   John SantaLucia, J., "A Unified View of Polymer, Dumbbell, and Oligonucleotide
        DNA Nearest-Neighbor Thermodynamics", *Proc. Natl. Acad. Sci. USA* **1998**, *95*,
        1460-1465.

9   DeVoe, H.; Ignacio Tinoco, J., "The Stability of Helical Polynucleotides: Base
        Contributions", *J. Mol. Biol.* **1962**, *4*, 500-517.

10   Crothers, D. M.; Zimm, B. H., "Theory of the Melting Transition of Synthetic Polynucleotides: Evaluation of the Stacking Free Energy", *J. Mol. Biol.* **1964**, *9*, 1-9.

11   John SantaLucia, J.; Allawi, H. T.; Seneviratne, P. A., "Improved Nearest-Neighbor Parameters for Predicting DNA Duplex Stability", *Biochemistry* **1996**, *35*, 3555-3562.

12   Nasef, H.; Beni, V.; O'Sullivan, C. K., "Electrochemical Melting-Curve Analysis", *Electrochemistry Communications* **2010**, *12*, 1030-1033.

13   Peterlinz, K. A.; Georgiadis, R. M.; Herne, T. M.; Tarlov, M. J., "Observation of Hybridization and Dehybridization of Thiol-Tethered DNA Using Two-Color Surface Plasmon Resonance Spectroscopy", *J. Am. Chem. Soc.* **1997**, *119*, 3401-3402.

14   Taton, T. A.; Mirkin, C. A.; Letsinger, R. L., "Scanometric DNA Array Detection with Nanoparticle Probes", *Science* **2000**, *289*, 1757-1760.

15   Lehr, H.-P.; Reimann, M.; Brandenburg, A.; Sulz, G.; Klapproth, H., "Real-Time Detection of Nucleic Acid Interactions by Total Internal Reflection Fluorescence", *Anal. Chem.* **2003**, *75*, 2414-2420.

16   Liu, W.-T.; Mirzabekov, A. D.; Stahl, D. A., "Optimization of an Oligonucleotide Microchip for Microbial Identification Studies: a Non-equilibrium Dissociation Approach ", *Environmental Microbiology* **2001**, *3*, 619-629.

17   Li, E. S. Y.; Ng, J. K. K.; Wu, J.-H.; Liu, W.-T., "Evaluating Single-base-pair Discriminating Capability of Planar Oligonucleotide Microchips Using a Non-equilibrium Dissociation Approach", *Environmental Microbiology* **2004**, *6*, 1197-1202.

18   Urakawa, H.; Noble, P. A.; Fantroussi, S. E.; Kelly, J. J.; Stahl, D. A., "Single-Base-Pair Discrimination of Terminal Mismatches by Using Oligonucleotide Microarrays and Neural Network Analyses", *Applied and Environmental Microbiology* **2002**, *68*, 235-244.

19   Urakawa, H.; Fantroussi, S. E.; Smidt, H.; Smoot, J. C.; Tribou, E. H.; Kelly, J. J.; Noble, P. A.; Stahl, D. A., "Optimization of Single-Base-Pair Mismatch

Discrimination in Oligonucleotide Microarrays", *Applied and Environmental Microbiology* **2003**, *69*, 2848-2856.

20   Wick, L. M.; Rouillard, J. M.; Whittam, T. S.; Gulari, E.; Tiedje, J. M.; Hashsham, S. A., "On-chip Non-equilibrium Dissociation Curves and Dissociation Rate Constants as Methods to Assess Specificity of Oligonucleotide Probes", *Nucleic Acids Research* **2006**, *34*, e26.

21   Howell, W. M.; Jobs, M.; Gyllensten, U.; Brookes, A. J., "Dynamic Allele-Specific Hybridization", *Nature Biotechnology* **1999**, *17*, 87-88.

22   Collins, F. S.; Guyer, M. S.; Chakravarti, A., "Variations on a Theme: Cataloging Human DNA Sequence Variation", *Science* **1997**, *278*, 1580-1581.

23   Hacia, J.; Brody, L.; Collins, F., "Applications of DNA Chips for Genomic Analysis", *Molecular Psychiatry* **1998**, *3*, 483–492.

24   Southern, E.; Mir, K.; Shchepinov, M., "Molecular interactions on microarrays", *Nature Genetics Supplement* **1999**, *21*, 5-9.

25   Peterson, A. W.; Wolf, L. K.; Georgiadis, R. M., "Hybridization of Mismatched or Partially Matched DNA at Surfaces", *J. Am. Chem. Soc.* **2002**, *124*, 14601-14607.

26   Liu, W.-T.; Wu, J.-H.; Li, E. S.-Y.; Selamat, E. S., "Emission Characteristics of Fluorescent Labels with Respect to Temperature Changes and Subsequent Effects on DNA Microchip Studies", *Applied and Environmental Microbiology* **2005**, *71*, 6453-6457.

27   Redhead, P. A., "Thermal Desorption of Gases", *Vacuum* **1962**, *12*, 203-211.

28   Seebauer, E. G.; Kong, A. C. F.; Schmidt, L. D., "The Coverage Dependence of the Pre-Exponential Factor for Desorption", *Surface Science* **1988**, *193*, 417-436.

29   Allawi, H. T.; John SantaLucia, J., "Thermodynamics and NMR of Internal GT Mismatches in DNA", *Biochemistry* **1997**, *36*, 10581-10594.

30   Fogler, H. S. *Elements of Chemical Reaction Engineering*; 4th ed.; Pearson Education: Upper Saddle River, NJ, 2006,

CHAPTER V

PSORALEN CROSS-LINKING AND DNA NON-EQUILIBRIUM DESORPTION
ON A PATTERNED SURFACE

5.1 Introduction

This chapter is concerned with simultaneously obtaining multiple melting curves from a patterned 2-D surface by a non-equilibrium thermal desorption experiment. In Chapter II, I showed a method to prepare a 2-D surface architecture, and gene-specific DNA probes can be immobilized to the surface by their hybridization to surface oligos. However, the hydrogen binding between the DNA probes and the oligo surface is non-covalent, thus the probes can desorb from the surface under melting experiments. To maintain the attachment of the probes to the surface through the planned heating experiments, a stronger covalent bond between the probes and the surface would offer greater stability.

Psoralens (furocoumarins) are a common linker for DNA duplexes to improve their stability. They are a class of rigid, planar, three-ring heterocyclic compounds, and their core structure is shown in Figure 5.1. Psoralen molecules readily intercalate within double-strand DNA helices, and cyclobutane adducts are formed between psoralen and adjacent pyrimidine molecules upon exposure to long-wavelength UV irradiation (365 nm) [1,2]. Psoralens favor reaction with thymidine in DNA, although a minor reaction

exists with cytosine [3]. Researchers have used methylated psoralen derivatives to crosslink two complementary single-stranded DNAs to generate DNA duplexes with enhanced thermal stabilities in solution. For example, temperature denaturation data in solution of a psoralen-modified 18-mer DNA have indicated that the melting temperature can increase from 32 ℃ for an unmodified 18-mer to 40 ℃ for the modified version [4].

Psoralen-containing phosphoramidites are commercially available from Glen Research (Sterling, Virginia), making it easy to introduce them into a stepwise oligo synthesis. Previous research in the Laibinis' group has indicated that psoralen phosphoramidites can crosslink A-T base pairs in double-stranded DNA molecules at surface. Different psoralen cross-linking strategies were tested, and it showed that best psoralen crosslinking efficiency was obtained when the psoralen crosslinker was attached to the 5' end of the surface oligos [5], possibly due to less steric hindrance. Base on this previous result from our group, I chose to use psoralen C2 phosphoramidite for synthesizing surface oligos with 5' psoralen linkers.

Here in this chapter the first goal is to determine the optimized experimental conditions to crosslink the probes to the surface oligos, thereby providing a covalent linkage between the probes and the substrate surface. The second goal is to use such patterned surface to obtain multiple melting curves.
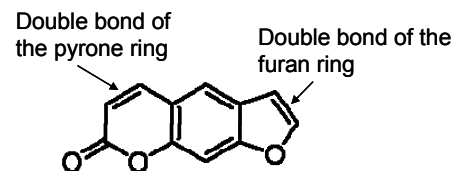
Figure 5.1. Psoralen structure.

5.2 Methods and materials

Surface preparation. Microscopic slides were cleaned in piranha solution (7:3(v/v),

concentrated H_2SO_4 : 30% H_2O_2. Caution: "piranha" solution reacts violently with

organic material and should be used with great care.) for 30 min, followed by rinsing

with copious quantities of DI water and drying under a N_2 stream. The slides were then

immersed into a 1 wt.% N-(3-triethoxysilylpropyl)-4-hydroxy-butyramide (Gelest,

Morrisville, PA) solution in 95% ethanol for 16 hours to produce a hydroxyl silane

surface. The slides were removed from the silane solution, rinsed sequentially with

ethanol and water, and then blown dry with N_2. Then the slides were heated in an oven at

~110 °C for 30 min to anneal the films.

Solid phase synthesis of psoralen-modified surface oligos. Surface oligonucleotides

were synthesized from the hydroxyl group using phosphoramidite chemistry (see Chapter

II). After the surface oligos were synthesized at surface, psoralen C2 Phosphoramidite

(Glen Research, Sterling, VA), 2-[4'-(hydroxymethyl)-4,5',8-trimethylpsoralen]-ethyl-1-

O-(2-cyanoethyl)-(N,N-diisopropyl)-phosphoramidite, was used under standard

phosphoramidite chemistry conditions to modify the surface oligonucleotides. After the

synthesis, the slide was removed from the synthesizer, rinsed sequentially with ethanol

and water, and then immersed into an ethylenediamine/ethanol (50/50, v/v) solution for

one hour to remove both the base and phosphate protective groups [6,7]. Following the

deprotection, the sample was rinsed sequentially with ethanol and water, blown dry with

N_2, and used as a substrate in spotting experiments. The sequence of the surface oligos is

shown in Figure 5.2.

Immobilization of DNA probes to surface by robotic spotting. Spotting was

performed with a single solid pin using a microarray spotting station (MiraiBio Inc.,

South San Francisco, CA). The spotting volume of each spot was ~2 nL according to the

manufacturer's specification and the spot size was ~240 μm in diameter. Non-

fluorescence tagged probe DNA (4μM, 0.26 M [Na^+]) was spotted onto the prepared

oligo surface. The sequence of the probe DNA is shown in Figure 5.2. After spotting,

the slide was placed in a Corning hybridization chamber and stored at room temperature

for 5 hours. Following the hybridization, the surface was rinsed in 1 × SSC buffer

solution and blown dry under a stream of N_2.

Psoralen cross-linking. After the immobilization of probe DNA, the slide was

immersed into 60 mL 1×SSC buffer in a glass petri dish, and the slide was illuminated

under 365 nm UV light for half an hour. The distance between the light bulb and the

slide surface was about 4 inches. The light source was a 100 watts 365 nm longwave UV

lamp (UVP, Upland, CA). The illumination was performed at room temperature inside a

photochemical safety cabinet (Ace Glass Inc, Vinland, NJ), and the petri dish was placed

on top of one pack of gel ice to minimize the thermal effect of the UV light to the buffer

solution. A thermocouple was placed into the buffer solution, and its temperature was

monitored during the UV illumination. The solution temperature increased gradually

from 12 °C to 18 °C. After the UV irradiation, the slide was immersed into 0.2% SDS in

80 mL TE buffer solution and heated at 60 °C for half an hour to remove those probe

DNA molecules that were not cross-linked. Then the slide was rinsed with DI water and

blown dry under N_2.

Hybridization between probe and target DNA. The probe DNA molecules were hybridized with 40 μL of 2 μM target DNA solution by pipetting the target solution on the probe region and covering it with a 22×22 mm glass coverslip (Fisher Scientific). The slide was transferred into a hybridization chamber (Corning, Corning, NY) and the humidification wells of the chamber were filled with 10 μL of 1×TE buffer (10mM Tris buffer and 1 mM EDTA, pH 8.0), and the chamber was kept at room temperature for 16 hours to allow for hybridization. Afterward the surface was washed at room temperature with 1×SSC buffer, and blown dry under N_2. The sample was then scanned with a GenePix 4000B laser scanner (Molecular Devices, Sunnyvale, CA). The sequence of the fluorescently-tagged target and the surface linkage are shown in Figure 5.2.

Surface melting curves (desorption kinetics). The methods for measuring surface desorption melting curves and data analysis have been described previously in Chapter IV and will not be repeated here. To find the spots and determine the mean intensity for each spot, the "Microarray Spot Finding Example" from MATLAB Central was referenced [8].

3'- TTTTTACGCTACAAGTACGGAA-psoralen-5'

Surface oligo with psoralen modification at 5' end

5'-TGCGATGTTCATGCCTTTTTATCTTAGCACCTCCG -3'

Non-fluorescence tagged probe DNA

3'-Cy3-TAGAATCGTGGAGGC-5'

Fluorescently-tagged target DNA

Spacer

Psoralen cross-linking with T's

Slide surface-3'-TTTTT ACGCTACAAGTACGGAA-psoralen-5'

5'-TGCGATGTTCATGCC TT TTT ATCTTAGCACCTCCG -3'

3'-Cy3-TAGAATCGTGGAGGC-5'

Linking surface oligo with probe DNA

Probe/target DNA

Figure 5.2. The sequences of psoralen-modified surface oligos, non-fluorescence tagged probe DNA, and fluorescently-tagged target DNA, and the schematic illustration of their complemarities and linkage at surface. The probe DNA has five T's in the middle of the sequence, which is designed for psoralen to cross-link with.

5.3 Results and discussion

Psoralen cross-linking efficiency. Previous research at the Laibinis' group have showed that it is more efficient to cross-link DNA duplexes at surface by adding psoralen to the end of the immobilized surface oligos during the DNA synthesis process than having psoralen linked with non-immobilized target [5]. In addition, it is convenient to add psoralen to surface oligos at the DNA synthesis step by using psoralen C2 phosphoramidite which is commercially available from Glen Research (Sterling, Virginia). This strategy, i.e., having psoralen-modified surface oligos, is used in this work.

To determine the psoralen cross-linking efficiency, the surface was coverslip-hybridized before and after the cross-linking, and the fluorescent intensities were compared. Figure 5.3(A) illustrated the process. Psoralen-modified surface oligonucleotides were first synthesized on a glass slide surface, with psoralen as the last addition step. Probe DNA was then immobilized to the surface via hybridization between probe and surface oligonucleotides. The probe DNA was hybridized to fluorescently-tagged target to measure the intensity before irradiation. Under UV irradiation, the psoralen cross-links with the probe DNA strands covalently. After the irradiation, the surface was heated to remove those probes that were not cross-linked during the irradiation step, and surface was hybridized again with the target to determine the fluorescent intensity after psoralen cross-linking. The scanned images before and after the psoralen cross-linking are shown in Figure 5.3(B). Using the calibration curve in Chapter II (Figure 2.5), the surface density of DNA duplexes changes from 2×10^{12} molecules/cm^2 before psoralen cross-linking to 1×10^{12} molecules/cm^2 after psoralen

133

cross-linking and heating steps. Thus the psoralen cross-linking efficiency is ~ 50%,

comparing to a coupling efficiency of 75% for psoralen cross-linking in solution phase [4].
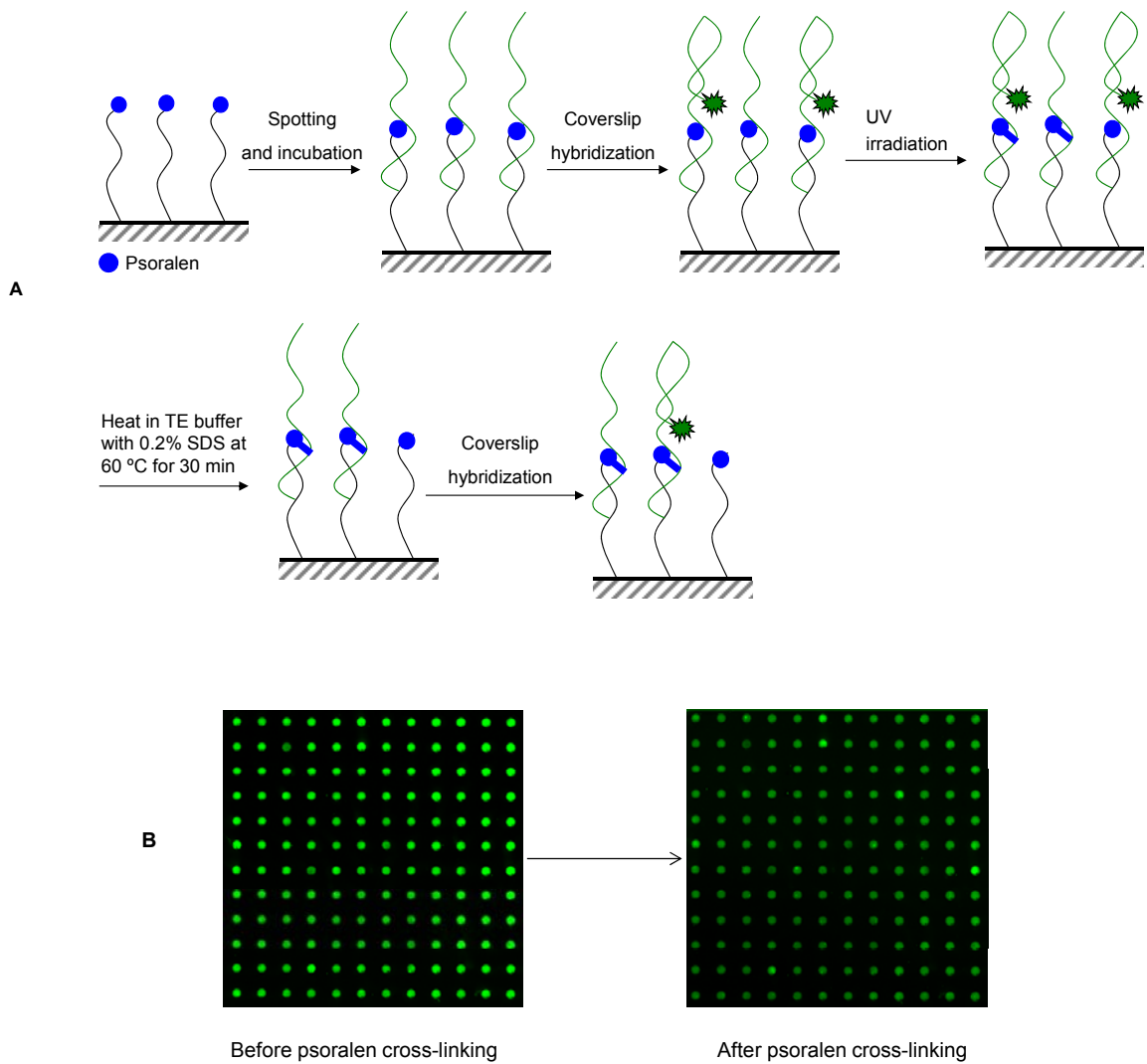
Figure 5.3. Psoralen cross-linking. (A) schematic illustrations of covalent attachment of probe DNA to surface by psoralen cross-linking. (B) scanned fluorescence images of the coverslip-hybridized surface before the UV irradiation step and after the UV irradiation and heating steps.

DNA melting on a patterned array surface. In Chapter IV we investigated DNA

melting behaviors on a homogeneous surface. By preparing a patterned surface as

discussed in Chapter II and using psoralen to covalently cross-link the probe DNA

molecules to surface as examined in this work earlier, DNA melting behaviors can be

monitored on a patterned surface. Typically multiple melting curves from each spot are

obtained simultaneously by a single non-equilibrium desorption experiment. Shown in

Figure 5.4 are the fluorescent images of a patterned surface taken at different

temperatures during a linear sweep experiment. All the 64 spots on the surface have the

same probe/target sequence (Figure 5.2). During the linear temperature sweep, the

fluorescent intensities from the spots decay with the temperature increase until reaching

the background intensity level.

Figure 5.5 (A) shows the TIRF image of the 64 spots at the beginning of the

temperature sweep (i.e., at the initial temperature of 25.1 °C) with 0.5 M NaCl circulating

across the sample surface. The TIRF fluorescence intensities of the spots depend on the

spot positions, as shown in Figure 5.5 (B). For comparison, Figure 5.6 (A) shows the

scanned image of the patterned DNA surface before the melting experiment (the sample

was washed in 1 × SSC before scanning.). The scanned fluorescence intensities of the 64

spots are shown in Figure 5.6 (B). In the TIRF image, for every 8 spots from each

column in Figure 5.5 (A), i.e., spots 1-8, 9-16, 17-24, 25-32, 33-40, 41-48, 49-56, 57-64,

the central three to four spots have higher fluorescence intensities than the other spots at

both sides. This is almost opposite to the trend observed in the scanned image. The

reason of the intensity variations in each column between spots is probably due to the

non-uniformity of the incident light. In the TIRF setup (Chapter III), the expanded

incident laser beam has a Gaussian intensity profile, and when the laser beam is totally reflected at the interface between the slide and the buffer solution, the illuminated surface area has an elongated elliptical shape. The incident light is more uniform in the elongated x-direction than that in the non-elongated y-direction. Another observation is that in the TIRF image the intensities from the central spots from each column increase from column 1 to column 8. This trend is also observed in the scanned image, but not as significant as the TIRF image. So the intensity variations of the central spots from column to column is probably also affected by the non-uniformity of the incident light, but not as significant as those in y-direction.

For each spot, the normalized fluorescent intensity was obtained from the non-equilibrium melting experiment, and plotted with the solution temperature, as shown in Figure 5.7 (A) for a representative spot. The desorption rate is shown in Figure 5.7 (B). Both curves are fitted using a MATLAB cubic smoothing spline function (csaps). The half temperature and the peak temperature were determined using the fitted curves. Both characteristic temperatures are defined in Chapter IV, i.e., the half temperature is the temperature at which the normalized intensity reaches 0.5, and the peak temperature is the temperature at which the desorption rate is a maximum. Figures 5.8 and 5.9 show the half and the peak temperatures, respectively. The mean half temperature and its standard deviation from all the 64 spots is 49.5 ± 0.7 °C, and the mean peak temperature and its standard deviation is 54.1 ± 0.8 °C. Both the half and peak temperatures show similar variations from spot to spot, however, these variations do not correlate to those of initial fluorescence intensities (Figures 5.5 and 5.6).

In comparison to a homogeneous surface, the half temperature for the same sequence was measured as 51.7 °C (temperature step width 0.3 °C, Chapter IV). The difference of the half temperatures between the homogeneous and the patterned surfaces is probably due to the surface densities. As we recall from the preparation methods for the two surfaces, the homogeneous surface was hybridized once by the target solution with a coverslip, while the patterned surface was first hybridized with probes in a printed solution, then cross-linked with probes under UV irradiation, followed by the second hybridization with targets using a coverslip. Although the hybridization efficiencies for the printing or coverslip methods were not determined, we do know that the psoralen cross-linking efficiency is ~ 50%, which means the probe-target duplex density of the patterned surface is at least 50% less than that of the homogeneous one. Such difference in surface density probably contributes to the variations in their half temperatures. On the other hand, the peak temperature obtained from the patterned surface (54.1 ± 0.8 °C) is more consistent with that determined on the homogeneous surface (54.9 °C, temperature step width 0.3 °C), indicating that the peak temperature is probably more independent on the surface coverage.

Temperature increases
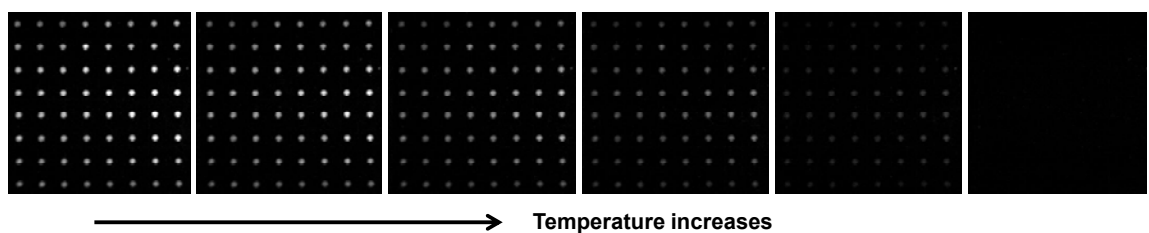
Figure 5.4. The fluorescence intensity of spots on a patterned surface changes with temperature during a linear sweep desorption experiment. The first image was taken at temperature 25 °C, and the temperature increase between every two neighboring images was ~ 6.5 °C. Spot size: ~ 240 µm.
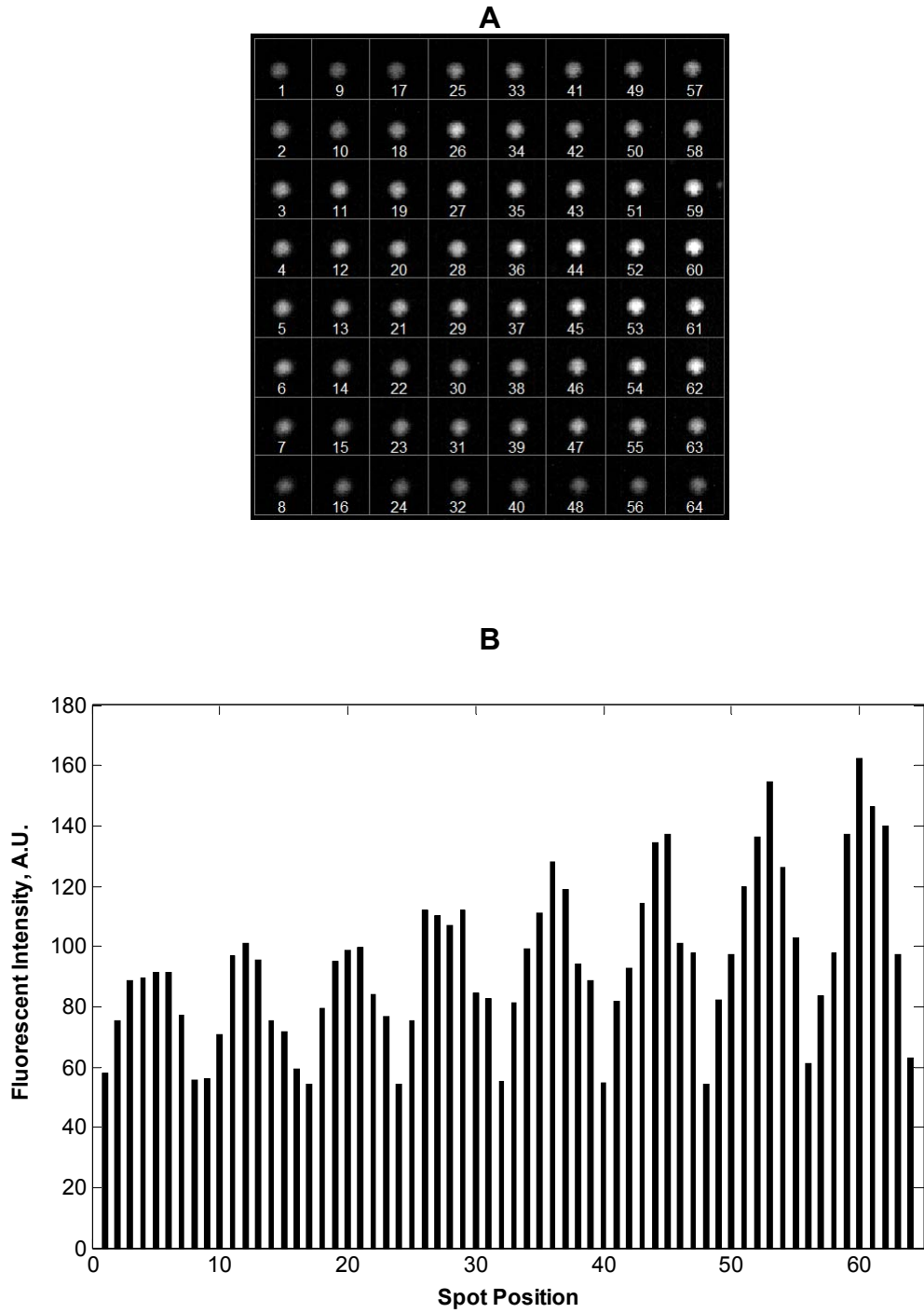
Figure 5.5. (A) TIRF image of the patterned DNA spots at 25.1 °C with the spot numbers showing under the spots. (B) The bar chart of the fluorescent intensities of the 64 spots.
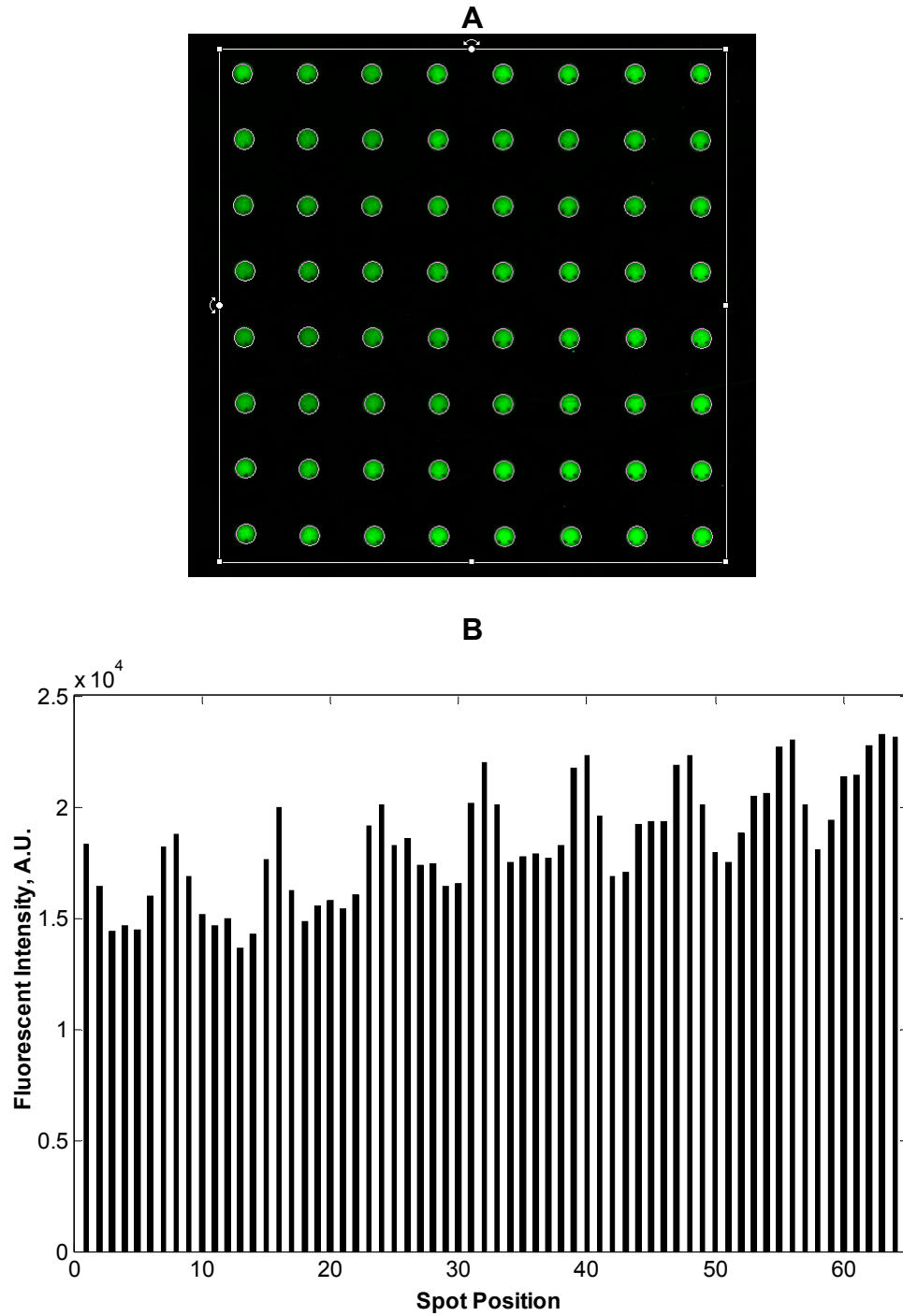
Figure 5.6. (A) Scanned image of the patterned DNA surface. Spot size: 240 μm, and spot center to spot center distance is 800 μm. (B) The bar chart of the fluorescent intensities of the 64 spots.

A

B
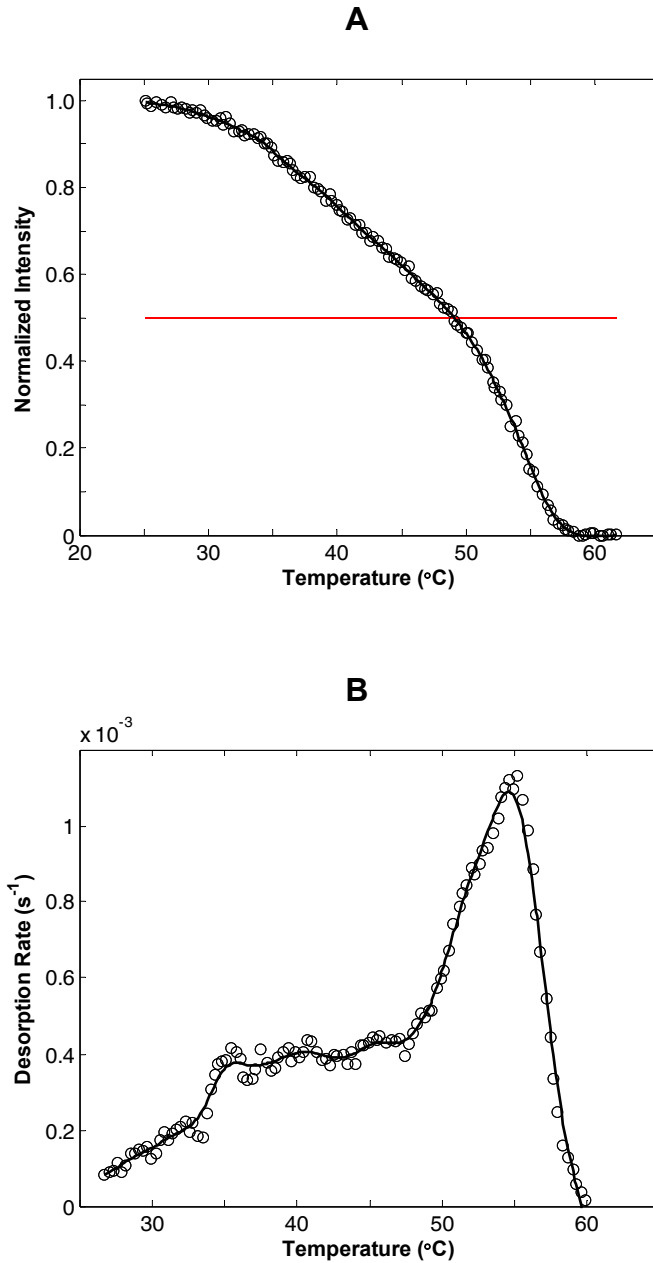
Figure 5.7. (A) A representative non-equilibrium desorption curve at spot 60 on the patterned DNA surface (spot 60). (B) A representative desorption rate curve from spot 60 at the patterned DNA surface. The lines in both curves are the cubic smoothing spline fittings to the experimental data using MATLAB function: csaps.

A

48.3	48.7	48.3	48.3	49.1	49.0	49.1	48.0
49.0	48.8	48.9	49.1	48.5	49.4	48.6	47.9
49.4	49.4	49.1	49.5	49.1	49.9	48.6	48.5
49.8	49.5	49.8	49.7	50.0	49.9	48.9	49.0
49.8	49.9	50.0	50.0	50.2	50.1	49.2	49.9
49.8	49.8	50.2	50.1	50.3	50.0	49.6	50.5
50.6	50.5	50.4	50.9	50.6	50.3	49.6	50.4
50.1	50.3	50.4	50.0	49.9	49.2	49.8	50.0

B
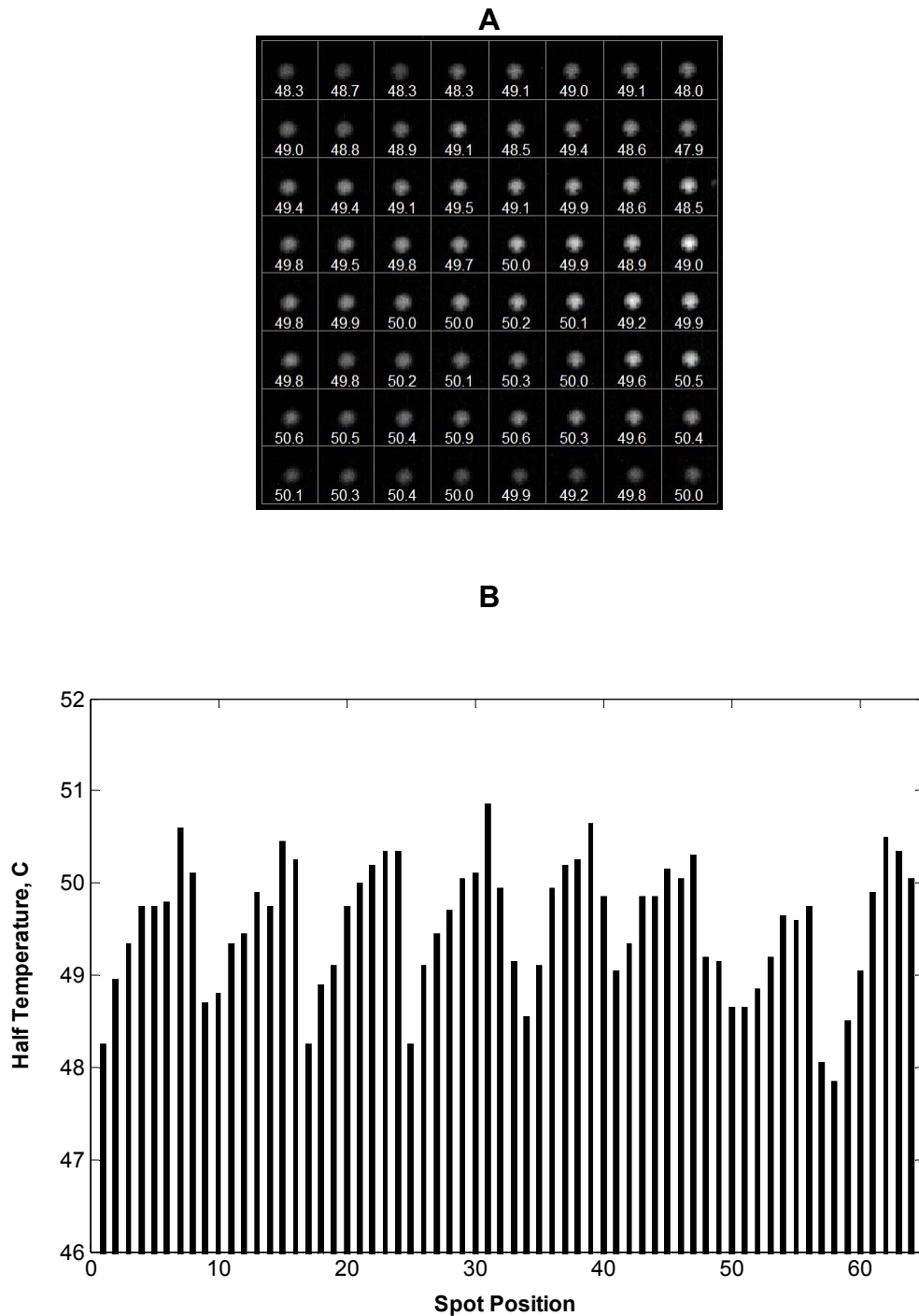
Figure 5.8. (A) The TIRF image of the pattered DNA array showing the half temperatures for each spot, unit: °C. (B) The bar chart of the half temperatures for the 64 spots. Each spot has 15-mer perfectly matched probe-target duplexes with the same sequence. The half temperature, $T_{0.5}$, is defined as the temperature at which the normalized fluorescent intensity reaches 0.5.

A

52.8	51.3	52.2	53.1	53.1	52.8	53.3	53.3
53.3	53.2	53.3	53.6	53.1	53.2	53.1	53.1
53.6	53.4	53.7	53.6	53.5	53.5	53.4	53.8
53.9	54.4	54.5	54.2	54.2	54.4	54.3	54.6
54.5	54.4	54.9	54.9	55.1	55.1	55.0	54.9
54.4	54.9	54.5	54.7	55.0	55.1	54.9	54.8
54.8	54.7	55.0	55.3	55.0	54.1	54.6	54.5
55.0	55.0	55.0	54.9	54.0	53.9	54.2	54.4

B
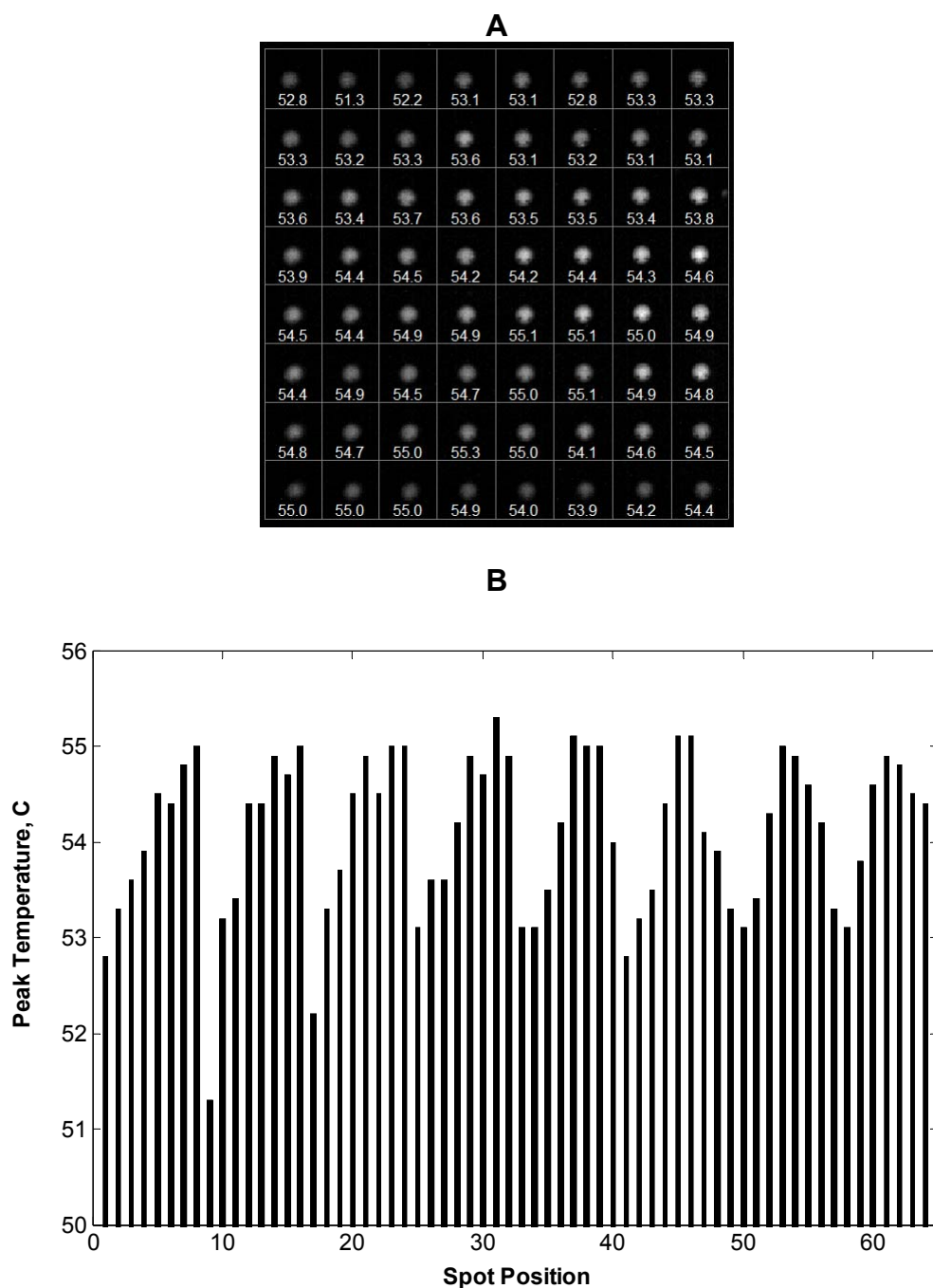
Figure 5.9. (A) The TIRF image of the patterned DNA array showing the peak temperatures for each spot. Unit: °C. (B) The bar chart of the peak temperatures for the 64 spots. Each spot has 15-mer perfectly matched probe-target duplexes with the same sequence. The peak temperature, T_p, is determined as the temperature at which the desorption rate reaches a maximum.

144

5.4 Conclusions

Psoralen is used to modify the surface oligonucleotides during the DNA synthesis process, and provides covalent linkage between surface oligonucleotides and probe DNA molecules under UV irradiation. The psoralen cross-linking efficiency at surface is determined to be around 50%. Using the patterned surface with probe DNA covalently end-immobilized to surface, melting curves was obtained simultaneously for all the spots on the chip in a single non-equilibrium desorption experiment. The melting process was observed using total internal reflection fluorescence. For a 15-mer perfectly matched sequence, all the 64 spots on the chip surface show similar melting and desorption rate profiles. The half temperature is 49.5 ± 0.7 °C, and the peak temperature is 54.1 ± 0.8 °C. Comparing to the melting studies on the homogeneous surface in Chapter IV, the peak temperature is consistent from either homogenous or patterned surfaces, and much less dependent on the surface coverage than the half temperature.

References

1   Chatterjee, P. K.; Cantor, C. R., "Photochemical Production of Psoralen-DNA Monoadducts Capable of Subsequent Photocrosslinking", *Nucleic Acids Research* **1978**, *5*, 3619-3633.

2   Hearst, J. E., "Photochemistry of the Psoralens", *Chem. Res. Toxicol.* **1989**, *2*, 69-75.

3   Cimino, G. D.; Shi, Y.-b.; Hearst, J. E., "Wavelength Dependence for the Photoreversal of a Psoralen-DNA Cross-Link", *Biochemistry* **1986**, *25*, 3013-3020.

4   Pieles, U.; Englisch, U., "Psoralen Covalently Linked to Oligodeoxyribonudeotides: Synthesis, Sequence Specific Recognition of DNA and Photo-Cross-Linking to Pyrimidine Residues of DNA", *Nucleic Acids Research* **1989**, *17*, 285-299.

5   Lee, I. H., "Covalent End-Immobilization of Oligonucleotides onto Solid Surfaces", PhD thesis, Massachusetts Institute of Technology, 2001.

6   LeProust, E.; Zhang, H.; Yu, P.; Zhou, X.; Gao, X., "Characterization of Oligodeoxyribonucleotide Synthesis on Glass Plates", *Nucleic Acids Research* **2001**, *29*, 2171-2180.

7   Pirrung, M. C.; Fallon, L.; McGall, G., "Proofing of Photolithographic DNA Synthesis with 3',5'-Dimethoxybenzoinyloxycarbonyl-Protected Deoxynucleoside Phosphoramidites", *J. Org. Chem.* **1998**, *63*, 241-246.

8   http://www.mathworks.com/matlabcentral/fx_files/2573/2/content /R14_MicroarrayImage_CaseStudy/html/R14_MicroarrayImage_CaseStudy.html

CHAPTER VI

MALDI IMAGING MASS SPECTROMETRY

6.1 Introduction

Mass spectrometry is a powerful analytical tool for the determination of the

molecular mass and composition of a sample. It has become an indispensable analytical

method in the life science, especially in the proteomics research [1,2,3]. In mass

spectrometry, the analyte molecules need first to be intact ionized in the vapor phase

(either positively or negatively charged), and then the ions are separated by electric

and/or magnetic fields based on their mass-to-charge ratio (m/z). Traditionally the

analytes are limited to volatile chemicals, which readily form molecules in the vapor

phase in vacuo, and these gas-phase molecules are encountered and ionized with

electrons, chemical ions, photons, or electronically excited atoms or molecules [4,5]. These

methods of ionization are very energetic and can cause extensive fragmentation of the

analyte molecules. Very large bio-molecules such as proteins generally cannot be

vaporized, even in vacuo, as they are non-volatile, and thus they cannot be ionized using

the above classical ionization methods without extensive decomposition. Since late

1980's, a couple of important "soft" ionization methods were developed: electrospray

ionization (ESI) [5] and matrix-assisted laser desorption ionization (MALDI) [6,7]. These two innovative ionization methods have revolutionized the characterization of bio-molecules using mass spectrometry. The following will focus on MALDI and MALDI mass spectrometry imaging. The information on electrospray ionization is available in literature elsewhere [5,8-13].

Matrix-assisted laser desorption ionization (MALDI), coupled with time-of-flight (TOF) mass spectrometers is an important analytical tool to probe bio-molecules [14,15]. In a MALDI experiment, the matrix is usually strong absorbent of UV light (337 nm N_2 lasers are the common laser source for MALDI instruments), such as 2,5-dihydroxybenzoic acid (DHB) and sinapic acid (SA). A UV-Vis spectrum of 0.1 mg/mL DHB in 50:50 acetonitrile/water is shown in Figure 6.1.

Over the past decade, MALDI imaging mass spectrometry has emerged as an extraordinarily powerful technology to examine the relative abundance and spatial localization of lipids [16], peptides and proteins [17,18] in a thin tissue section. In an imaging mass spectrometry (IMS) experiment, sample preparation is critical in terms of obtaining high quality mass spectrometry signal after hand [19]. For such an experiment, usually a thin tissue section is prepared in a cryostat, and consequently mounted on a MALDI plate. Then the matrix solution is deposited onto the tissue surface using a low volume pipette, or an automatic acoustic matrix spotter [20], or the tissue surface can be coated with matrix crystals by sublimation [21]. By moving the MALDI plate in x and y direction, mass spectrometry spectra are obtained from different locations on the surface in a defined raster pattern, and each spectrum might have hundreds of peaks from a particular spot on the tissue surface. Images of selected ions of interest can be created to describe the

spatial distribution and relative abundance of those ions on the surface. The workflow of an imaging mass spectrometry experiment is illustrated in Figure 6.2 [22].

The application of imaging mass spectrometry will have a tremendous impact on biological and clinical sciences [23]. Protein images or profiles from diseased tissues may be specific to the disease and the disease state and thus can be used to identify the disease and the state or to access the prognosis of a patient. Imaging mass spectrometry can be used to study the molecular phenotypes expressed in cancers or other human diseases by comparing protein patterns in pre-lesion and tumor biopsies. These studies help clinicians assess and verify disease progression, prognosis and therapeutic efficacy. In addition, IMS may be used to identify the protein patterns for complex differentiating cells to probe protein markers specific to certain diseases. This technology will provide extraordinary power for researchers to investigate the molecular events in cells and tissues and enhance the understanding of the underlying biology of health and disease [23].
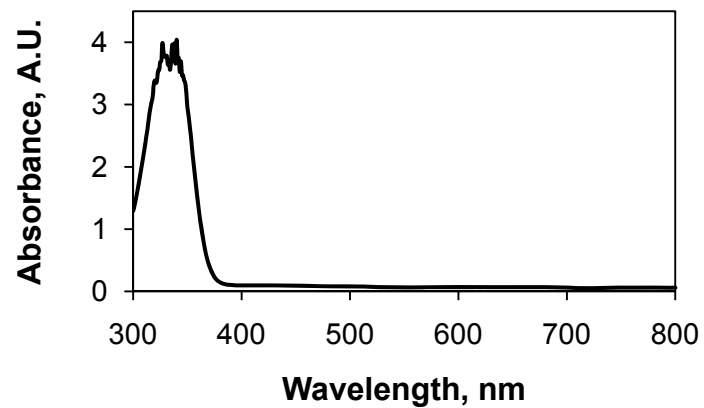
Figure 6.1. UV-Vis spectrum of 0.1 mg/mL 2,5-dihydroxybenzoic acid (DHB) in 50% acetonitrile in water with 0.1% trifluoroacetic acid.
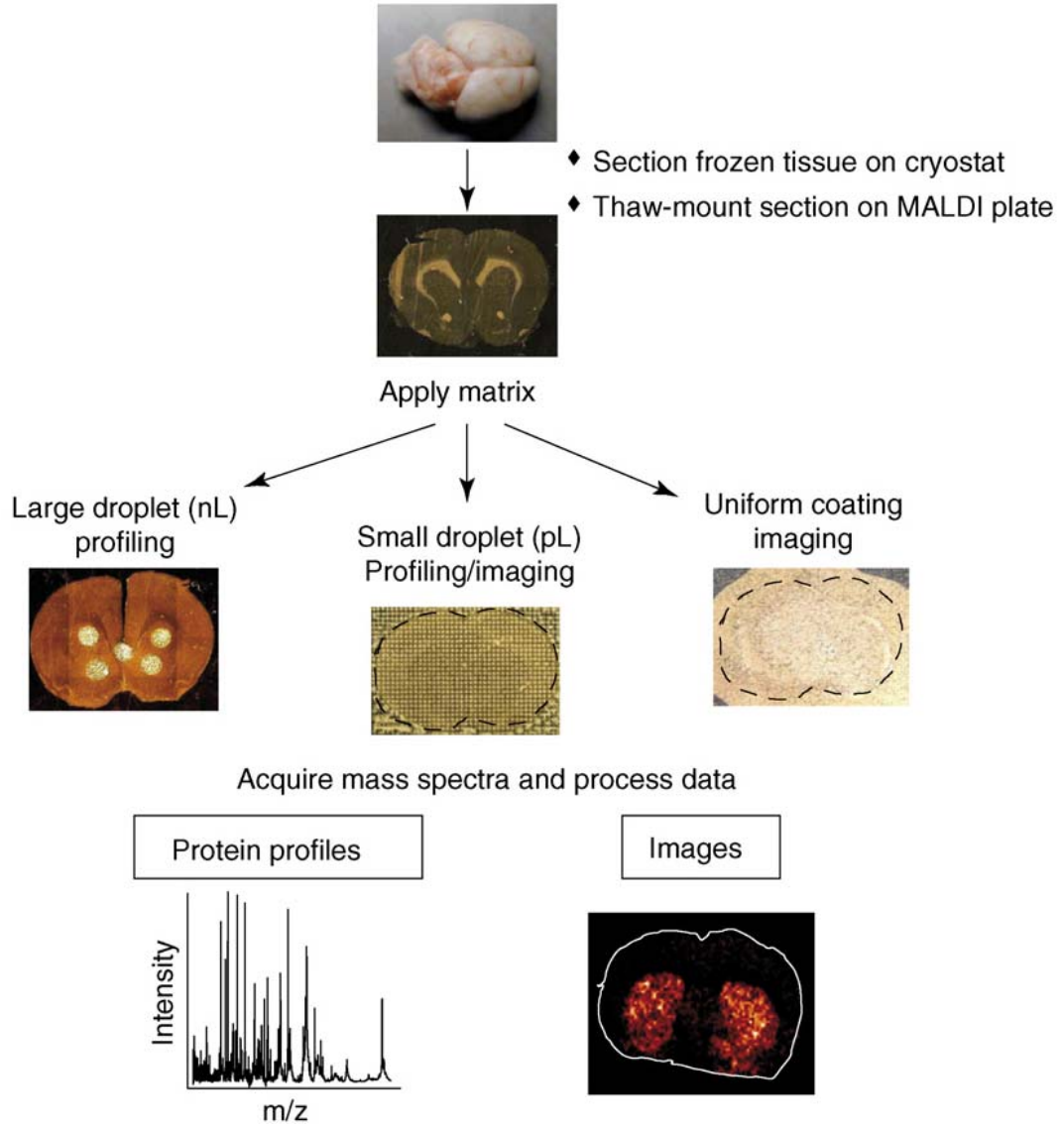
Figure 6.2. The workflow of an imaging mass spectrometry (IMS) experiment on a tissue section. (The figure is taken from a reference paper [22].)

6.2 Current sample preparation methods for imaging mass spectrometry

Direct tissue analysis using imaging mass spectrometry requires localizing matrix solution onto tissue surface. Practically, the matrix spots need to be discrete from each other as cross-talk between the spots jeopardizes the quality of the ion images due to possible protein delocalization or diffusion. At the same time, higher resolution image requires finer spot size. For this reason, sample preparation, especially matrix deposition onto a tissue surface, is critical for obtaining high quality data using imaging mass spectrometry.

Matrix can be applied onto the tissue surface by coating, sublimation or spotting using an automatic spotter. Whole tissue surface can be coated with matrix by spraying matrix solution directly onto the tissue surface using a glass spray nebulizer, by electrospray deposition, or by immersing the tissue into a matrix solution [19]. The problems with coating are that the protein signals are hardly reproducible due to non-efficient protein integration with the matrix crystals and possible protein delocalization across the tissue surface. Vapor-phase deposition of matrix by sublimation is considered as a solvent-free dry-coating approach [21]. Sublimation minimizes the spreading of analytes at surface, but usually this dry-coating process is not able to integrate proteins into the matrix crystals and is mainly applied for imaging lipids, which are in abundance on a tissue surface and easier to be ionized than proteins. Currently automated acoustic matrix deposition is routinely used for imaging mass spectrometry for proteins [20]. In an acoustic matrix spotter, a transparent lid covers the matrix reservoir to minimize the solvent evaporation, and the matrix solution is acoustically ejected from the solution and

passes through a 400-micron hole in the center of the lid to reach the sample surface. Figure 6.3 shows the scheme of the acoustic matrix spotter and the photographs of the formation of one matrix droplet. The Optimized droplet volume is about 120 picoliters, and multiple (about 20 to 30) droplets are required to generate a 220-300 μm matrix spot with high quality of mass spectrometry spectra. The spot-center to spot-center distance is around 400 microns. Acoustic spotter offers an alternative non-contact matrix deposition method, which eliminates concern for matrix clogging. Spots of matrix solution can be deposited onto a tissue surface as an array and allow imaging mass spectrometry to be performed. Protein migration or image resolution is limited to the size of matrix spots, which are around 220-300 μm. However, the spotting method has a few shortcomings. First, the spot size of 220-300 μm limits this method for higher resolution images; second, the acoustic spotter is expensive and may not be available to an ordinary lab; third, it is very time-consuming to spot a tissue surface. For example, taking the calibration time into account, the spotting speed is ~ 10 spots/s, thus it takes about one hour to spot matrix on a tissue section of 1 cm^2 at spotting resolution 300 μm with 30 cycles for each spot (i.e., totally there are ~ 33000 droplets to spot). If we were able to increase the spotting resolution to 50 μm, there will be 1200000 total droplets to spot, and the spotting time will be 33 hours! Obviously, with the elongated sample preparation time, it is not practical to spot matrix for high resolution images, such as spot center-to-center distance less than 50 μm.
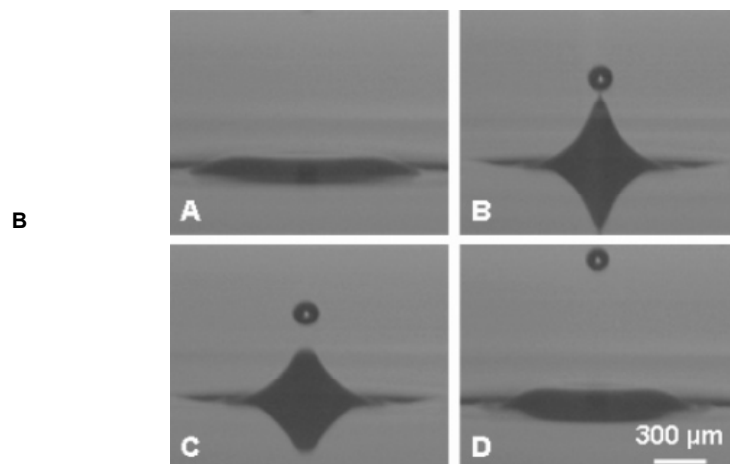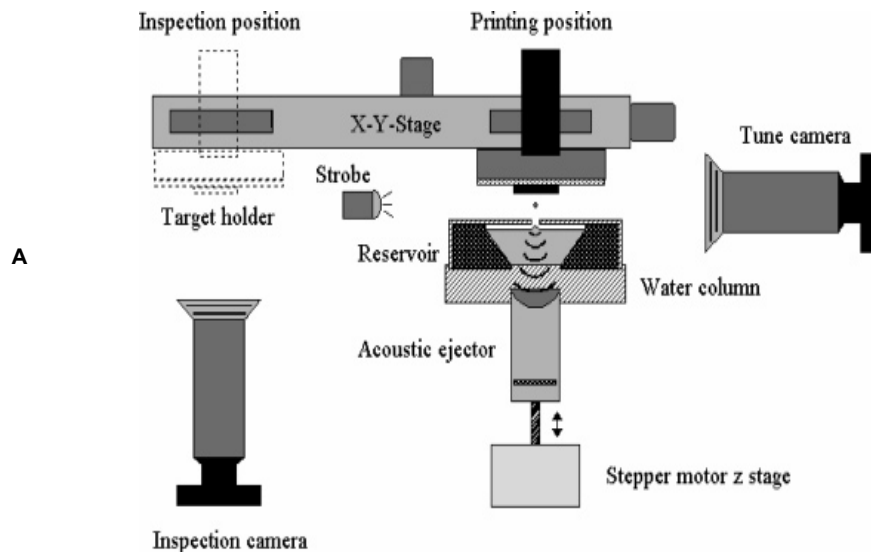
Figure 6.3. (A) Schematic illustration of an acoustic matrix spotter. (B) Photomicrographs showing the formation of a liquid droplet from the surface of the matrix solution by the acoustic matrix spotter. The images in (A) and (B) are taken from a reference paper [20].

6.3 Motivation of pre-coating a MS target surface for imaging mass spectrometry

In the sample preparation for imaging mass spectrometry, the most important is to locate the matrix onto the tissue surface as an array. To improve the resolution of the ion images, it is critical to have matrix spots as small as possible, and as dense as possible, with the condition that a high quality of signal can be achieved with the amount of matrix on each spot. The smaller the size of the matrix spot, the higher image resolution and possibly the less sensitive of the mass spectrometry signal. The aforementioned acoustic spotter has been routinely used in the lab for imaging mass spectrometry, but it suffers with difficulty to achieve finer resolution and long sample preparation time. The following describes a pre-coating method which can produce matrix spot size smaller than the acoustic spotter, and furthermore, the sample preparation time can be shortened from a couple of hours using an acoustic spotter to a couple of minutes using the pre-coating method.

Pre-coating target surface simplifies sample preparation for imaging mass spectrometry. The workflow of the pro-coating approach is illustrated in Figure 6.4. The approach starts with a solid surface, such as a gold coated silicon/glass slide surface or a regular MS target. The target surface is first patterned by microcontact printing and thus allows matrix crystals to be formed as an array format on the surface, as discussed in Chapter VII. After the surface modification and formation of matrix crystal array, tissue sample is applied to the surface and imaging mass spectrometry is performed to collect ion images. Chapter VIII provides details on the IMS experimental data and discussions.
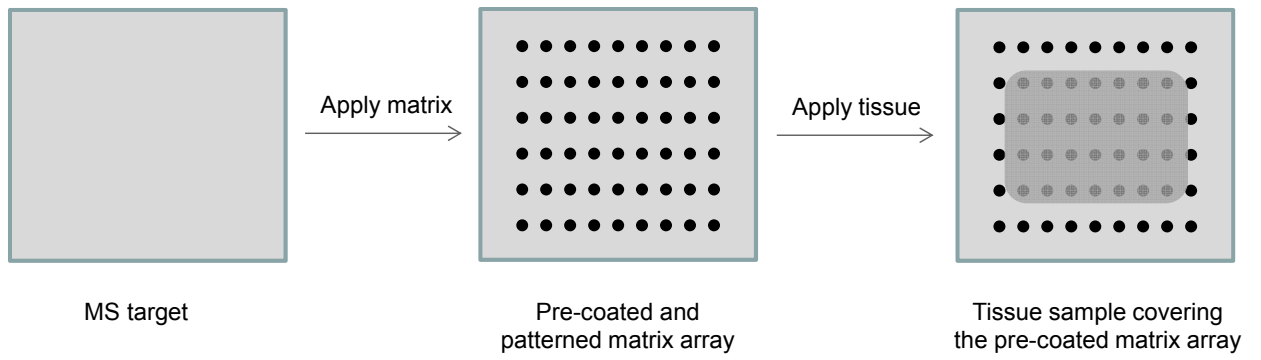
Figure 6.4. Pre-coating a target surface. Matrix array is pre-coated and patterned on a MS target. Tissue sample is then applied to cover the matrix array.

References

1   Domon, B.; Aebersold, R., "Mass Spectrometry and Protein Analysis", *Science* **2006**, *312*, 212-217.

2   *Mass Spectrometry Analysis for Protein-Protein Interactions and Dynamics*; Chance, M., Ed.; John Wiley & Sons, Inc.: Hoboken, New Jersey, 2008.

3   *Quantitative Proteomics by Mass Spectrometry*; Sechi, S., Ed.; Humana Press Inc.: Totowa, New Jersey, 2007.

4   Hoffmann, E. d.; Stroobant, V. *Mass Spectrometry: Principles and Applications*; 3rd ed.; John Wiley & Sons Ltd: West Sussex, England, 2007,

5   Fenn, J. B.; Mann, M.; Meng, C. K.; Wong, S. F.; Whitehouse, C. M., "Electrospray Ionization for Mass Spectrometry of Large Biomolecules", *Science* **1989**, *246*, 64-71.

6   Tanaka, K.; Waki, H.; Ido, Y.; Akita, S.; Yoshida, Y.; Yoshida, T., "Protein and Polymer Analyses up to m/z 100 000 by Laser Ionization Time-of-flight Mass Spectrometry", *Rapid Communications in Mass Spectrometry* **1988**, *2*, 151-153.

7   Karas, M.; Hillenkamp, F., "Laser Desorption Ionization of Proteins with Molecular Masses Exceeding 10 000 Daltons", *Analytical Chemistry* **1988**, *60*, 2299-2301.

8   Wong, S. F.; Meng, C. K.; Fenn, J. B., "Multiple Charging in Electrospray Ionization of Poly(ethylene glycols)", *J. Phys. Chem.* **1988**, *92*, 546-550.

9   Mann, M.; Meng, C. k.; Fenn, J. B., "Interpreting Mass Spectra of Multiply Charged Ions", *Anal. Chem.* **1989**, *61*, 1702-1708.

10   Fenn, J. B.; Mann, M.; Meng, C. K.; Wong, S. F.; Whitehouse, C. M., "Electrospray Ionization-Principles and Practice", *Mass Spectrometry Reviews* **1990**, *9*, 37-70.

11   Fenn, J. B., "Ion Formation from Charged Droplets: Roles of Geometry, Energy, and Time", *J. Am. Soc. Mass Spectrom* **1993**, *4*, 524-535.

12   Fenn, J. B.; Rosell, J.; Meng, C. K., "In Electrospray Ionization, How Much Pull Does an Ion Need to Escape Its Droplet Prison?", *J. Am. Soc. Mass Spectrom* **1997**, *8*, 1147-1157.

13   Fenn, J. B., "Electrospray Wings for Molecular Elephants (Nobel Lecture)", *Angew. Chem. Int. Ed.* **2003**, *42*, 3871-3894.

14   Schiller, J.; Su¨ß, R.; Arnhold, J.; Fuchs, B.; Leßig, J.; ller, M. M.; Petkovic´, M.; Spalteholz, H.; rnig, O. Z.; Arnold, K., "Matrix-Assisted Desorption and Ionization Time-of-Flight (MALDI-TOF) Mass Spectrometry in Lipid and Phospholipid Research", *Progress in Lipid Research* **2004**, *43*, 449–488.

15   Caprioli, R. M.; Farmer, T. B.; Gile, J., "Molecular Imaging of Biological Samples: Localization of Peptides and Proteins Using MALDI-TOF MS", *Anal. Chem.* **1997**, *69*, 4751-4760.

16   Puolitaival, S. M.; Burnum, K. E.; Cornett, D. S.; Caprioli, R. M., "Solvent-Free Matrix Dry-Coating for MALDI Imaging of Phospholipids", *J Am Soc Mass Spectrom* **2008**, *19*, 882–886.

17   Groseclose, M. R.; Andersson, M.; Hardesty, W. M.; Caprioli, R. M., "Identification of Proteins Directly from Tissue: In Situ Tryptic Digestions Coupled with Imaging Mass Spectrometry", *J. Mass Spectrom.* **2007**, *42*, 254–262.

18   Seeley, E. H.; Caprioli, R. M., "Molecular Imaging of Proteins in Tissues by Mass Spectrometry", *PNAS* **2008**, *105*, 18126-18131.

19   Schwartz, S. A.; Reyzer, M. L.; Caprioli, R. M., "Direct Tissue Analysis Using Matrix-Assisted Laser Desorption/Ionization Mass Spectrometry: Practical Aspects of Sample Preparation", *J. Mass Spectrom.* **2003**, *38*, 699–708.

20   Aerni, H.-R.; Cornett, D. S.; Caprioli, R. M., "Automated Acoustic Matrix Deposition for MALDI Sample Preparation", *Anal. Chem.* **2006**, *78*, 827-834.

21   Hankin, J. A.; Barkley, R. M.; Murphy, R. C., "Sublimation as a Method of Matrix Application for Mass Spectrometric Imaging", *J Am Soc Mass Spectrom* **2007**, *18*, 1646–1652.

22   Reyzer, M. L.; Caprioli, R. M., "MALDI-MS-Based Imaging of Small Molecules and Proteins in Tissues", *Current Opinion in Chemical Biology* **2007**, *11*, 29–35.

23   Caprioli, R. M., "Perspectives on Imaging Mass Spectrometry in Biology and Medicine", *Proteomics* **2008**, *8*, 3679–3680.

CHAPTER VII

PATTERNED WELLS ON PDMS STAMP MADE BY LIQUID-POLYMER CASTING

7.1 Introduction

Microcontact printing is a technique that allows self-assembled monolayers (SAMs) to be patterned on a surface. The best developed and most extensively studied SAMs are alkanethiolates on gold surface. Long chain n-alkanethiols ($R(CH_2)_nSH$, R is the terminal group of the chain, the tail group) adsorb onto clean gold surfaces from solution and form densely packed and well-ordered monolayer films [1,2]. The surface properties, especially the surface wettability, can be tailored depending on the functionality of the tail group. For example, the adsorption of n-alkanethiols on gold generates hydrophobic surfaces with the lowest surface free energy (19 mJ/m^2) of any hydrocarbon surface; the contact angle of water on these SAMs with terminal methyl groups lies in the range 110-115°, comparing to 30-70° for the contact angle of water on bare gold surface [2].

A polydimethylsiloxane (PDMS) stamp is usually used for microcontact printing. The surface of the PDMS stamp has the desired pattern, which is cast from an appropriate relief structure ---- the master. The master is usually generated using

photolithography, and the photoresist pattern is developed on a silicon substrate. Although microcontact printing is routinely used for generating patterned SAMs on gold surface and experimentally the technique is very simple, preparing a PDMS stamp requires facility access to photolithography which may not be available to many labs.

In this work I describe an alternative method to prepare a PDMS stamp with patterned structure on the surface with no need of photolithography facilities. PDMS pre-polymers are immiscible in water, and when the polymers encapsulate patterned water on a surface and then solidify, the cavities occupied by water will form a certain microstructure, depending on the shape of the water droplets at the surface [3]. Micro-channels are the common structure that has been prepared using this method [3,4]. In this work I prepared a PDMS stamp with an array of recessed small hemispherical wells by liquid-polymer casting. The prepared stamp was further used for microcontact printing to pattern a gold surface and the surface was later used for patterning of organic crystals with possible application in imaging mass spectrometry.

7.2 Materials and methods

Materials. Trifluoroacetic acid (TFA) was purchased from Acros (Morris Plains, NJ). Diisopropylethylamine (DIEA), 2,5-dihydroxybenzoic acid (DHB) and betaine were purchased from Sigma-Aldrich (Milwaukee, WI). Sinapinic acid (SA) was purchased from VWR and recrystallized twice with 70% acetonitrile (by Junhai Yang). n-Hexadecanethiol (C16) was obtained from Fluka.

Substrate preparation. Three kinds of substrates were used in this work: hydroxyl

silane modified glass slide, octadecyltrichlorosilane modified silicon substrate and gold

surface.

The following describes the procedures for the preparation of hydroxyl silane

modified surfaces. Microscopic slides were cleaned in piranha solution (7:3(v/v),

concentrated H_2SO_4 : 30% H_2O_2. Caution: "piranha" solution reacts violently with

organic material and should be used with great care.) for 30 min, followed by rinsing

with copious quantities of deionized water and drying under a N_2 stream. The slides were

then immersed into a 1 wt.% N-(3-triethoxysilylpropyl)-4-hydroxy-butyramide (Gelest,

Morrisville, PA) solution in 95% ethanol for 16 hours to produce a hydroxyl silane

surface. The slides were removed from the silane solution, rinsed sequentially with

ethanol and water, and then blown dry with N_2. Then the slides were heated in an oven at

~110 °C for 30 min to anneal the films.

Self-assembled monolayers (SAMs) of octadecylsiloxane on Si/SiO$_2$ were

prepared as follows. Silicon substrates (~ 1 cm × 2 cm area) were cleaned in piranha

solution for 30 min, followed by rinsing with copious quantities of deionized water and

drying under a N_2 stream. The silicon substrates were immersed into 0.1% (v/v)

octadecyltrichlorosilane in anhydrous toluene for 20 hours. The slides were removed

from the silane solution, rinsed with toluene and deionized water, and then blown dry

with N_2.

The gold-coated silicon substrates were available in the lab from previous

studies. The gold surfaces were used after cleaning with ethanol and water.

Wetting measurements. Water contact angles were measured using a Ramé-Hart goniometer 100-01 S under ambient conditions. For the measurements of advancing and receding contact angles, the pipette tip was remained in the water drop. For the sessile contact angles, the pipette tip was not contacting the water drop, and the volume of the water drop applied was 2 µL. Contact angles were measured on both sides of the drop. At least three measurements were performed at different positions on the sample surface, and the data represent the average of them.

Fabrication of PDMS stamp. Spotting was performed using a microarray spotting station (MiraiBio Inc., South San Francisco, CA) with a single solid pin. The spotting solution was 50% betaine (trimethylglycine) in water. The sample surface with patterned liquid microdroplets was placed in a glass or plastic petri dish, and PDMS pre-polymers were poured over the patterned surface. The PDMS was made by a 10:1 ratio (w:w) mixture of SYLGARD silicone elastomer 184 and SYLGARD silicone elastomer 184 curing agent (Dow Corning Corporation). The PDMS was cured at 80 °C in an oven for one hour. Then the cured PDMS was peeled off the slide surface, and the left betaine on the PDMS surface was rinsed off by deionized water.

Microcontact printing. With the PDMS stamp, microcontact printing was applied to pattern a gold surface [5]. The stamp surface was "inked" with 2 mM hexadecanethiol ($CH_3(CH_2)_{15}SH$) in ethanol solution using a cotton swab, and brought in contact with a gold surface for ~ 20 s. The gold surface was rinsed with ethanol, and dried under a stream of nitrogen.

Matrix solutions. SA-DIEA ionic matrix was prepared at 0.75 mM by mixing equimolar amounts of sinapinic acid and DIEA in 50:50 acetonitrile/0.1% TFA in DI H_2O. DHB-

DIEA ionic matrix was prepared at 0.75 mM by mixing equimolar amounts of DHB and DIEA in 50:50 acetonitrile/0.1% TFA in DI H_2O. DHB matrix solution was prepared at 20 mg/mL by dissolving DHB in 50:50 acetonitrile/0.1% TFA in deionized H_2O.

7.3 Results and discussion

The procedure to prepare PDMS stamp by liquid-polymer casting. Figure 7.1 depicts the procedure for preparing a PDMS stamp with patterned wells on the surface using a liquid-polymer casting method. The substrate surfaces used here include both hydroxyl surface and gold surface. Water advancing (receding) contact angles on the hydroxyl and gold surface are 53° ± 1° (26° ± 1°) and 68° ± 1° (22° ± 1°), respectively. Nano-liter liquid droplets were placed on the substrate surface in an array format by a robotic spotter. The spotting solution was 50% betaine (trimethylglycine) in water. Betaine is a zwitterionic and hygroscopic substance that helps minimize the evaporation of each droplet. The shape of each droplet on the surface is determined by the surface energy of the substrate and the surface tension of the liquid. The slide with the liquid droplet array is then used as a master to make a PDMS relief structure by pouring PDMS pre-polymers over the patterned surface. Since PDMS is not miscible with water, each water droplet remains at its location at the substrate surface and is surrounded by the PDMS. After the curing step, the PDMS surface forms patterned wells due to the cavities occupied by the liquid droplets. Such surface with recessed hemispherical wells can be used as a stamp to pattern a surface by microcontact printing (Figure 7.1).

164
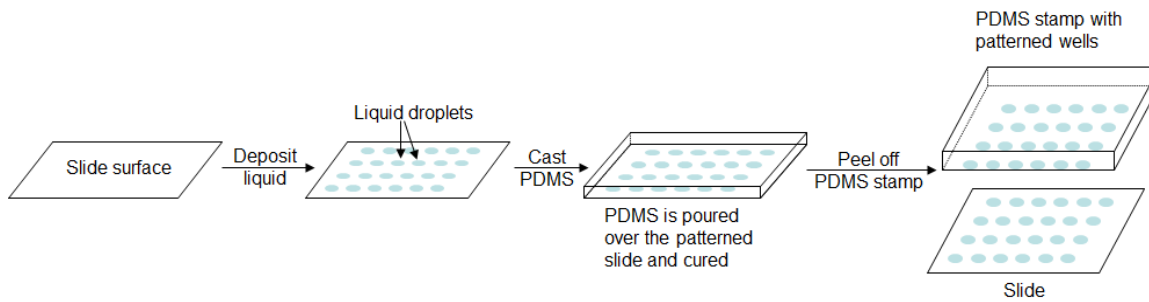
Figure 7.1. Scheme illustrating the process for making a PDMS stamp with patterned wells using a microarray spotter.

Patterned wells. Figure 7.2 shows the optical images of PDMS surfaces with patterned wells prepared using liquid-polymer casting on a hydroxyl surface (Figure 7.2(A)) and on a gold surface (Figure 7.2(B)). The wells are 175~200 μm in diameter, and their center-to-center distance is 400 μm. The size of the wells is related to the size of the liquid droplets formed during the spotting process. The wells were prepared using a either a 70 μm or a 150 μm printing pin. It is possible to generate smaller wells if a smaller printing pin is used, and thus to increase the density of the features, too. In addition, other spotting method is also possible to deposit tiny droplets of liquid onto a surface, such as using an acoustic spotter [6]. If bigger spot sizes are desired, one can simply hand spot solution to the surface.

To investigate the curvature of the wells, a blade was used to cut the wells and the images of the cross sections of one well from each stamp are shown as the insets in Figure 7.2. From the inset of Figure 7.2(A), the angle between the tangential line of the well's curvature at the interface and the PDMS surface is about 45° for the stamp casted from the hydroxyl surface, comparing to 20° for the stamp casted from the gold surface (Figure 7.2(B)). For the hydroxyl surface, the obtained well's angle is smaller than the advancing water contact angle of hydroxyl surface (53° ± 1°), and close to the sessil contact angle of 2 μL water on hydroxyl surface (49 ± 1°). For the gold surface, the well's angle is close to the receding water contact angle on the gold surface (22 ± 5°). The reason for the formation of different well curvatures is not clear. One possible reason is that the gold surface on a silicon substrate is more conductive than a hydroxyl surface on a glass substrate and there was crystallization from the liquid droplets on the

166

gold surface during the PDMS curing step, as indicated by the rougher well surface in Figure 7.2(B).

Different well curvatures can be obtained by using surfaces with different functional groups (i.e. different surface energies) since the curvature of the wells is a negative copy of the shape of the liquid droplets at the substrate surface. Such surfaces include gold surface, hydroxyl surface, methyl surface (such as SAMs of octadecylsiloxane), etc. Figure 7.3 shows two cross-section images of two recessed wells prepared on both the gold surface (Figure 7.3 (A)) and the octadecylsiloxane surface (Figure 7.3 (B)). The liquid (0.1~0.3 μL) was hand pipetted to the surface. By casting on the gold surface, the well's curvature from the gold surface has a 60° angle, which is close to the water advancing contact angle on gold surface (68° ± 1°). For the 0.1 μL liquid volume used here, no crystallization of betaine was observed in the drop. While on the octadecylsiloxane surface, the angle is ~ 160°, which is much higher than the water advancing contact angle on a methyl surface (110° ± 1°). The reason to have such a higher contact angle on the octadecylsiloxane surface is explained next.

The interfacial tensions determine the contact angle of a drop on a surface as indicated by Young's equation [7]. Figure 7.3(C) shows the wetting situations for a drop on an octadecylsiloxane surface before and after the surface and the drop are covered by the PDMS pre-polymers. The figure also shows the related Young's equations. The values for the interfacial tensions are $\gamma_{SV\ (OTS,air)} = \gamma^d_{SV\ (OTS,air)} = 21.8$ mN/m [8], $\gamma_{L2V(PDMS,air)}$ = 18.2 mN/m (dispersive or van der Waals contribution: 15.6 mN/m, and polar contribution: 2.6 mN/m) [9], and $\gamma_{L1V(water,air)} = 72.8$ mN/m (dispersive contribution: 21.8 mN/m, and polar contribution: 51 mN/m) [9]. Here S is the octadecylsiloxane surface, V is

air, L1 is water, and L2 is PDMS. γ_{SL2} and γ_{L1L2} are calculated using the following equation [7]

$$\gamma_{12} \approx \gamma_1 + \gamma_2 - 2\sqrt{\gamma_1^d \gamma_2^d} - 2\sqrt{\gamma_1^p \gamma_2^p} ,\tag{7.1}$$

where the superscripts "d" and "p" indicate dispersive and polar interactions. Thus we obtain $\gamma_{SL2(OTS,PDMS)} \approx 3.1$ mN/m, and $\gamma_{L1L2(water, PDMS)} \approx 31.1$ mN/m. To consider the wetting situations using the Young's equation, we have

$$\text{in air, } \cos\theta_{\text{in air}} = \frac{\gamma_{SV} - \gamma_{SL1}}{\gamma_{L1V}} ,\tag{7.2}$$

$$\text{and in PDMS, } \cos\theta_{\text{in PDMS}} = \frac{\gamma_{SL2} - \gamma_{SL1}}{\gamma_{L1L2}} .\tag{7.3}$$

Since $\gamma_{L1L2(water, PDMS)} < \gamma_{L1V(water,air)}$, $\gamma_{SL2(OTS,PDMS)} < \gamma_{SV (OTS,air)}$, and the values on the right sides of eqs (7.2) and (7.3) are negative as both contact angles are greater than 90°, we know that $\cos\theta_{\text{in PDMS}}$ is more negative than $\cos\theta_{\text{in air}}$, thus the contact angle in PDMS $\theta_{\text{in PDMS}}$ is greater than that in air $\theta_{\text{in air}}$. This result is consistent with the experimental observations.

Thousands of wells can be patterned on a PDMS surface. Shown in Figure 7.4 is a PDMS stamp prepared by liquid-polymer casting on a gold surface. About 3500 wells were formed on the 11 mm × 7 mm surface. Each well is about 120 μm in diameter, and the well center-to-center distance is about 150 μm.

A
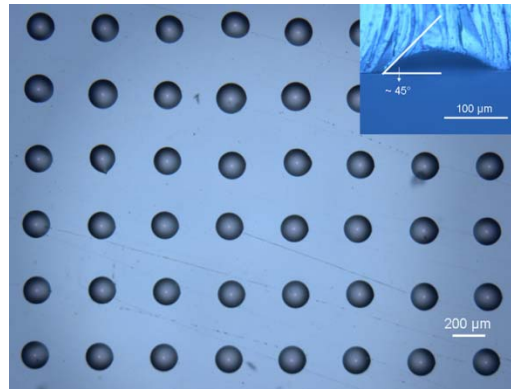
B
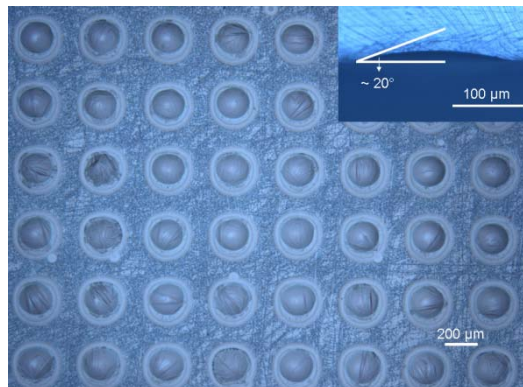
Figure 7.2. Optical photographs of the patterned recessed wells on PDMS stamp surfaces. (A) stamp surface casted from a hydroxyl surface. The wells are ~ 175 μm in diameter, and their center-to-center distance is 400 μm. The master was generated by spotting 50% aqueous betaine onto a glass slide surface derivatized with hydroxyl groups. The spotting was performed at room temperature and the relative humidity inside the spotter was 46~50%. The inset is a cross-section image showing the well has a contact angle around 45° with the PDMS surface; (B) stamp surface casted from a gold surface. Wells are around 200 μm in diameter, and the well center-to-center distance is 400 μm. The master was generated by spotting 50% aqueous betaine onto a bare gold surface. The spotting was performed at room temperature and the relative humidity inside the spotter was 45%. The inset is a cross section image of one well showing the contact angle around 20° with the PDMS surface.

A

60°

0.5 mm

B

160°

0.5 mm

C

Air

γ_{L1V}

γ_{SV} θ γ_{SL1}

$$\cos\theta_{\text{in air}} = \frac{\gamma_{SV} - \gamma_{SL1}}{\gamma_{L1V}}$$

PDMS pre-polymers

γ_{L1L2}

γ_{SL2} θ γ_{SL1}

$$\cos\theta_{\text{in PDMS}} = \frac{\gamma_{SL2} - \gamma_{SL1}}{\gamma_{L1L2}}$$

L1: water
L2: PDMS pre-polymers
V: air
S: octadecylsiloxane surface
$\theta_{\text{in air}}$, $\theta_{\text{in PDMS}}$: water contact angles in air and in PDMS
$\gamma_{SL1}, \gamma_{SV}, \gamma_{L1V}, \gamma_{SL2}, \gamma_{L1L2}$: interfacial tensions
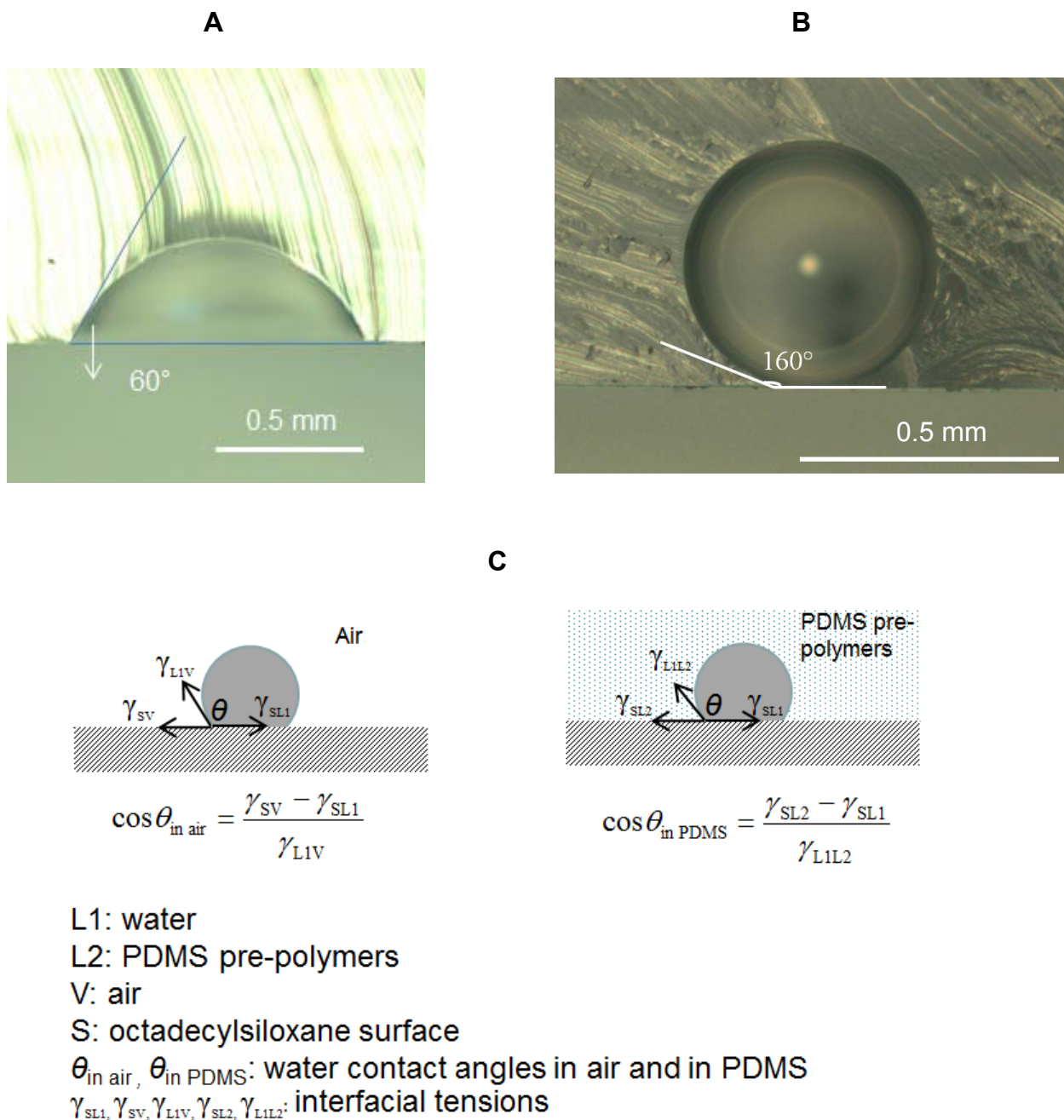
Figure 7.3. cross-section images of recessed wells on PDMS stamp surfaces (A) prepared by hand pipetting 0.1 μL 50% betaine aqueous solution onto a gold surface and casting it with PDMS pre-polymers; (B) prepared by hand pipetting 0.2~0.3 μL 50% betaine aqueous solution onto an octadecylsiloxane surface and casting it with PDMS pre-polymers. More betaine solution was pipetted on the methyl surface because it was difficult to pipette small amount of liquid (0.1 μL) to the low energy methyl surface; (C) The wetting situations of a drop on an octadecylsiloxane surface in air (left), and with PDMS pre-polymers covering the surface and the drop (right).

170
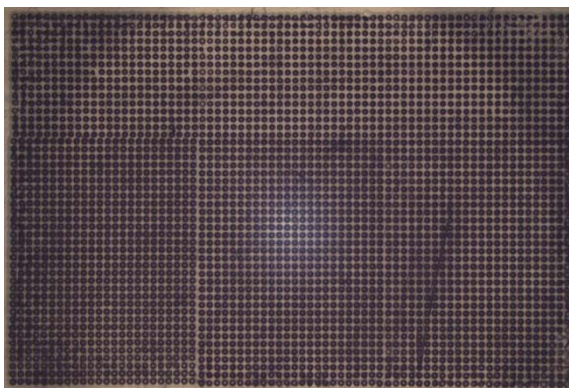
Figure 7.4. Optical photograph of a PDMS stamp with ~ 3500 wells on the surface. Each well is about 120 μm in diameter, and the well center-to-center distance is about 150 μm.

**Applications using the PDMS stamp with patterned wells.** In this section, I show a few applications using the PDMS stamp with pattern wells.

The first application is to use the stamp itself to load solution into the each well and transfer them to a surface. For applications of imaging mass spectrometry, we want the matrix solution to be patterned on a thin tissue section (see Chapter VI). Commonly matrices are dissolved in volatile solvents such as acetonitrile and water. Such matrix solutions evaporate fast and could not be used for the printing in atmosphere. For this demonstration, ionic matrix, such as a mixture of sinapic acid (SA) with N,N-diisopropylethyl amine (DIEA) was chosen since the solution is nonvolatile and does not evaporate during the printing process in atmosphere. By simply dipping the PDMS stamp surface in the ionic matrix solution and emerging it, each well on the stamp surface is loaded with a tiny amount of solution, as shown in Figure 7.5(A) with a magnified view in Figure 7.5(B). The volume of each droplet in each well is believed to be in the order of or less than 2 nL, which is the amount of the droplet used to manufacture the stamp. It shows that the well is not fully covered by the matrix solution. Both unwashed and ethanol washed thin tissue section were used as the substrate onto which the prepared stamp with loaded matrix in each well was directly printed to transfer the material. Shown in Figure 7.5(C) and (D) are the optical images of the tissue surfaces. It showed that the matrix was patterned on both surfaces with a new moon shape, however, the matrix in each well was not 100% transferred during the printing process. This method was not further investigated as it is challenging to transfer the liquid in each well fully or equally to the tissue surface.
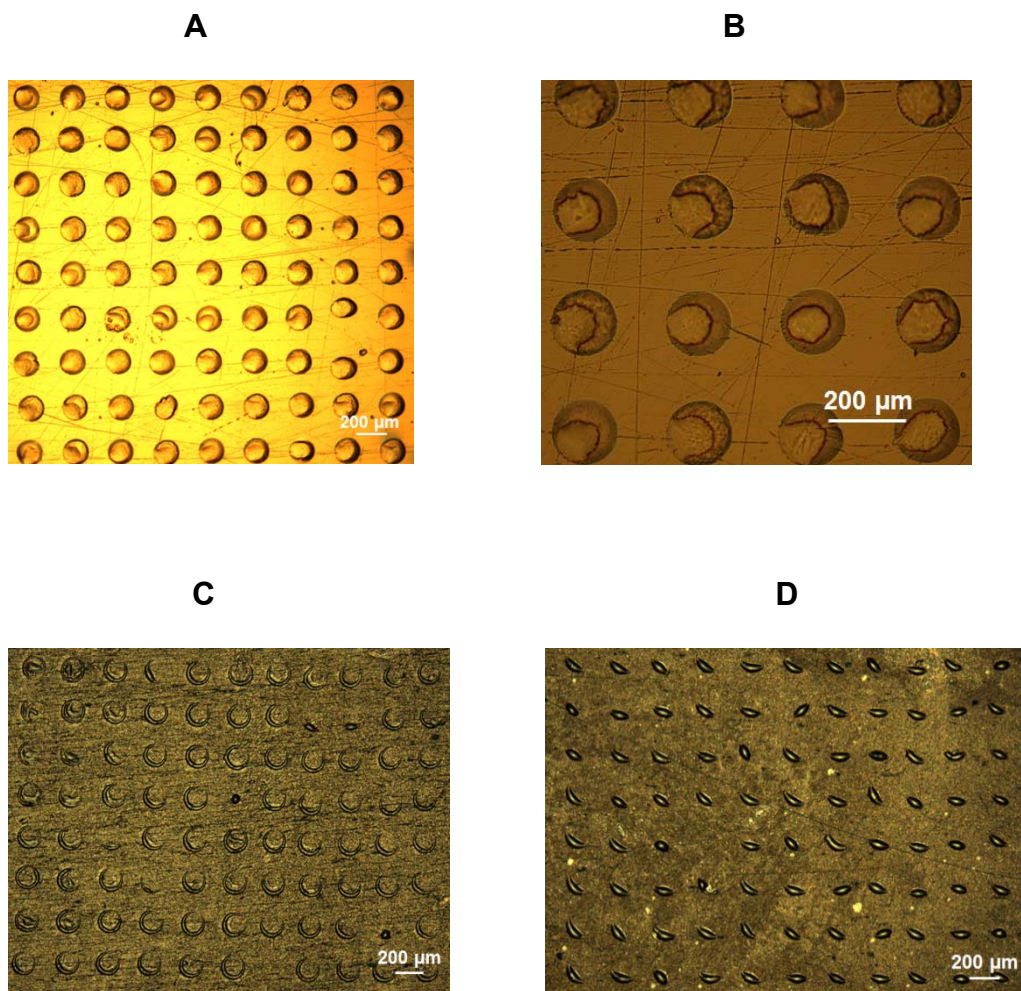
Figure 7.5. Optical photographs. (A) a PDMS surface with each patterned well locating a tiny amount of liquid of nonvolatile SA-DIEA mixture (SA = sinapinic acid and DIEA = N,N-diisopropylethyl amine); (B) a magnified view of the surface in (A); (C) a unwashed tissue section surface covered with an array of SA-DIEA spots directly printed with a surface like (A); (D) an ethanol washed tissue section surface covered with an array of SA-DIEA directly printed with a surface like (A).

Other applications using the PDMS stamp with patterned wells on the surface include patterning gold surfaces by microcontact printing. Microcontact printing is to use an elastomeric PDMS stamp to form patterned self-assembled monolayers (SAMs) on a surface [5]. As illustrated in Figure 7.6, by simply "inking" the stamp surface with hexadecanethiol in ethanol solution using a cotton swab, and bringing the stamp to contact with a gold surface, the gold surface contacting with PDMS stamp becomes hydrophobic due to the transfer and rapid reaction of alkanethiol with gold and the formation of the SAM with methyl groups. The non-contacting regions, corresponding to the recessed wells on the PDMS stamp, remain as intact gold surface and less hydrophobic the methyl SAM.

Patterned SAMs on a metal substrate provide a template for arraying inorganic [10] or organic crystals [11] at a surface. Here I show the use of the patterned gold surface for forming an array of DHB (2,5-dihydroxybenzoic acid) matrix liquid droplets or matrix crystals. DHB is a commonly used substance for matrix-assisted laser desorption ionization (MALDI) experiments [12]. As illustrated in Figure 7.6, the final patterned gold surface has a continuous hydrophobic region with patterned and less hydrophobic circular spots. When the surface is immersed and wetted with polar solutions, and after emersion of the surface, the liquid retreats from the surface leaving behind microdroplets of solution in the hydrophilic patches on the substrate surface. Figure 7.7(A) shows a gold surface patterned with nonvolatile DHB-DIEA matrix droplets. When the matrix solution was dissolved in a volatile solvent, the liquid droplets evaporated in a few seconds in atmosphere and formed the DHB crystals on those hydrophilic spots, as shown in Figure 7.7(B).
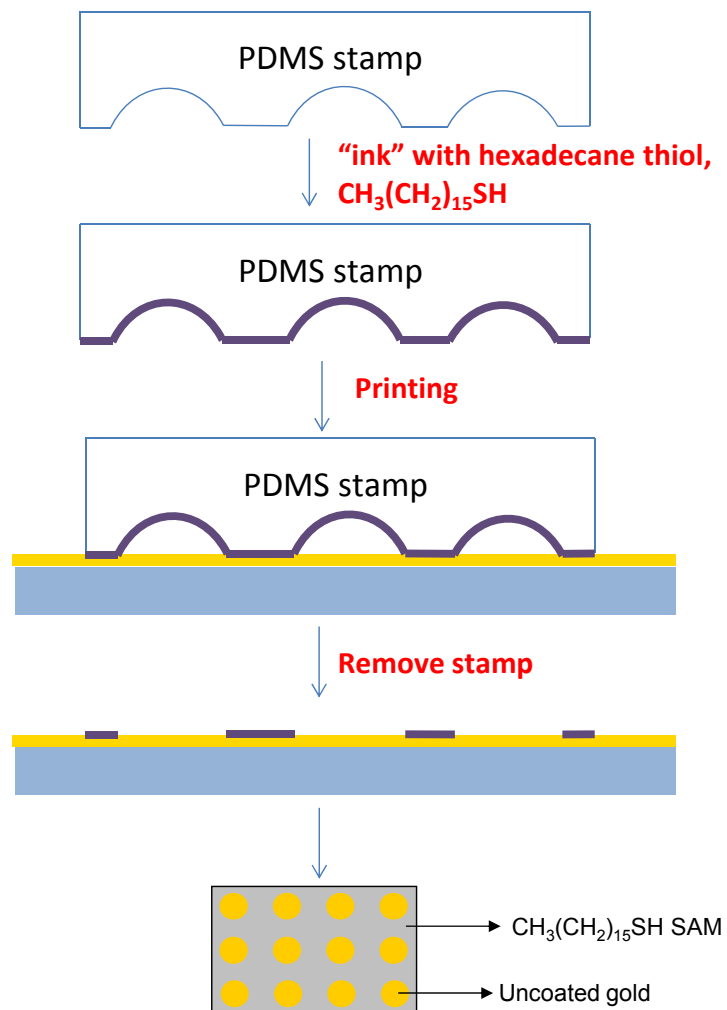
Figure 7.6. Schematic illustration of the procedure to prepare a patterned gold surface by microcontact printing using the PDMS stamp with patterned wells.

A
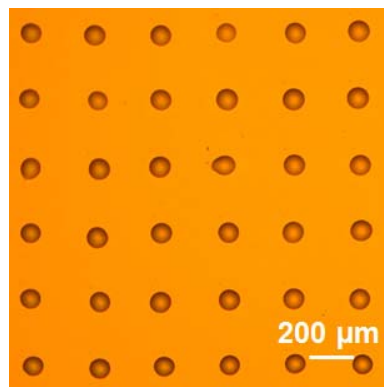
B
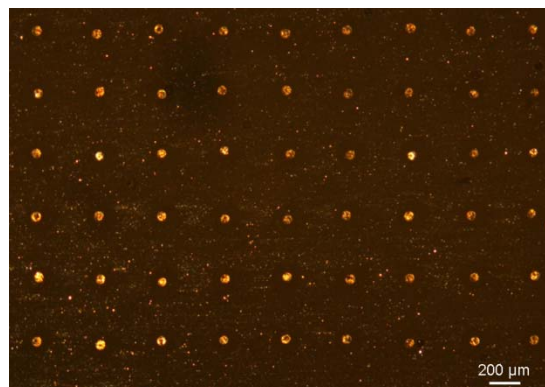
Figure 7.7. Optical photographs of (A) an array of DHB-DIEA (DHB = 2,5-dihydroxybenzoic acid; DIEA = N,N-diisopropylethyl amine) ionic matrix droplets formed by dip-coating, and (B) an array of DHB matrix crystals formed by dip-coating.

7.4 Conclusions

Liquid-polymer casting was used to prepare polydimethylsiloxane (PDMS) stamps. The formed stamps have patterned recessed wells with the size of 100 ~ 150 μm on the surface. Substrate surface affects the well's curvature during the casting. The stamps were used to directly print ionic matrix solution to tissue section surfaces. They were also used to pattern gold surfaces by microcontact printing. The patterned gold surface allows the array formation of either ionic matrix droplets or matrix crystals by selective dewetting. Such patterned matrix arrays have possible applications in MALDI imaging mass spectrometry (see Chapter VIII).

References

1   Porter, M. D.; Bright, T. B.; Allara, D. L.; Chidsey, C. E. D., "Spontaneously Organized Molecular Assemblies. 4. Structural Characterization of n-Alkyl Thiol Monolayers on Gold by Optical Ellipsometry, Infrared Spectroscopy, and Electrochemistry", *J. Am. Chem. Soc.* **1987**, *109*, 3559-3568.

2   Bain, C. D.; Troughton, E. B.; Tao, Y.-T.; Evall, J.; Whitesides, G. M.; Nuzzo, R. G., "Formation of Monolayer Films by the Spontaneous Assembly of Organic Thiols from Solution onto Gold", *J. Am. Chem. Soc.* **1989**, *111*, 321-335.

3   Chao, S.-h.; Carlson, R.; Meldrum, D. R., "Rapid Fabrication of Microchannels Using Microscale Plasma Activated Templating (µPLAT) Generated Water Molds", *Lab Chip* **2007**, *7*, 641-643.

4   Liu, X.; Wang, Q.; Qin, J.; Lin, B., "A Facile "Liquid-Molding" Method to Fabricate PDMS Microdevices with 3-Dimensional Channel Topography", *Lab Chip* **2009**, *9*, 1200-1205.

5   Xia, Y.; Whitesides, G. M., "Soft Lithography", *Angew. Chem. Int. Ed. Engl.* **1998**, *37*, 550-575.

6   Aerni, H.-R.; Cornett, D. S.; Caprioli, R. M., "Automated Acoustic Matrix Deposition for MALDI Sample Preparation", *Anal. Chem.* **2006**, *78*, 827-834.

7   Butt, H.-J.; Graf, K.; Kappl, M. *Physics and Chemistry of Interfaces*; Second, Revised and Enlarged ed.; Wiley-VCH: KGaA, Weinheim, 2006, 128-140.

8   Hurst, K. M.; Roberts, C. B.; Ashurst, W. R., "Characterization of Gas-Expanded Liquid-Deposited Gold Nanoparticle Films on Substrates of Varying Surface Energy", *Langmuir* **2011**, *27*, 651-655.

9   Comyn, J., "Contact Angles and Adhesive Bonding", *Int. J. Adhesion and Adhesives* **1992**, *12*, 145-149.

10   Aizenberg, J.; Black, A. J.; Whitesides, G. M., "Control of Crystal Nucleation by Patterned Self-Assembled Monolayers", *Nature* **1999**, *398*, 495-498.

11   Kim, K.; Lee, I. s.; Centrone, A.; Hatton, T. A.; Myerson, A. S., "Formation of Nanosized Organic Molecular Crystals on Engineered Surfaces", *J. Am. Chem. Soc.* **2009**, *131*, 18212–18213.

12   Hankin, J. A.; Barkley, R. M.; Murphy, R. C., "Sublimation as a Method of Matrix Application for Mass Spectrometric Imaging", *J Am Soc Mass Spectrom* **2007**, *18*, 1646–1652.

CHAPTER VIII

PRE-COATED MATRIX CRYSTAL ARRAYS FOR IMAGING MASS SPECTROMETRY

8.1 Introduction

Over the past decade, MALDI (matrix-assisted laser desorption/ionization) imaging mass spectrometry [1] has emerged as an extraordinarily powerful technology to examine the relative abundance and spatial distribution of lipids [2], peptides and proteins [3,4] across a thin tissue section. The application of imaging mass spectrometry and the new knowledge that it can generate will have a tremendous impact on biological and clinical sciences [5]. Images from diseased tissues yielding the distributions and concentrations for proteins and other species that may be specific to the onset and/or presence of a disease may be highly useful in providing patient prognosis.

In an imaging mass spectrometry (IMS) experiment, sample preparation is critical for obtaining high quality mass spectrometry signals [6]. Typically, a thin tissue section is prepared in a cryostat, and consequently mounted on a MALDI plate, and then matrix is deposited onto the tissue surface using a low volume pipette or an automatic acoustic matrix spotter [7], or the tissue surface is coated with matrix crystals by sublimation [8]. By moving the MALDI plate in its x and y directions, a collection of individual mass spectrometry spectra can be obtained from discrete locations across the

sample in a defined laser raster pattern. Each spectrum may contain hundreds of mass spectral peaks that represent the composition of each particular spot on the tissue surface. From these individual spectra, intensity maps for selected ions of interest are created across the sample to produce images that illustrate the spatial distribution and relative abundance of those ions across the tissue surface.

In the preparation of a sample for imaging mass spectrometry, the most important step is locating the matrix on the tissue surface. To achieve ion images at high resolution, it is critical to present the matrix in spots that are small and in a density as high as possible, with the condition that the same high quality of signal be achieved by the amount of matrix on each spot. To achieve this goal, acoustic spotting has been routinely used in various laboratories for preparing tissue samples for imaging mass spectrometry [7]; however, this spotting method has a few shortcomings. First, the smallest spot size presently possible by these instruments is ~250 μm in diameter and this feature size limits this method for achieving higher resolution images. Second, acoustic spotters that can produce small spots of this size are expensive and often not available in many labs. Third, acoustic spotting process is very time-consuming as it sequentially applies the matrix onto the tissue surface as individually deposited spots. For example, it presently takes many hours for current acoustic spotters to deposit the matrix compounds as individual droplets onto a tissue section that is just 1 cm^2 in area with center-to-center distances between spots of 300 μm. The reliance on acoustic spotting for sample preparation limits abilities for higher resolutions, both in terms of achieving much smaller spot sizes as well the longer spotting times that will be required for spotting smaller spots with decreasing center-to-center distances between spots.

This work describes a "pre-coating" method that can produce matrix spots in sizes much smaller than achievable by an acoustic spotter or other drop-on-demand systems. A goal was to achieve matrix spot sizes on a surface with diameter <100 μm by sample preparation methods that could also shorten sample preparation times. Specifically, the required many hours of processing using an acoustic spotter were targeted to be reduced to a few minutes by a pre-coating method. The approach that I pursued avoided using an expensive spotting procedures to prepare the sample for imaging mass spectrometry, thus having the potential for broad use if successful. The pre-coating method applied microcontact printing methods to pattern a gold surface, using an elastomeric polydimethylsiloxane (PDMS) stamp that is cast against an appropriate relief structures present in a master. These masters are prepared by a liquid droplet/polymer casting method that is described in Chapter VII or by photolithography.

Microcontact printing has been used to pattern self-assembled monolayers (SAMs) on a surface. The best developed and most extensively studied SAMs are those formed by the adsorption of alkanethiolate monolayers onto gold surfaces. For long chain n-alkanethiols, these molecules adsorb onto clean gold surfaces from solution and form densely packed, well-ordered monolayer films [9,10]. The properties of the surface are modified by the formation of these films, and features such as the surface wettability can be tailored depending on the tail group functionality of the adsorbing alkanethiol.

In this work, the patterned gold surface was used to direct the deposition of matrix compounds such as sinapinic acid (SA) and 2,5-dihydroxybenzoic acid (DHB) regioselectively, as an array on the surface. These compounds have shown broad usefulness in MALDI for obtaining mass spectral data for lipids, whole proteins, and

other often high molecular weight species. After formation of the patterned matrix array,
a tissue section is applied onto the surface to allow interactions between the matrix
crystals and the analytes in the tissue section to take place as needed for obtaining
MALDI spectra. The resulting method that was developed offers great simplification and
time savings over present methods, with the further benefit of allowing imaging mass
spectrometry to be performed at much higher resolutions.

8.2 Materials and methods

Materials. Trifluoroacetic acid (TFA) was purchased from Acros (Morris Plains, NJ).
Chloroform, diisopropylethylamine (DIEA), and 2,5-dihydroxybenzoic acid (DHB) were
purchased from Sigma-Aldrich (Milwaukee, WI). Sinapinic acid (SA) was purchased
from VWR and recrystallized twice with 70% acetonitrile (by Dr. Junhai Yang). Mouse
brains and rat brains were purchased from Pel-Freez Biologicals (AZ). Gold-coated glass
slides were obtained from Deposition Research Lab Inc. (St. Charles, MO). The PDMS
SYLGARD silicone elastomer 184 and SYLGARD silicone elastomer 184 curing agent
were purchased from Dow Corning Corporation (Midland, MI).

Microcontact printing. PDMS stamps were prepared by casting a prepolymer of PDMS
against a printed liquid droplet array as described in Chapter VII. These stamps
contained a relief structure with circular openings on their surfaces. Gold surfaces were
rinsed with ethanol and water, and blown dry under a stream of N_2 before use. The
surface of the PDMS stamp was "inked" with a 2 mM hexadecanethiol ($CH_3(CH_2)_{15}SH$)

solution in ethanol using a cotton swab, and brought into contact with a gold surface for ~ 20 s. After removal of the stamp, the patterned gold surface was rinsed with ethanol, and dried under a stream of nitrogen.

Formation of matrix crystal array by selective dewetting. Patterned gold surfaces were immersed into DHB or SA matrix solutions at various concentrations. The matrices were dissolved in solution formed from equal volumes of acetonitrile and 0.1% TFA in deionized water. After emersion of a sample from a matrix solution, microdroplets of the matrix solution formed on the gold surface. The sample was either left to dry in the atmosphere, or immediately transferred into a humidity chamber to maintain the matrix as liquid droplets on the slide surface.

Formation of matrix crystal array by selective deposition. Patterned gold surfaces were used to direct the self-organization of matrix crystals from solution. Matrix solutions were prepared to contain 10-20 mg/mL sinapinic acid in 1:1 Carnoy's fluid/water, with Carnoy's fluid consisting of ethanol:chloroform:acetic acid in a volumetric ratio of 6:3:1. The resulting matrix solution phase separated into two layers, and the upper layer (i.e., the water phase) was collected and 1-400 µL of this solution was pipetted onto a slide to cover the patterned gold surface. The solvent was allowed to evaporate, forming matrix crystals that grew preferentially on the hydrophilic circular spots. Continuous deposition of the matrix compound occurred as additional solvent evaporates. During the deposition, the solvent did not retreat from the substrate surface, and the patterned matrix arrays formed in a few minutes. The procedure stopped by removing the solution from the slide by pipette or contact with a Kimwipes tissue, and the surface was left to dry in the atmosphere.

185

Preparation of tissue sections. Tissue sections were prepared using a Leica CM3050 cryostat (Leica Microsystems GmbH, Wetzlar, Germany), and thaw-mounted onto the patterned matrix surface. The slide was transferred into a Corning humidity chamber, and 200 µL water and 40-200 µL methanol were pipetted inside the chamber in a region next to the sample. This procedure allowed the sample surface to be exposed to a mixture of methanol/water vapors. The chamber was placed in an oven at 90 °C for 4-10 minutes to enhance analyte extraction from the tissue and into the matrix crystals.

MALDI imaging mass spectrometry. After the vapor rehydration/extraction step, the samples were loaded into a Bruker UltrafleXtreme MALDI-TOF/TOF mass spectrometer (Bruker Daltonics, Billerica, MA) and MALDI imaging was performed. Lipid images were prepared using the FlexImaging 2.1 software (Bruker Daltonics), and spectra were generated using FlexAnalysis 3.3 software (Bruker Daltonics).

8.3 Results and discussion

Pre-coating a surface for imaging mass spectrometry. Figure 8.1 depicts the procedure to prepare a pre-coated matrix crystal array for imaging mass spectrometry. A microarray featured surface was constructed by microcontact printing a gold coated glass slide with a polydimethylsiloxane (PDMS) stamp hosting an array of microwells (diameter ranges from 1 to 500 µm) "inked" with n-hexadecanethiol ($CH_3(CH_2)_{15}SH$). The microcontact printing process forms a gold surface that exposes a microarray of hydrophilic areas (i.e., uncoated gold surface) that are surrounded by a continuous

hydrophobic surface (i.e., the self-assembled hexadecanethiol monolayer). The PDMS stamp was prepared using liquid-polymer casting as discussed in Chapter VII. The gold surface with the hydrophilic microarray was used to direct the assembly of matrix crystals onto the slide, and the matrix crystal arrays could be prepared by either a selective dewetting method (Chapter VII) or a pipetting-evaporation method (this work). The pipetting-evaporation method was developed in this work as a way to overcome the limitations of the selective dewetting method in that each spot could be exposed to a greater matrix amounts and could produce thicker matrix deposits on each spot. After the matrix crystal array formed, a tissue section was applied on top of the matrix array. The sample was exposed to the solvent vapors (methanol, water, and/or any other chemicals), allowing the extraction and interaction between the tissue and the matrix crystals. After the extraction, the sample was ready for imaging mass spectrometry experiments.
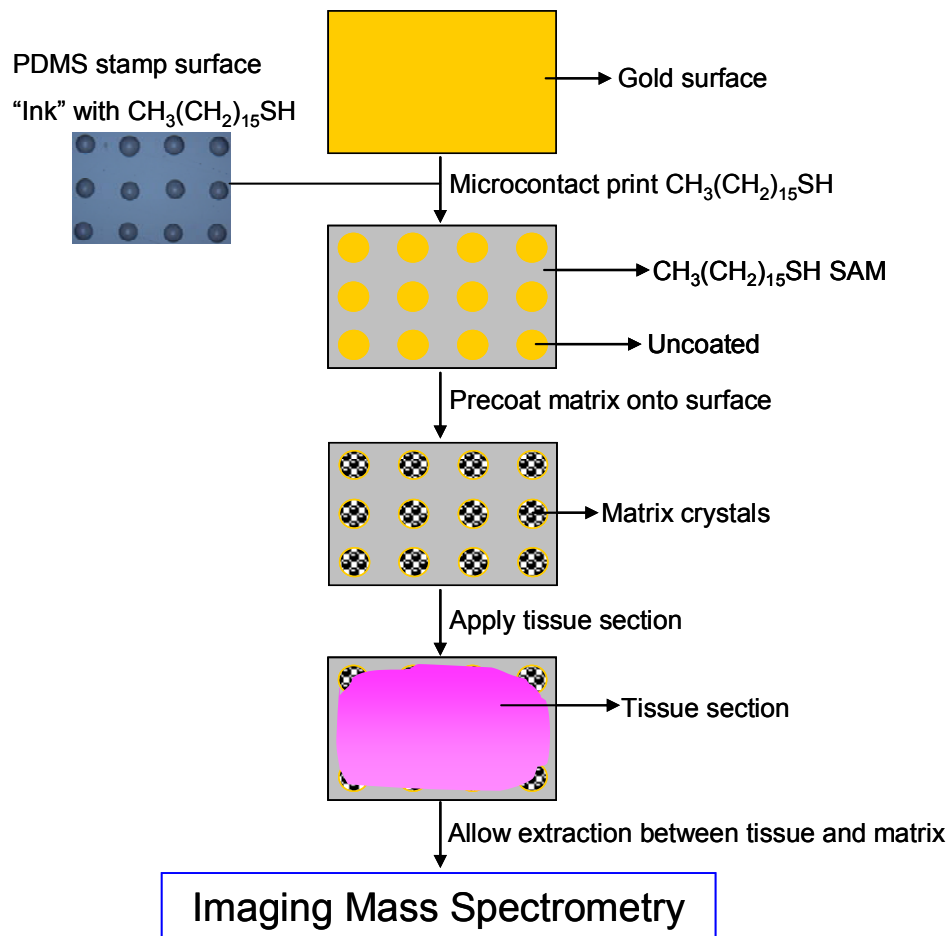
Figure 8.1. Schematic presentation of the experimental steps for IMS using a pre-coated patterned matrix array surface.

Matrix crystal array formed by selective dewetting. As showed in Figure 7.7 of

Chapter VII, matrix crystals can be formed as an array by a selective dewetting process.

In that process, the surface is immersed in a polar solution of the matrix, and after its

emersion from the solution, the liquid retreats from the surface leaving behind

microdroplets of the matrix solution in the hydrophilic spots. Matrix crystals form in

these areas as the solvent evaporates. This selective dewetting method requires only a

few seconds to form matrix arrays on the surface. Figure 8.2(A) shows a patterned DHB

crystal array that was formed by is the selective dewetting process from a DHB matrix

solution at a concentration of 20 mg/mL.

For imaging mass spectrometry, greater amounts of the matrix crystals on each

spot may be required to achieve the necessary enhancement for the interactions between

the analytes in the tissue sections and the matrix compound. If more matrix material is

desired on each spot in a selective dewetting process, the easiest way to achieve this goal

can be to increase the matrix concentration in the dipping solution. Figure 8.2(B) shows

a DHB crystal array that was formed by this process using ~260 mg/mL matrix solution.

At these higher matrix concentrations, the spots tend to form irregular shapes, in

comparison to the consistent circular spots in Figure 8.2(A) formed at lower

concentrations. Alternatively, to further increase the matrix amount deposited on each

spot, the surface could be placed into a saturated DHB matrix solution and selectively

dewetted multiple times as a way to yield thicker crystal films. Although additional

matrix crystal deposition was observed by this multiple dewetting process, it did not

proceed with a high level of repeatability since some of the deposited crystals would

wash off during the consequent immersion dewetting steps. As a result, this method was not further investigated.

In the above process, it is the difference in wettability on the patterned gold surfaces that defines the discrete locations for matrix deposition by selective dewetting. When a non-patterned gold surface is immersed and removed from the DHB matrix solution, DHB crystals instead grow randomly on the surface, as shown in Figure 8.3(C).

To estimate the amount of matrix that may form on each spot in a single dewetting step, I assumed that each liquid droplet forms a hemispherical cap on each of the hydrophilic sites on the gold surface. Note that the diameter of the hydrophilic spot is determined by the feature size on the PDMS stamp and is usually larger than the final formed matrix spot size probably due to solvent evaporation. The droplet forms a contact angle θ on the surface. The volume of the spherical cap can be calculated using the following equation [11]:

$$V_{cap} = \frac{1}{6}\pi h\left(3a^2 + h^2\right),\tag{8.1}$$

where h is the height of the cap and a is the radius of the spot, as shown in Figure 8.3. Using eq (8.1), the drop volume for each spot in Figure 8.2(A) is 0.14 nL ($a = 80$ μm, $h = 14$ μm, $\theta = 20°$), and that for each spot in Figure 8.2(B) is 0.06 nL ($a = 60$ μm, $h = 11$ μm, $\theta = 20°$). For the employed the matrix concentrations, the amount of DHB on each spot in Figure 8.2(A) is 2.8×10^{-6} mg, and that in Figure 8.2(B) is 16×10^{-6} mg. For a typical acoustic spotting process where the matrix concentration is 20 mg/mL, and 30 drops each of 0.17 nL are sequentially deposited onto a common spot with a size of 250 μm, these spots contain has 100×10^{-6} mg of matrix compound.

Another commonly used matrix, sinapinic acid, can also be patterned by the selective dewetting method. This matrix compound is frequently used for the detection of protein signals in MALDI experiments. One problem faced in generation useful arrays of sinapinic acid for IMS is its low solubility in many solvents including in 1:1 acetonitrile:H_2O. As a result, it is not possible to deposit sufficiently thick sinapinic acid crystals on gold surface by the selective dewetting process. To overcome this limitation, I describe a different deposition method in this chapter that was developed for sinapinic acid. This process is able to deposit sinapinic acid crystals with various thicknesses, and it is likely to be useful as well for other matrix compounds that exhibit low solubilities.
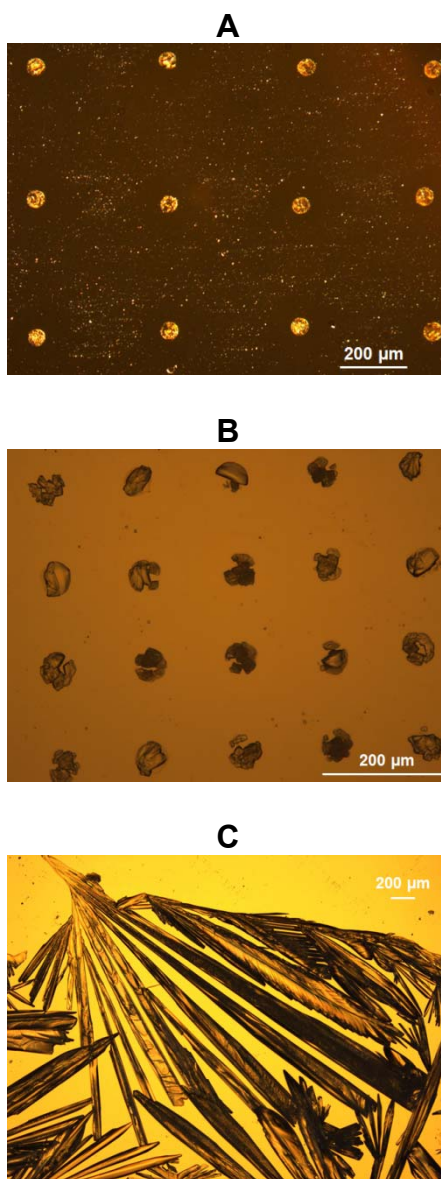
Figure 8.2. Optical photographs of DHB crystals on gold surfaces. (A) Patterned DHB crystal array formed by selective dewetting. The spot size is ~ 50 μm, and the center-to-center distance between spots is 400 μm. The DHB matrix solution was 20 mg/mL in 50:50 acetonitrile/0.2% TFA in deionized H_2O. (B) Patterned DHB crystal array formed by selective dewetting. The spot size is ~ 50 μm, and the center-to- center distance between spots is 150 μm. The DHB matrix solution was ~260 mg/mL in 50:50 acetonitrile/0.2% TFA in deionized H_2O. (C) DHB crystals on a non-patterned gold surface formed after removal from a 262 mg/mL DHB solution and allowed to evaporate.

liquid drop
with height h
and contact
angle θ

h

θ

a

u

$u = a \cdot \tan(90 - \theta)$
$r = a/\cos(90 - \theta)$
$h = r - u$
$V_{cap} = (1/6)\pi h(3a^2 + h^2)$

Figure 8.3. Schematic illustration of a spherical cap with height *h* and radius *a*, representing the side view of a droplet on a circular spotted region of diameter *2a* and having a contact angle *θ*.

Matrix crystal arrays formed by selective deposition. In a selective deposition

process, the matrix solution (~1-400 μL) was pipetted onto the support surface, i.e., the

patterned gold surface (Figure 8.4(A)) to fully cover the surface region of interest. The

matrix solution consisted of a solvent such as ethanol, acetic acid, chloroform and water

and the matrix compound (sinapinic acid) at concentrations near its saturation level. As

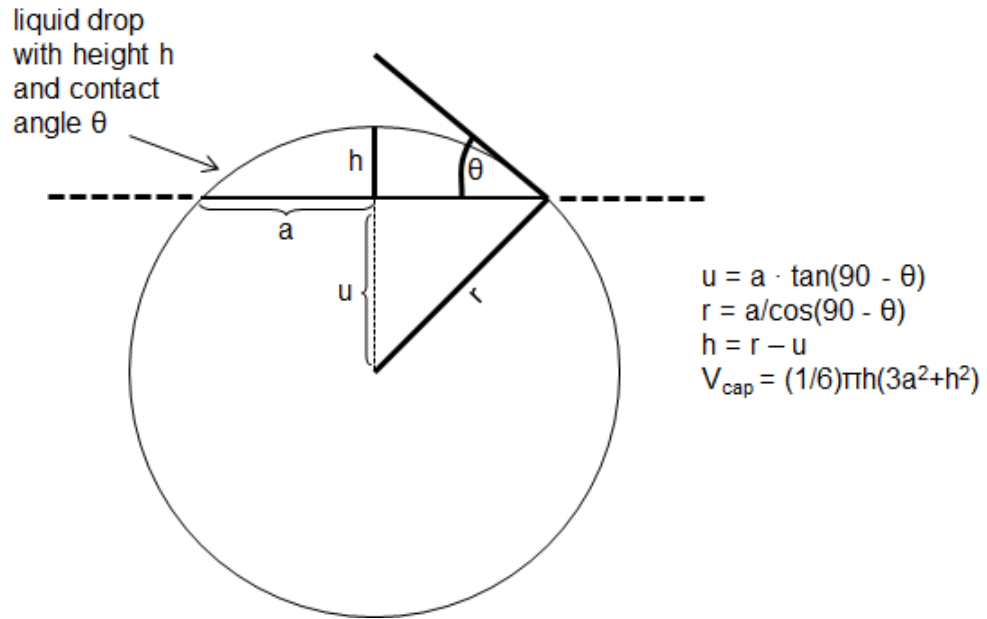the solvent film underwent evaporation, crystals started to form in the liquid film present

on the support surface. For sinapinic acid, the formed crystal size were ~ 10 μm or less

in size as observed under an optical microscope during the crystallization process.

During their formation, the matrix crystals moved around the surface, and predominately

located within the hydrophilic regions on the surface. This process required only a few

minutes to occur (Figure 8.4(B) and (C)). During the evaporation process when the

matrix crystal array was forming, the liquid drop continued to fully cover the substrate

surface (Figure 8.4 (B) and (C)), and it was subsequently removed by pipette or a

Kimwipes tissue after sufficient deposition had occurred (Figure 8.4 (D)). The formed

array was then dried in the atmosphere and showed a high degree of selective deposition

(Figure 8.4 (E)).

Depending on the features present on the PDMS stamp that is used to pattern the

gold surface, the matrix crystals can be patterned in a denser array with the spots located

closer to one other. Figure 8.5 shows an array formed where the center-to- center

distance between spots is 150 μm. This density is higher than can be achieved by current

acoustic spotting methods, which has a limiting center-to- center distance between spots

of ~200-300 μm. In Figure 8.5(A), 400 μL matrix solution was pipetted onto a patterned

gold surface area of ~ 1 cm^2. Although the matrix compound still formed crystals in

discrete spots, they grew in many different orientations and the matrix compound packed with each other to form complex 3-D structures. The crystals prefer to deposit on the uncoated gold surface areas and avoid the hydrophobic surface regions. In contrast with the dewetting process, this method of deposition allows significantly greater amount of matrix to be deposited on each spot. This deposition process is both straightforward and rapid as all the spots undergo deposition in a parallel fashion. The process allows control over the amount of matrix that is deposited by simply controlling the pipetted volume of matrix solution onto the patterned gold surface.

To determine the amount of SA crystals that was deposited on each spot in a typical process, a slide was weighed before and after the deposition of the crystal array. By using 100 µL matrix solution on a 3000-spot array, each 120 µm spot formed a deposit with ~170 × 10^{-6} mg SA. The average thickness of these spots was calculated to be ~ 11 µm. A comparison of the matrix amounts that have been produced by various methods is summarized in Table 8.1.

Matrix crystal arrays formed by selective dewetting plus deposition. Selective deposition process also could be performed on a gold surface following a dewetting process. I refer this combination process as selective dewetting plus deposition. In this process, a gold surface was first patterned with a SA crystal array by selective dewetting, and then matrix solution was either pipetted onto the surface or the slide was immersed into a matrix solution in a vial that was open to the atmosphere to allow solvent evaporation from the solution. As shown in Figure 8.5(B), the crystals have a shorter aspect ratio in comparison to those shown in Figure 8.5(A), and on each spot the crystals are closely packed to form a flatter spot surface.

195
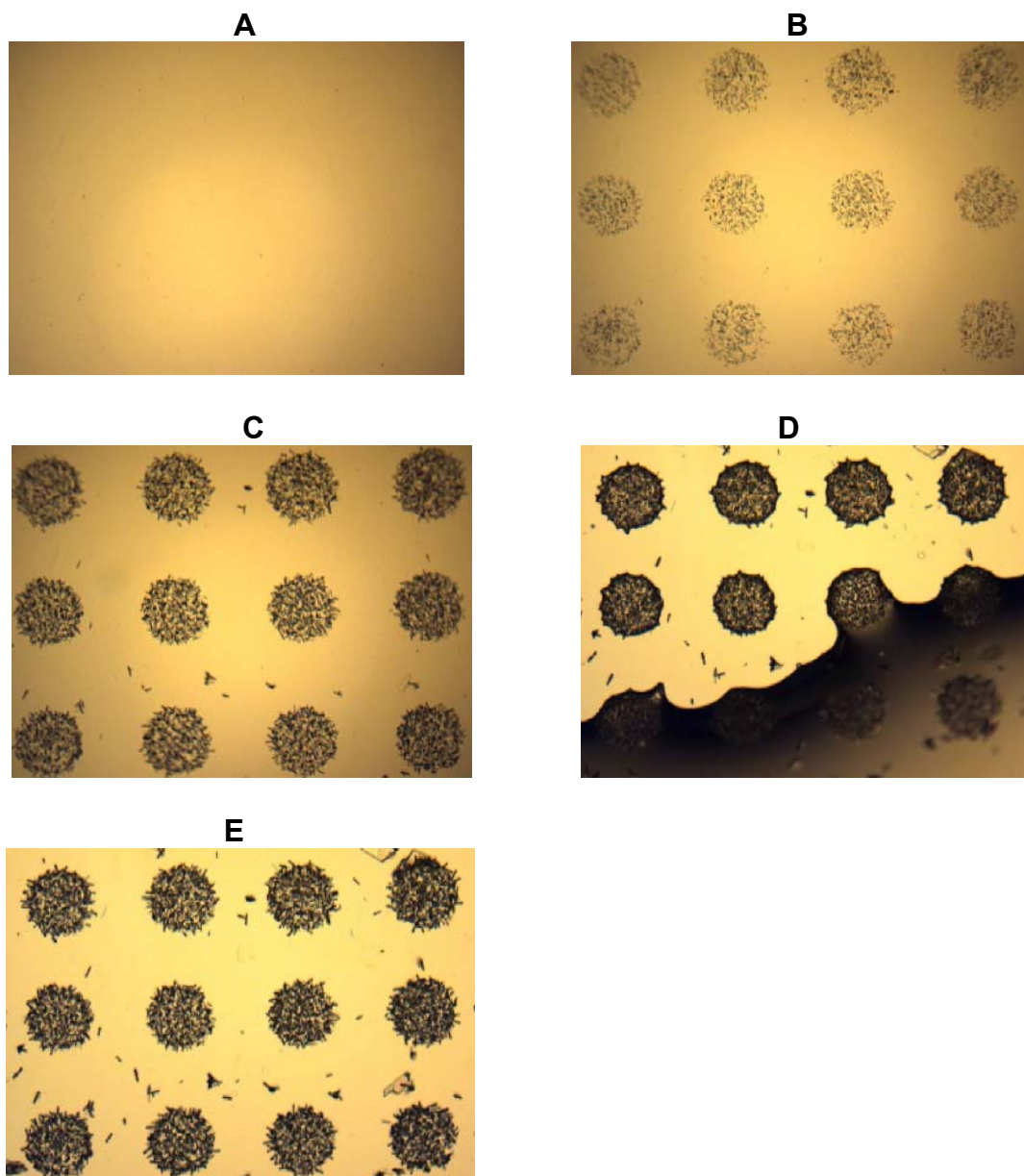
Figure 8.4. Optical photographs showing the formation progress of a SA crystal array. (A) Matrix solution containing saturated SA pipetted on a gold surface. The matrix solution was the upper layer solution from the mixture solution of 10 mg/mL sinapinic acid in 1:1 Carnoy's fluid:water. (B) One minute later, a SA crystal array can be observed to form. The surface remained covered by the matrix solution. (C) Two minutes later, thicker SA crystals formed on each spot. A few crystals also deposited on the hydrophobic region. The surface remained covered by the matrix solution. (D) The matrix solution was being removed from the surface. The removing step took a couple of seconds. (E) The SA crystal array after drying in the atmosphere. The spot size is 170 µm, and the spot center to spot center distance is 300 µm.

Figure 8.5. Optical photographs of (A) a patterned sinapinic acid crystal array made by selective deposition on a gold surface, and (B) a patterned sinapinic acid crystal array by selective dewetting followed by selective deposition.
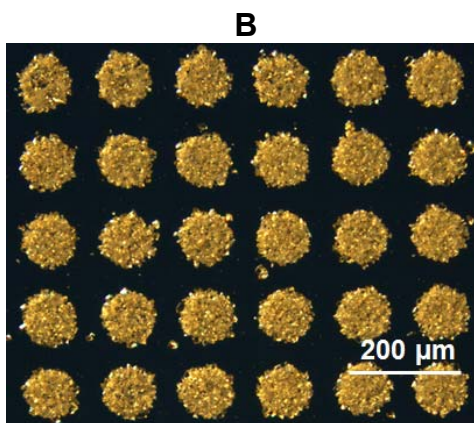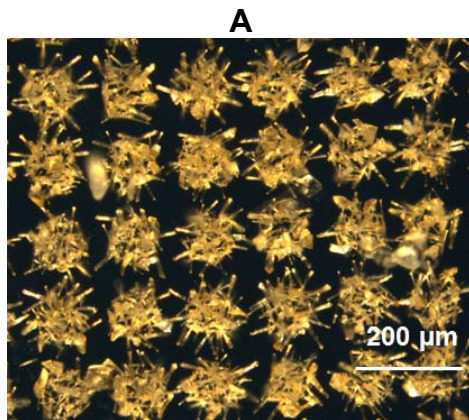
Table 8.1 Matrix amount for each spot prepared by different methods

Method	Matrix Amount ($\times 10^6$ mg)	Spot diameter[a], µm	Spot thickness[b], µm	Conditions
Acoustic spotting	100	250	1.6	30 drops, each 0.17 nL, 20 mg/ml matrix
Selective dewetting	2.9	160 (50)	1.1	20 mg/ml matrix
Selective dewetting	15.8	120 (50)	6.1	262 mg/ml matrix
Selective deposition	167	120	11	100 µL matrix pipetted on a 3000-spot array

Note: (a) for selective dewetting, spot diameter 160(50) µm means that the PDMS stamp has the well size of 160 µm (i.e., the size of the uncoated circular gold spot), and the formed DHB crystals have the size of 50 µm. The DHB crystals are smaller than the circular gold spot is probably due to solvent evaporation. (b) estimated on mass, full coverage, assumed density of 1.307 g/cm^3 (www.lookchem.com) for sinapinic acid. The density of DHB is not available, and is assumed to be same as SA at 1.307 g/cm^3.

Application of tissue sections. After the patterned matrix crystal array is prepared, the application of a tissue section onto such a pre-coated matrix surface is straightforward. Typically a tissue section could be thaw-mounted onto the pre-coated surface, the same as we prepare a tissue sample on a flat surface before the acoustic matrix spotting process. Figure 8.6 shows the optical images of the patterned matrix arrays with a 5 μm thick tissue sections that was thaw-mounted on them. On arrays that were prepared by selective dewetting (Figure 8.6(A)) and by selective dewetting plus deposition (Figure 8.6(C)), the applied tissue sections look flat and appear to cover the array surfaces well. However, on the array surface that was prepared by selective deposition, the matrix crystals yielded a rough surface (Figure 8.5(A)) and the tissue section appears to "grab" onto each individual spot causing cracks in the overlain tissue, as shown in the inset of Figure 8.6(B). In IMS, it appeared that the presence of such cracks might allow more signals to be passed from the underlying matrix.

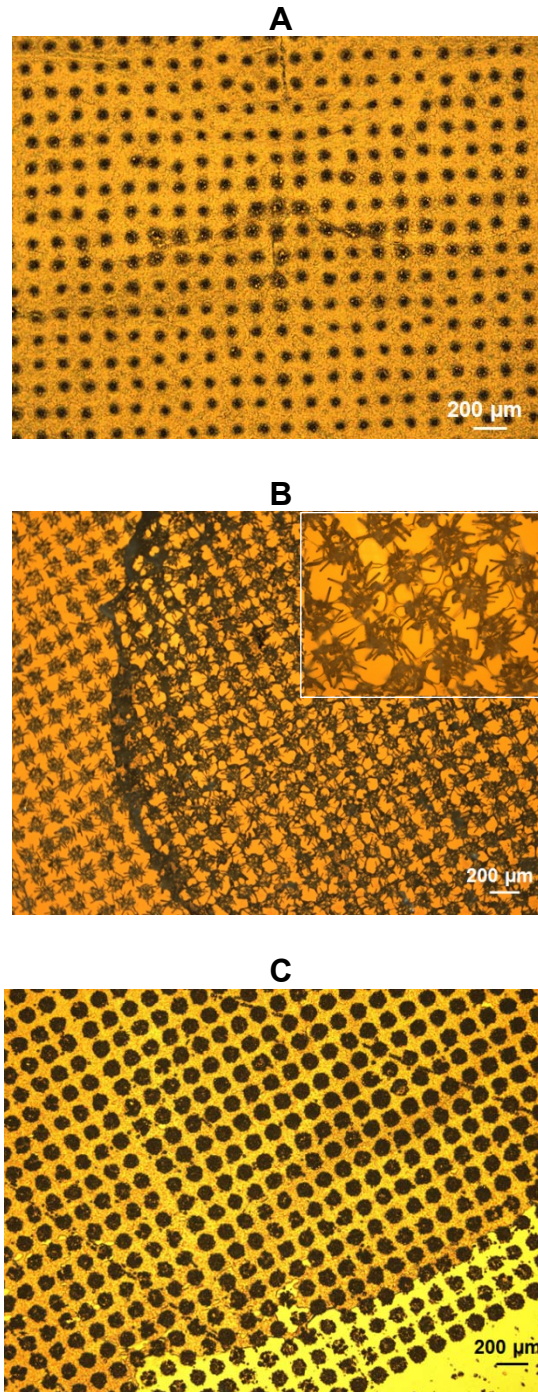**Figure 8.6.** Optical photographs of matrix crystal arrays with tissue section applied. (A) 5 μm thick mouse brain tissue covering a DHB crystal array prepared by selective dewetting. (B) 5 μm thick mouse brain tissue covering a SA crystal array prepared by selective deposition, with inset at higher magnification. (C) 5 μm thick mouse brain tissue covering a SA crystal array prepared by selective dewetting and deposition.

MALDI signals from a tissue sample. The abilities of the pre-coated matrix spots to yield MALDI signals were examined by placing a tissue section on top of a matrix array. The DHB crystal arrays were prepared using 20 mg/mL DHB matrix solution in 1:1 acetonitril:water, and the selective dewetting process. Rat brain tissue sections were applied on both fully dried DHB spots and wet frozen spots, with an example of the latter shown in Figure 8.7(A). The wet frozen spots were produced by quickly (in a couple of seconds) placing the slide into a humidity chamber after its removal from the matrix solution. The DHB liquid microdroplets remained as liquids in the chamber and were then frozen using dry ice before the application of the tissue. Superior results in MALDI were obtained using the wet frozen spots in comparison to the fully dried spots

Figure 8.7 (B) shows the obtained MALDI mass spectral signals using the wet frozen spots. The MALDI signals are contributed by the presence of lipids in the tissue sample. This experiment indicated the promise of using the pre-coating approach for imaging mass spectrometry. Also, it showed the importance of the presence of solvents for obtaining MALDI signals from species in a tissue. This factor would be especially important for proteins since they are much heavier than lipids in terms of molecular weight. The ability to obtaining protein signals is strongly desired for this work and next I describe approaches that directed toward improving the interactions between a tissue and the matrix compound with the goal to detect high quality protein signals.
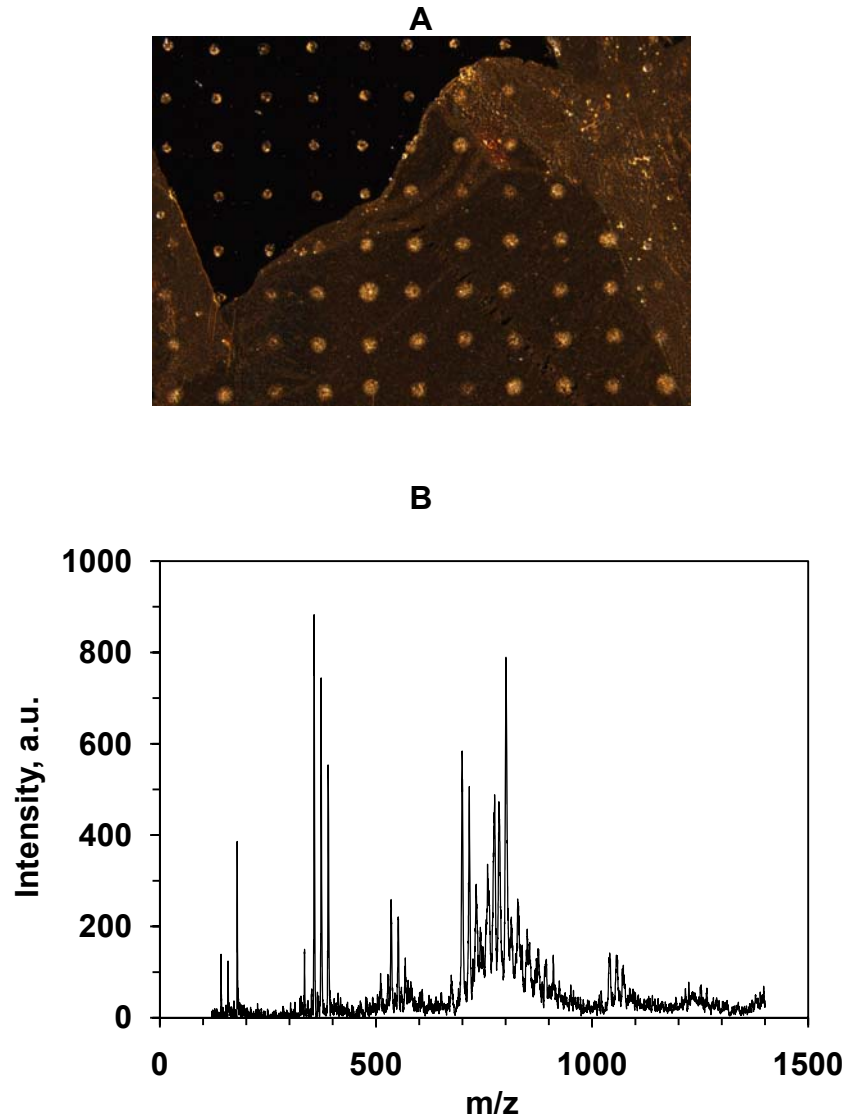
A

B

Figure 8.7. (A) Optical photograph of a rat brain tissue section covering a DHB crystal array (wet frozen). The spot sizes are 70-85 μm, and center-to-center distance between spots is 300 μm. (B) MALDI spectrum take from one spot covered with tissue collected using 100 laser shots.

Vapor treatments to enhance interactions between tissue and matrix. Although wet frozen spots were used to maintain solvents in each spot initially, it requires the slide to be loaded into a humidity chamber quickly after its removal from the matrix solution and also requires the liquid microdroplets to be frozen so that the drops are not evaporative during the tissue application step. This preparation is tedious and hard to control. In addition, the amount of solvent is also limited to the volume of the initial liquid droplet obtained from the dewetting process.

A solvent vapor stream was used to improve the easiness and flexibility of sample preparation and to enhance interactions between the matrix crystals and the overlain tissue. After the patterning and dryness of the matrix array by either aforementioned method and the application of tissue, the sample was introduced into a chamber with solvent vapor environment. The chosen solvents included water, alcohol and other chemicals. The solvent vapors selectively condensed into regions where the matrix spots were under the tissue and generated separated droplets within the tissue defined by the regions where the matrix was placed. Simultaneously, the matrix crystals dissolved into the condensed solvents, and after removal of the slide from the vapor chamber, the matrix recrystallized. The condensation, dissolving and recrystallization steps greatly assisted the contact between tissue and discrete matrix spots in a parallel format. Figure 8.8 shows the optical images of two DHB matrix spots in a methanol vapor environment. The crystals were almost fully dissolved into the condensed solvent in one minute and recrystallized after the removal from the methanol vapor. With the vapor treatment, the lipid and protein MALDI signals are readily obtained using the array spots. Figure 8.9 shows the effect of vapor treatment for obtaining MALDI

protein signals. Both methanol and water vapors enhance the number of protein peaks to be detected. It is noted that the peak positions from methanol and water are different, indicating that both methanol and water may be useful for extracting different proteins from tissue. For obtaining better mass spectral signals, methanol and water vapor mixture was often exposed to the sample at the same time to increase the extraction of both water soluble and alcohol soluble from tissue.

During the development of this work, much effort was focused on obtaining MALDI protein signals. SA is empirically considered as a more appropriate matrix for protein signals in MALDI experiments. SA crystals can be patterned by selective deposition as aforementioned thus SA crystal array can be patterned with more material on each spot than DHB array. As shown in Table 8.1 (last two rows), using the same PDMS stamp, the formed SA spot has $10 \times$ more matrix than a DHB spot. How much matrix is needed for high quality of MALDI protein signals is not known, and it should be also related with the amount of analytes (the thickness of tissue), the extraction efficiency, and the ionization efficiency, etc. We chose to use SA crystal array for the proof-of-concept experiments for imaging mass spectrometry since it allows us a wider range to control the amount of matrix on the spots. Next I describe vapor experiments on SA crystals.

Since sinapinic acid has lower solubility in alcohol and water than DHB. Exposing SA crystal to methanol and water vapor does not fully dissolve the crystals in each spot, as shown in Figure 8.10. To improve the vapor pressure, some vapor treatment experiments were also carried out with the vapor chamber loaded into an oven at 90 °C for 4 min to increase the vapor pressures of the solvents and enhance interactions

between matrix and tissue. Figure 8.11 shows MALDI mass spectral signals obtained from a SA spot covered with a rat brain tissue sample. The collection of protein peaks are due to their presence in the tissue sample.

Except to solvents like water and alcohol, any evaporative chemicals possibly can be transferred to contact with each matrix spot and react with the crystals. For example, diisopropylethylamine (DIEA) vapor was used to transform the SA matrix crystals on each spot into the ionic liquid droplets without changing the coordinates of the spots, as shown in Figure 8.12. The formed ionic matrix can recrystallize in water with 2% TFA. Figure 8.13 shows the optical images of a SA array sample at the different stages. The TFA in water is used since TFA is a stronger acid than sinapinic acid, and it will replace SA to associate with DIEA, allowing SA crystals to form. This method was used for protein imaging mass spectrometry. One concern with the water (2% TFA) step is that immersing the whole surface into water may delocalize some analytes on the tissue surface, which need further investigations.
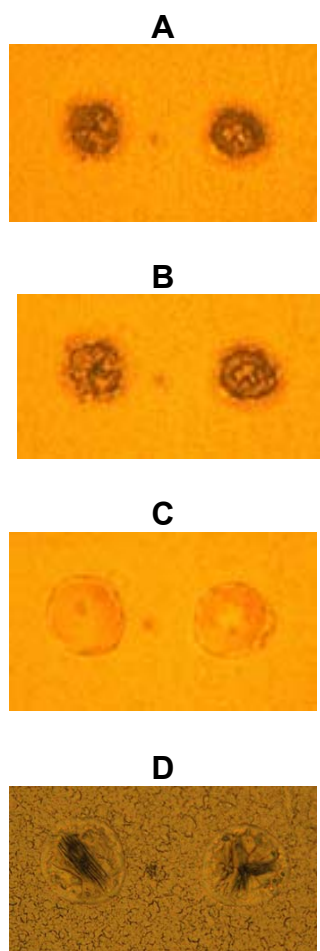
Figure 8.8. Optical photographs showing the progress of using methanol vapor to dissolve DHB matrix. Spot sizes is 130-160 μm, and spot center to spot center distance is 300 μm. (A) 6 μm thick rat brain tissue section covering the DHB spots. (B) The spots were present to methanol vapor for 30 s. (C) The spots were present to methanol vapor for 1 min. The matrix crystals were almost fully dissolved in the solvent. Spot sizes increased from the initial 130 μm to 160 μm. (D) The matrix spots recrystallized.

A
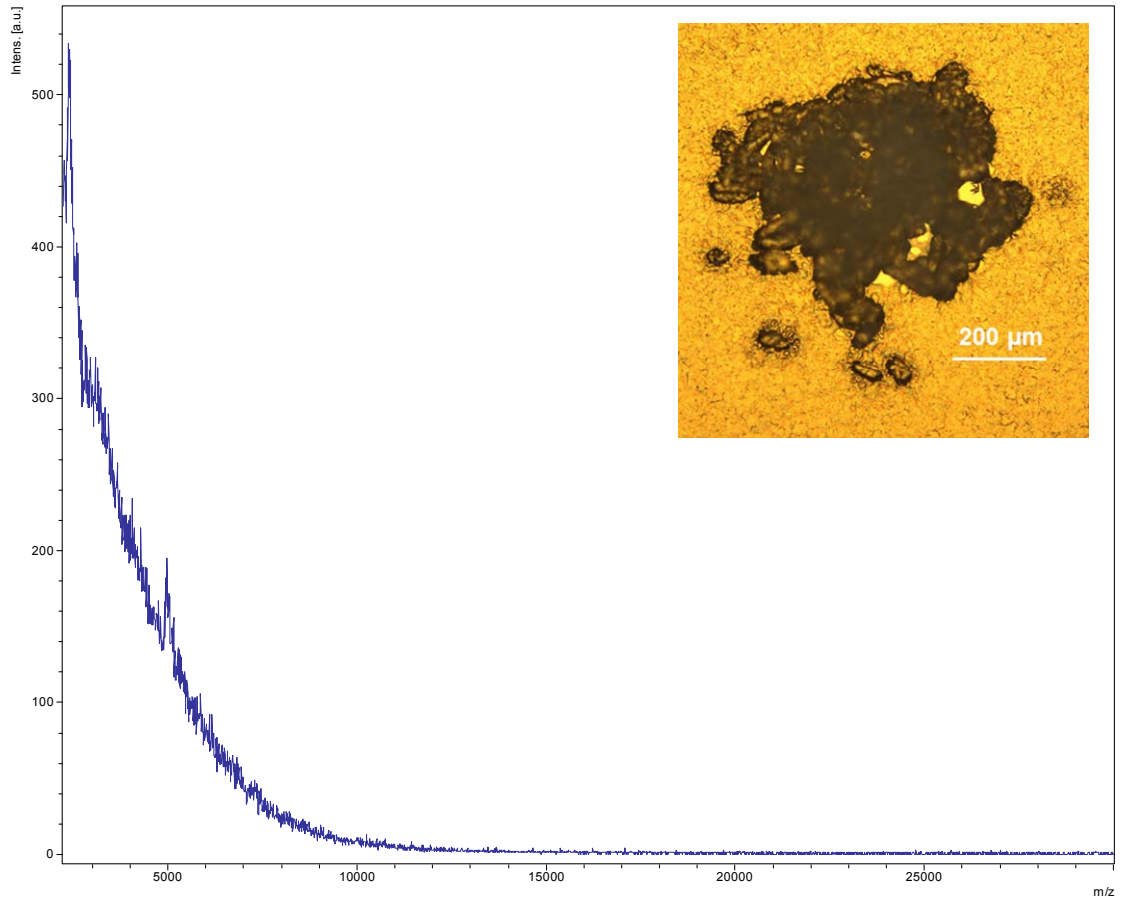
B
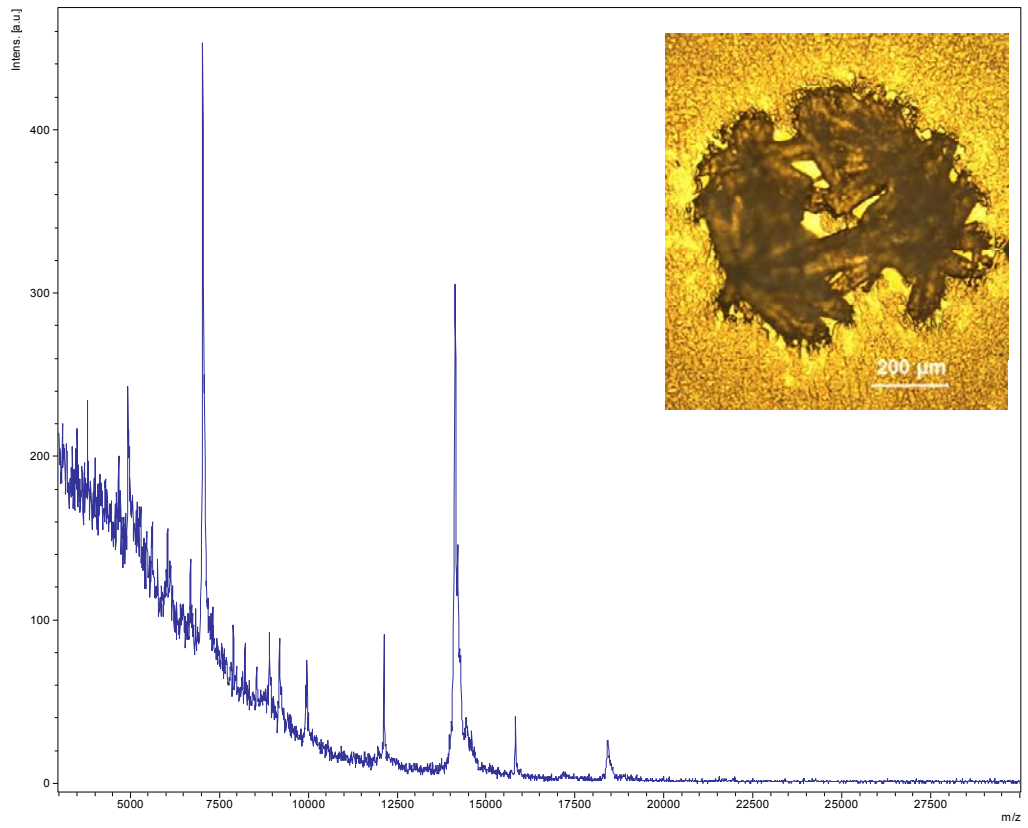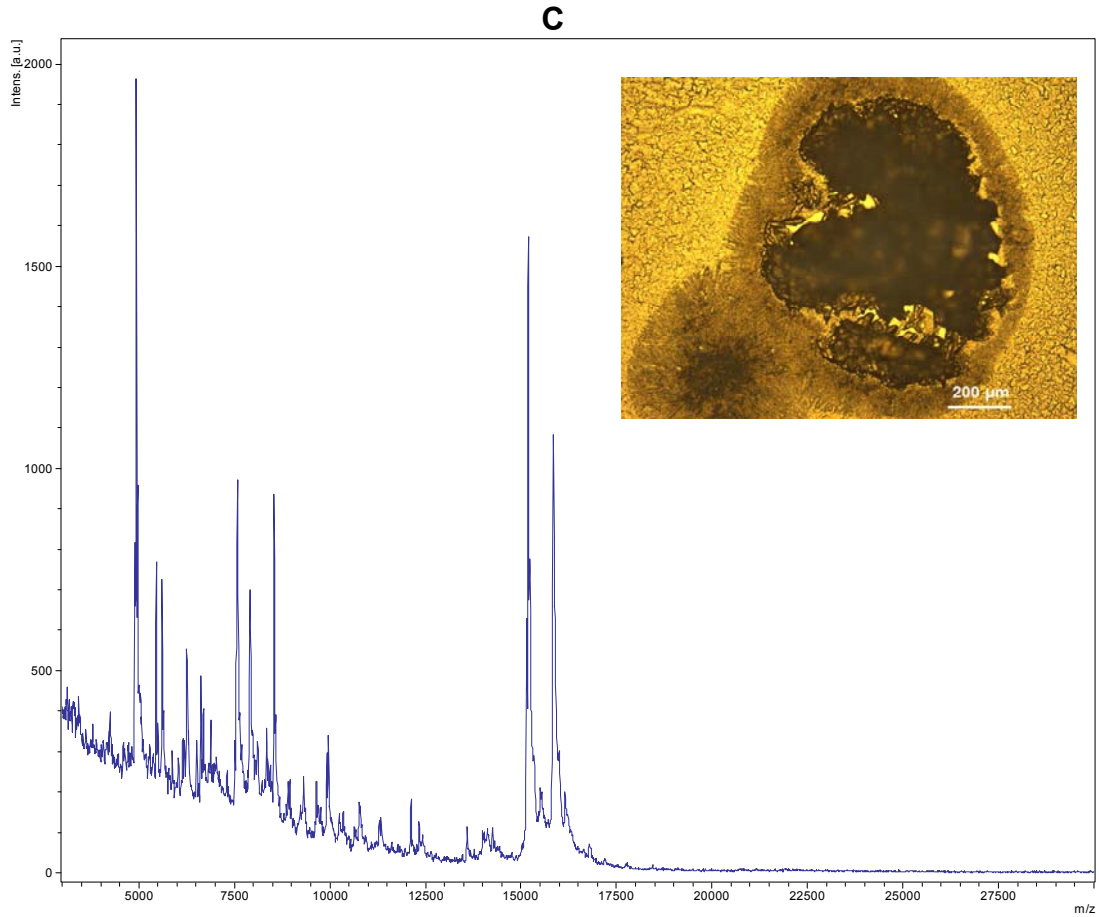
Figure 8.9. MALDI spectra from a DHB matrix spot. The insets are optical photographs of the surface. DHB spot size: 600 μm. tissue thickness: 6 μm. (A) No vapor treatment. (B) Water vapor treatment at room temperature. (C) Methanol vapor treatment.
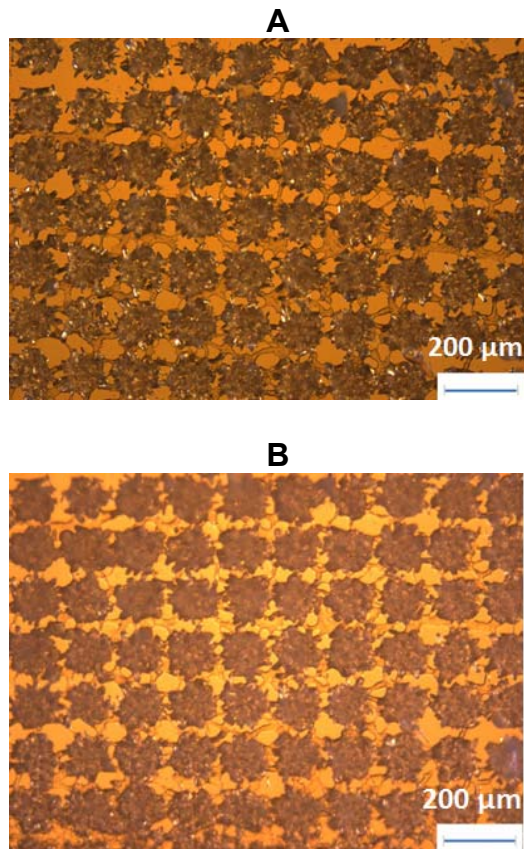
Figure 8.10. Optical photographs of a SA array. (A) A SA crystal array made by selective deposition, covered with a 5 µm thick mouse brain tissue section. (B) The array surface was rehydrated with method and water vapor for 35 min. The image was taken with the sample inside the vapor chamber.
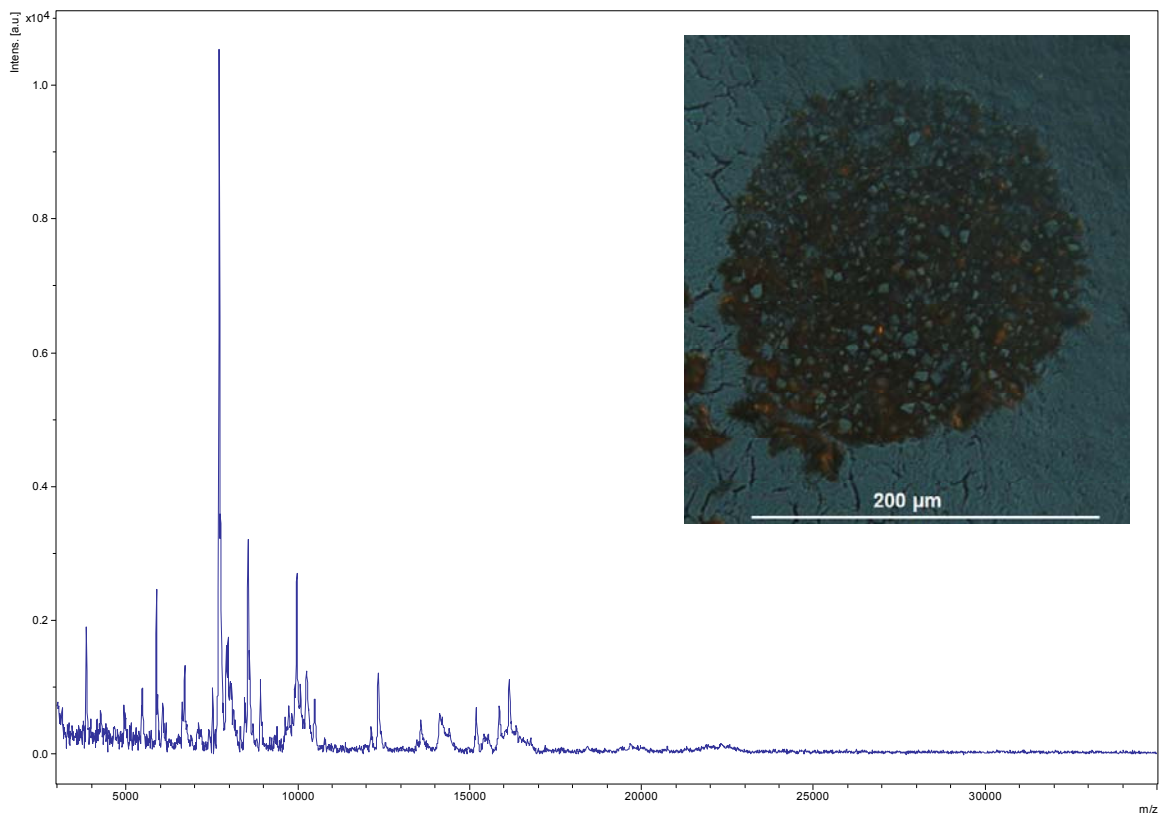
Figure 8.11. A MALDI mass spectrum take from a 200 μm SA spot (the inset shows the spot image) covered with a 6 μm thick rat brain tissue section. The spot was treated with methanol and water vapor at 90 °C for 4 min.
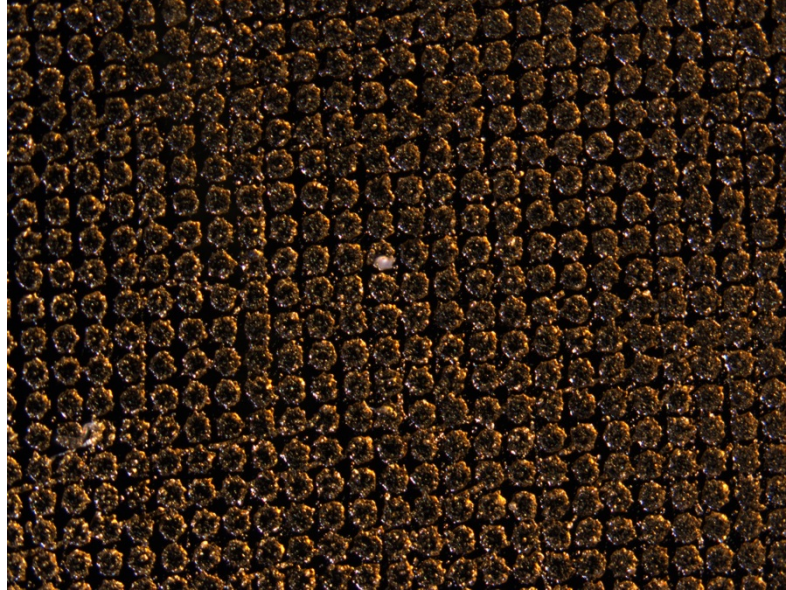
Figure 8.12. Optical photograph of a SA-DIEA array. The spot size is 120 μm, and spot center to spot center distance is 150 μm. The SA array was prepared by selective deposition (15 mg/mL SA in 1:1 Carnoy's fluid:water), and the slide was then loaded into a DIEA vapor chamber (100 μL DIEA pipetted in the chamber). No tissue applied on this surface.
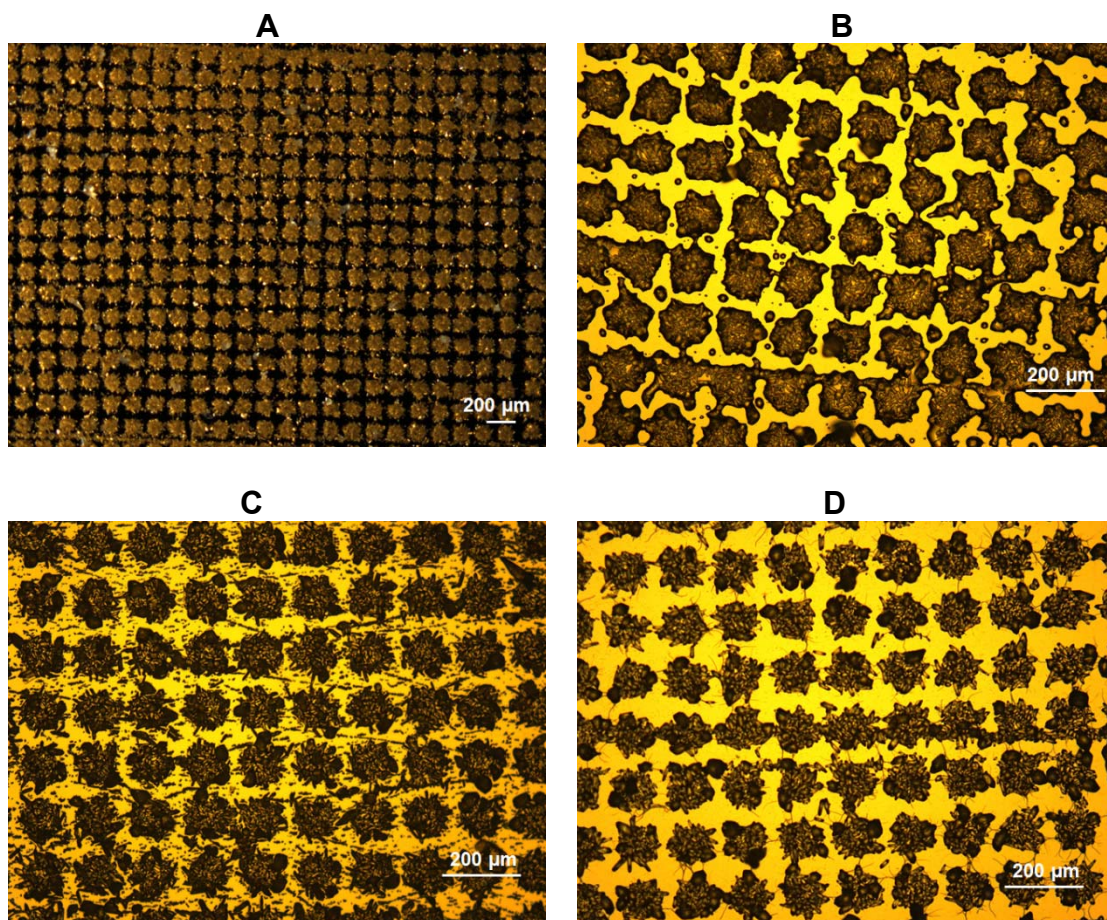
Figure 8.13. Optical photographs of SA crystal array. (A) SA array formed by selective deposition. (B) SA array under DIEA vapor (200 µL DIEA liquid, 20 min). (C) SA-DIEA ionic matrix recrystallizes by covering the array with 200 µL deionized water (2% TFA) for 4 min. (D) SA array after the removal of the 200 µL deionized water (2% TFA) and dried.

Lipid imaging mass spectrometry. MALDI imaging mass spectrometry experiments was performed using the pre-coated matrix crystal array to obtain the ion maps across the surface of a 5 μm thick mouse brain tissue section. Figure 8.14 (A) shows the distribution of ions at two selected m/z values. Shown in Figure 8.14 (B) are two spectra at two different regions indicated on the ion map of m/z 827. The resolution of the matrix spots is 150 μm center-to-center distance, comparing to 200~300 μm by using an acoustic spotter. By using a PDMS stamp with smaller features, it is feasible to improve the pre-coated matrix spot resolution to 10 μm. This proof-of-concept experiment indicates the possibility of using the pre-coated matrix crystal array for high resolution imaging mass spectrometry. The pre-coating method combines the advantage of high density matrix application for imaging MS and ease of sample preparation while maintaining the ability to analyze a wide variety of analytes, such as lipids, peptides, and proteins from a tissue sample. This method can potentially realize high throughput and high resolution MALDI imaging.

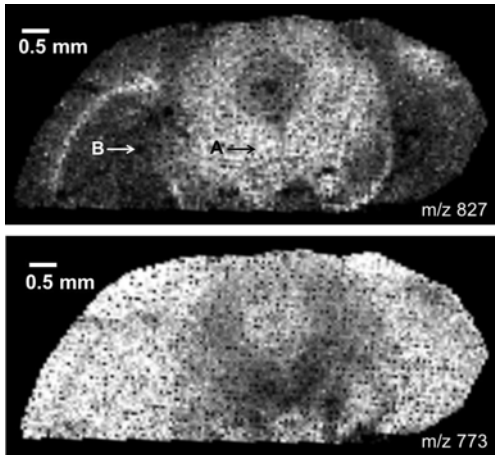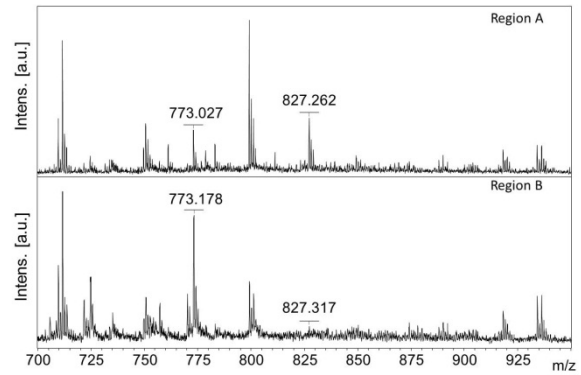**Figure 8.14.** (A) MALDI ion density maps at selected m/z values of 827 and 773. The surface was prepared by thaw-mounting a 5 µm thick mouse brain tissue section on a patterned sinapinic acid matrix crystal array, followed with a vapor rehydration step. (B) The representative spectra from two different locations on the tissue surface, noted as Region A and Region B on the upper left ionic map (m/z 827).

8.4 Conclusions

Pre-coating a MALDI target is an alternative sample preparation approach for fast and simple imaging mass spectrometry. A MALDI target can be patterned by microcontact printing to have relatively hydrophilic surface areas surrounded by a continuous hydrophobic surface. Matrix crystals can be regioselectively deposited onto the hydrophilic spots, forming a matrix crystal microarray. Matrix crystal arrays can be patterned on surfaces by either selective dewetting or by selective deposition. Both methods can yield thousands of matrix spots with sizes ranging from 50 to 200 μm in a few minutes. Solvent or other chemical vapors were used to enhance the extraction between matrix and tissue. Ion signals ranging from a few hundred to 30000 m/z were obtained from tissue samples applied on top of the arrays. Imaging mass spectrometry experiments were performed with a resolution at 150 μm spot center-to-center distance. This approach speeds up the sample preparation by decreasing the preparation time from a few hours to ~30 minutes, avoids expensive spotters, and provides possibilities of high resolution and high throughput imaging by using an array format.

References

1   Caprioli, R. M.; Farmer, T. B.; Gile, J., "Molecular imaging of biological samples: localization of peptides and proteins using MALDI-TOF MS", *Anal. Chem.* **1997**, *69*, 4751-4760.

2   Puolitaival, S. M.; Burnum, K. E.; Cornett, D. S.; Caprioli, R. M., "Solvent-free matrix dry-coating for MALDI imaging of phospholipids", *J Am Soc Mass Spectrom* **2008**, *19*, 882-886.

3   Groseclose, M. R.; Andersson, M.; Hardesty, W. M.; Caprioli, R. M., "Identification of proteins directly from tissue: in situ tryptic digestions coupled with imaging mass spectrometry", *J. Mass Spectrom.* **2007**, *42*, 254-262.

4   Seeley, E. H.; Caprioli, R. M., "Molecular imaging of proteins in tissues by mass spectrometry", *PNAS* **2008**, *105*, 18126-18131.

5   Caprioli, R. M., "Perspectives on Imaging Mass Spectrometry in Biology and Medicine", *Proteomics* **2008**, *8*, 3679–3680.

6   Schwartz, S. A.; Reyzer, M. L.; Caprioli, R. M., "Direct tissue analysis using matrix-assisted laser desorption/ionization mass spectrometry: practical aspects of sample preparation", *J. Mass Spectrom.* **2003**, *38*, 699-708.

7   Aerni, H.-R.; Cornett, D. S.; Caprioli, R. M., "Automated acoustic matrix deposition for MALDI sample preparation", *Anal. Chem.* **2006**, *78*, 827-834.

8   Hankin, J. A.; Barkley, R. M.; Murphy, R. C., "Sublimation as a Method of Matrix Application for Mass Spectrometric Imaging", *J Am Soc Mass Spectrom* **2007**, *18*, 1646-1652.

9   Porter, M. D.; Bright, T. B.; Allara, D. L.; Chidsey, C. E. D., "Spontaneously Organized Molecular Assemblies. 4. Structural Characterization of n-Alkyl Thiol Monolayers on Gold by Optical Ellipsometry, Infrared Spectroscopy, and Electrochemistry", *J. Am. Chem. Soc.* **1987**, *109*, 3559-3568.

10   Bain, C. D.; Troughton, E. B.; Tao, Y.-T.; Evall, J.; Whitesides, G. M.; Nuzzo, R. G., "Formation of Monolayer Films by the Spontaneous Assembly of Organic Thiols from Solution onto Gold", *J. Am. Chem. Soc.* **1989**, *111*, 321-335.

11   Harris, J. W.; Stocker, H. *Handbook of Mathematics and Computational Science*; Springer-Verlag: New York, 1998, p107.

CHAPTER IX

SUMMARY

9.1 DNA microarrays

Oligonucleotide microarrays have become an increasingly important tool for genomic investigations such as gene expression studies, single nucleotide polymorphisms (SNPs) and DNA sequencing. However, conventional DNA microarray methods do not provide probe sequences with both covalent end-immobilization and high fidelity, and lack of quantitative data for studying DNA molecular interactions in real time.

My first goal of this work was to develop a surface architecture that provides covalent end-immobilization of DNA probes with user-defined sequences to a substrate surface, commonly a glass slide surface. A thin film of surface oligonucleotides was synthesized on a slide surface and DNA probes were patterned on the surface by a robotic microarray spotter. The surface oligonucleotides and DNA probes were end-immobilized through the base pairs between them (Chapter II), and further covalently cross-linked by psoralen molecules (Chapter V). This methodology allows researchers to customize the DNA probes that comprise a DNA microarray, and obtain covalent end-immobilization between probes and substrates. These surfaces could have high fidelity of probe

sequences. They could be used in real-time melting experiments to investigate interactions between DNA molecules, such as DNA thermal desorption.

The second goal of this work was to investigate the kinetics of DNA hybridization and dehybridization at surfaces. Such *in situ* measurements were aimed towards obtaining more quantitative data to better understand the dynamic behaviors between DNA molecules. Accompanied with this goal was the progressive development of an integral optical system, total internal reflection fluorescence (TIRF). The TIRF system was coupled with a flow system which has a linear temperature sweeping ability. DNA hybridization kinetics between targets and surface oligonucleotides were observed using the TIRF system, and mathematical models were applied to analyze the experimental data and obtain estimates on the reaction rates, equilibrium constants, and surface probe densities (Chapter III). DNA non-equilibrium desorption studies were performed on both a homogeneous surface (Chapter IV) and a patterned surface (Chapter V). Chapter IV shows that a single base mismatch was discerned from the thermal desorption curves of both perfectly matched and one base mismatched sequences. Redhead's thermal desorption theory was applied to fit the experimental data and obtain the estimates on the activation energies of DNA duplexes. The measured half and peak temperatures were compared with predicted melting temperatures using nearest-neighbor model. Chapter V shows the reliability of the measurements on the half and peak temperatures from DNA thermal desorption curves using a 6×6 mm patterned surface. Although the intensity profile of the incident light affects the relative fluorescent intensities of DNA spots on the TIRF images, it did not show a significant effect on the measurements on half and peak temperatures. The peak temperatures were more

independent on the surface coverage and probably a more reliable characteristic parameter to use comparing to the half temperatures.

The devised system could be used to obtain a collection of DNA desorption curves in one single thermal desorption experiment for spots ranging from a few to hundreds of on a surface. The determined peak temepratures and activation energies are characteristic to the sequences of the spots. Such information could be useful towards detection of SNPs and DNA sequences.

9.2 Imaging mass spectrometry

MALDI (matrix-assisted laser desorption/ionization) imaging mass spectrometry (IMS) has emerged as a powerful technology to examine the relative abundance and spatial distribution of biomoleucles across a tissue section. Current sample preparation method for IMS is tedious and time-consuming, and has a low resolution.

This work developed pre-coated matrix crystal surfaces for imaging mass spectrometry. Chapter VIII describes the details of this sample preparation method. Matrix crystal arrays could be formed on a patterned gold surface in a few minutes without using an expensive instrument. Three matrix deposition methods were developed, selective dewetting, selective depositon, and selective dewetting plus selective deposition. The selective dewetting method could potentially be used for any matrix that has certain solubility in a polar solution. The selective deposition was developed for sinapinic acid,

222

a very commonly used matrix in IMS, and possibly it also applies to other matrices of interest. MALDI mass spectrometry signals on tissue samples were obtained and imaging mass spectrometry was performed. The developed method is promising as a fast and simple sample preparation approach for high resolution and high throughput imaging mass spectrometry, and is in the application for a patent (Paul E. Laibinis, Richard M. Caprioli, Zhou Xu, Junhai Yang, "Pre-coated surfaces for analysis", filed on May 21, 2010).

Associated with the development of the pre-coated matrix crystal arrays for IMS, I provided a liquid-polymer casting approach to pattern a PDMS (polydimethylsiloxane) surface with dimples. The PDMS surface could be used as a stamp for microcontact printing. It is often difficult to prepare such a structure using common photolithography. Chapter VII shows the details on the preparation steps and its uses. The size of the dimples and their center-to-center distance are dependent on the size and center-to-center distance of the liquid microdroplets that are placed on a substrate surface during the printing process. The current dimple size is 100 μm and spot center to spot center distance is 150 μm. The curvature of the dimples depends on the substrate surface and printing conditions such as humidity. If smaller liquid drops could be placed on the substrate, this method could be used to prepared smaller dimples with a higher density.

Photolithography was also used to prepare smaller SU-8 features on a silicon substrate (the SU-8 masters were prepared by Vanderbilt Institute for Integrative Biosystems Research and Education) and then the masters were used to form a PDMS stamp. As shown in Figure 9.1 (A), a thin film of sinapinic acid crystal array was formed

on a gold surface by selective dewetting, and the resolution for this array is 100 μm spot

center to spot center distance. The thickness and amount of the crystals on each spot site

were significantly increased by performing a selective deposition process (Figure 9.1 (B)).

A smaller spot size, ~ 30 μm was able to be achieved using this process (Figure 9.1(C)).

It is highly possible to reduce the spot size to 10 μm, and spot resolution at 20 μm center-

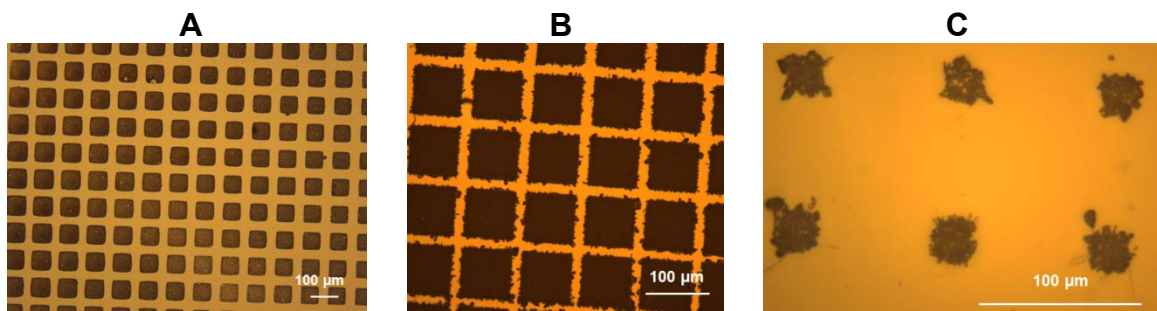to-center distance, which will be a great improvement from the current 200-300 μm

resolution.

Figure 9.1. (A) A thin sinapinic acid crystal array on a gold surface prepared by selective dewetting. Spot size: 70 ± 5 μm, spot center to spot center distance is 100 μm. (B) A thick sinapinic acid crystal array on a gold surface prepared by selective dewetting plus selective deposition. Spot size: 80 μm, spot center to spot center distance is 100 μm. (C) A thick sinapinic acid crystal array on a gold surface prepared by selective dewetting plus selective deposition. Spot size: 30 μm, spot center to spot center distance is 100 μm.

9.3 Engineered microarrayed surface

Engineered microarrayed surface provides the parallelism during either the sample analysis or preparation step. For examples, DNA microarrays have a wide variety of gene-specific probes immobilized on a surface, and they interact with a sample at the same time during the analysis step; matrix crystal arrays provides uniformly patterned matrix spots on a surface, and the spots extract analytes in a thin tissue section in parallel during the sample preparation step. Such systems could be utilized to obtain a large amount of high quality data for analysis in a short time. Using miniaturized arrays for sample analysis or preparation becomes a high throughput process and is finding use in various applications such as genomics, drug discovery, clinical diagnostics, forensics, and agriculture.